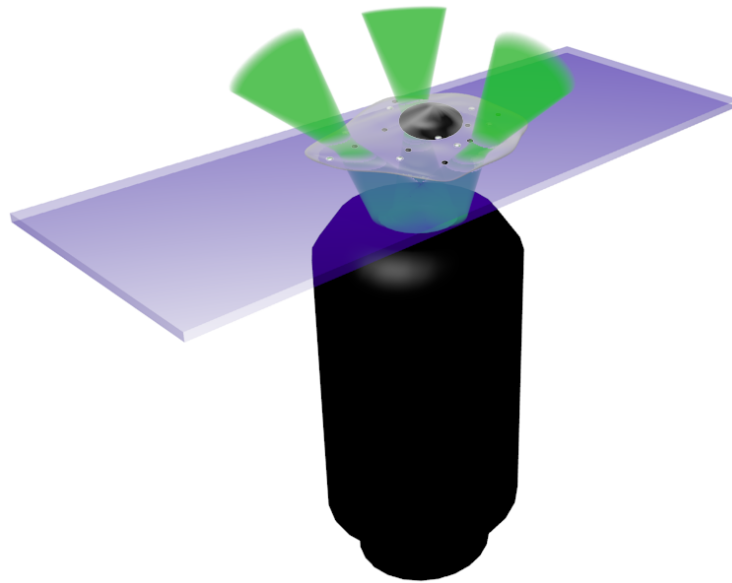


SPATIALLY RESOLVED
FLUORESCENCE CORRELATION SPECTROSCOPY

Development and Applications in cell biology



Technische Universität Dortmund
Fakultät für Chemie

Dissertation

Zur Erlangung des akademischen Grades eines
Doktors der Naturwissenschaften
(Dr. rer. Nat.)

vorgelegt von

Dipl.-Phys. Thimo-Christian Göllnitz

The work described in this thesis was performed under the supervision of Prof. Dr. Philippe Bastiaens from August 2009 to September 2012 at the Max-Planck Institute for Molecular Physiology, Dortmund.

First Examiner:

Prof. Dr. Philippe Bastiaens	Department of Systemic Cell Biology Max Planck Institute for Molecular Physiology Department of Chemical Biology Technical University, Dortmund
------------------------------	----------------------------------------------------------------------------------------------------------------------------------------------------------

Second Examiner:

Prof. Dr. Hernán E. Grecco	Department of Systemic Cell Biology Max Planck Institute for Molecular Physiology Departamento de Física Universidad de Buenos Aires
----------------------------	-----------------------------------------------------------------------------------------------------------------------------------------------

ONE SLM TO RULE THEM ALL,
ONE SLM TO FIND THEM,
ONE SLM TO ALIGN TO THEM ALL,
AND IN THE DARKNESS ENLIGHTEN THEM,
IN THE LAB F0.47 WHERE THE SHADOWS LIE.

Freely altered verse from Lord of the Rings, J.R.R. Tolkien.

Zusammenfassung

In der Zellbiologie werden Zellen als Bausteine lebender Organismen erforscht. Um ihre Funktionsweise zu verstehen, muss ein komplexes Netzwerk an Proteinen observiert werden, welches die Zelle reguliert. Eine stark verbreitete und fortwährend weiter entwickelte Methode, einzelne Typen an Proteinen im Inneren lebender Zellen zu verfolgen, stellt die Fluoreszenzmikroskopie dar. Hierzu werden Proteine mit fluoreszierenden Molekülen (Fluorophoren) markiert, die kurz nach der Anregung mit Licht einer spezifischen Wellenlänge ein Photon mit einer geringeren Energie emittieren. Die Größe einzelner Fluorophore und ihre Wechselwirkungsreichweite liegen unter dem Auflösungsvermögen klassischer Mikroskopie. Verschiedene Mikroskopietechniken wurden in der Vergangenheit entwickelt, um Fluorophore zu lokalisieren und ihre Bewegungen und Wechselwirkungen zu verfolgen. Eine Methode zur Quantifizierung der Anzahl an Fluorophoren und ihrer Bewegungsgeschwindigkeit in einem definierten kleinen Teilvolumen der Zelle ist die Fluoreszenzkorrelationspektroskopie (FCS). Hierbei werden die Fluorophore in dem Volumen angeregt und die emittierten Photonen zeitaufgelöst detektiert. Fluorophore, die das Volumen durchqueren, verursachen dabei Fluktuationen in der gemessenen Intensität. Durch Autokorrelation des Emissionshistogramms mit einer um die Zeit τ verschobenen Version wird eine Autokorrelationskurve berechnet und anschließend mit einem Diffusionsmodell gefittet. Verschiedene Volumengeometrien sind bekannt, wobei die Verwendung konfokaler Mikroskopie wegen dem geringen observierten Volumen üblich ist. In der konfokalen Mikroskopie wird ein kollimierter Laserstrahl beugungsbegrenzt fokussiert und die Detektion durch eine Lochblende auf das selbige Volumen begrenzt. Für eine räumliche Auflösung ohne Zeitverlust durch das Rastern des Volumens über die Zelle muss eine echte Parallelisierung statt finden. In dieser Arbeit wird dies durch die Parallelisierung konfokaler Mikroskopie ermöglicht. Während ein fixiertes Array an Glasfasern als Lochblenden fungiert, wird der Laserstrahl durch einen *Spatial Light Modulator* (SLM) auf die verschiedenen konfokalen Volumen aufgeteilt. Ein SLM kann optische Elemente, wie Linsen und Prismen, emulieren. In dem vorgestellten System wird dieses Gerät benutzt, um die Positionen der Glasfasern über das Scannen mit einer linienförmigen Beleuchtung zu lokalisieren und das Licht danach entsprechend auszurichten. Weiterhin wurde eine Optimierung durch das Scannen mit zusätzlich emulierten Linsen sowie die Kalibrierung der Positionierung relativ zu einem Flächendetektor mithilfe einer scannenden Punktbeleuchtung implementiert. Das Mikroskop kann an bis zu 16 parallelen Volumen (Anzahl der Glasfasern) FCS Messungen vornehmen. Es wurde erfolgreich in einer Reihe von Versuchen zur Dimerisierung von Erk2 im MAP-Kinase-Weg nach EGF Stimulieren und Kontrollmessungen in lebenden HeLa Zellen eingesetzt.

Contents

1. Introduction.....	1
1.1. Fluorescence microscopy.....	2
1.2. Fluorescence Correlation Spectroscopy (FCS).....	6
1.3. Spatial Resolved Fluorescence Correlation Spectroscopy (SRFCS).....	8
1.4. Spatial Light Modulator (SLM).....	11
2. Fluorescence Correlation Spectroscopy (FCS).....	15
2.1. Autocorrelation and diffusion model.....	16
2.2. Modifications of the diffusion model.....	22
2.3. Alternative analysis methods for fluctuation data.....	24
2.4. Requirements for FCS measurements in cells.....	25
3. Optical System.....	27
3.1. Design of the fixed optical system.....	28
3.1.1. Illumination.....	29
3.1.2. Microscope.....	30
3.1.3. Detection.....	31
3.2. Design of the adaptive optical system.....	32
3.3. SLM Devices.....	34
3.3.1. Holoeye Heo 1080P.....	34
3.3.2. Hamamatsu X10468-01.....	36
3.4. SLM control pattern creation.....	37
3.4.1. Prism and superposition.....	38
3.4.2. Lenses.....	42
3.4.3. Donut.....	43
3.4.4. Combined patterns.....	44
3.5. Calibration of system.....	46
3.5.1. Camera based calibration.....	46
3.5.2. Point detector based calibration.....	49
3.5.3. Direct search and simulated annealing algorithm for pattern improvement.....	52
4. Applications.....	57
4.1. Calibration of the positioning.....	58
4.1.1. Camera based calibration.....	59
4.1.2. Point detector based calibration.....	60
4.2. Light distribution geometrics for patterning of proteins.....	63
4.3. Calibration of confocal volume and intensity distribution.....	64
4.3.1. Linearity of detected fluorescence intensity.....	65
4.3.2. Excitation distribution.....	69
4.3.3. Sizes of confocal volumes.....	72

4.4. Discrimination of mono and double Citrine.....	73
4.5. Rapamycin-induced dimerization of FRB and FKBP.....	74
4.6. EGF-induced translocation and dimerization of Erk2.....	79
4.6.1. Wild type.....	79
4.6.2. Inhibition of the Mek-Erk2 interaction.....	86
4.6.3. Erk2(K52R) kinase-deficient mutant.....	91
5. Discussion.....	97
5.1. Implementation.....	100
5.1.1. Hardware.....	100
5.1.2. Software.....	101
5.1.3. Applications.....	102
5.2. Outlook.....	104
5.2.1. Increasing maximal number of processed photon counts per second.....	104
5.2.2. Sequently measurement of different groups of confocal volumes.....	105
5.2.3. Fluorescence Cross-Correlation Spectroscopy (FCCS).....	106
5.2.4. Improvement of the shape of the confocal volumes.....	108
5.2.5. Analysis software.....	110
6. References.....	113
7. Appendix.....	121
7.1. Additional devices.....	121
7.2. Equations.....	122
7.3. Fluorescence Cumulant Analysis (FCA).....	124
7.4. Protocols.....	125
7.5. Software manual with explanations.....	129
8. Acknowledgements.....	167
9. Curriculum Vitae.....	168
10. Statement of Originality.....	169

1. Introduction

Cell, from the Latin word *cella* for “small room”, describes the modules life is build up of. In order to understand the functionality of cells, biology aims to understand how the smallest biological functional units, such as proteins and nucleic acids, function as communication networks, processing collective and modules. These networks consist of a large number of different nodes with complex cross linking and span over large volumes compared to the size of the single actors. Molecules can diffuse or be transported actively and bind to or react with the membrane or other molecules. The mobility and interaction are the two important properties of the molecules that needed to be characterized to understand their function.

Only few measurement techniques allow single molecule observations. As a physical approach, atomic force microscopy (AFM) allows direct visualization of single atoms and molecule deformations. But it is mainly limited to surface characteristics. Depending on the parameter of interest, a robust and more flexible approach is given by fluorescence microscopy (*chapter 1.1*). In this approach, proteins of interest are tagged with fluorophores. Upon excitation with light, fluorophores emit photons of another wavelength which can be separated and detected. In this way, localization and dynamics of proteins can be observed.

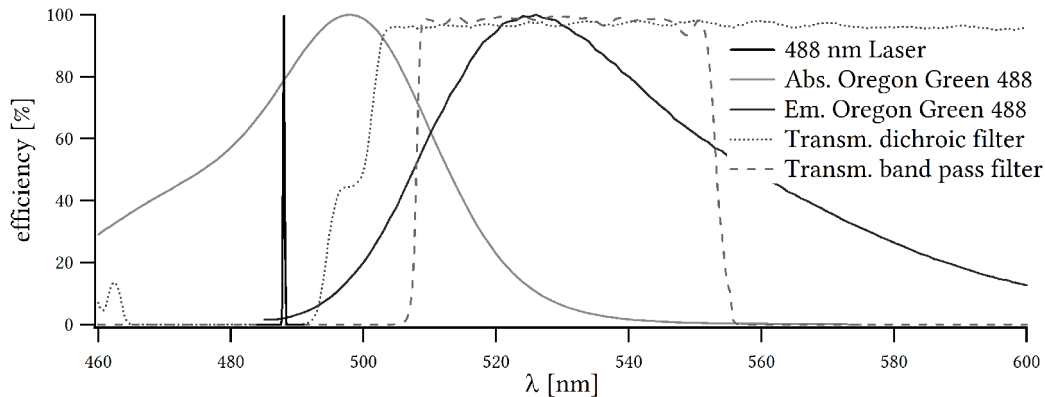
Various fluorescence microscopy techniques provide informations about mobility and interactions of proteins in living or fixed cell samples. Fluorescence Correlation Spectroscopy (FCS) is one method to determine absolute values for concentration and diffusion of fluorescent molecules in a small volume inside the cell, using the intensity fluctuations inside the volume caused by fluorophores crossing the volume (*chapter 1.2*).

The purpose of this work was to develop of a microscope system able to parallelize FCS measurements (*chapter 1.3*) in multiple positions inside a cell, aimed to characterize fast diffusion and dimerization processes inside the cytosol (*chapter 2 & chapter 4*). The microscope system (*chapter 3.1*) is equipped with with an adaptive optical element: a spatial light modulator (*chapter 3.2*). The modulator, a Liquid Crystal on Silicon device (LCoS) (*chapter 3.3*), with adjusted control pattern (*chapter 3.4*) splits illumination to multiple excitation volumes. It utilizes single spots or a line illumination for an automated calibration and alignment of the laser illumination of the microscope (*chapter 3.5*) to a camera or an array of 16 fibers connected to avalanche photon diodes (APD).

1.1. Introduction

1.1. Fluorescence microscopy

Fluorophores, molecules capable of absorbing light and re-emitting light of a longer wavelength, or objects of interest, e.g. proteins, linked to fluorophores can be easily observed in an optical approach. Each fluorophore is characterized by a specific spectra for absorbing and emitting light, depending on the band gap between the excited and the ground state, and a mean lifetime in the excited state, typically in the scale of a few nanoseconds. Using suitable filters and light sources, multiple different fluorophores can be observed in parallel. *f 1.i* shows an example of filters and excitation suitable for the fluorophore Oregon Green 488.

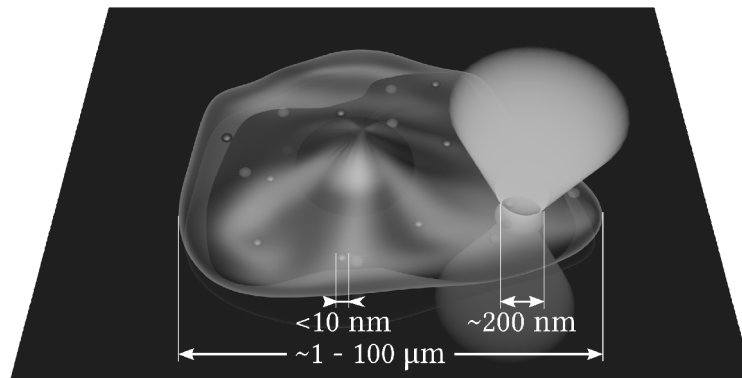


f 1.i: Spectra of absorption and emission of Oregon Green 488 (Invitrogen), excited by a 488 nm laser. Excitation reflected by a dichroic mirror (Semrock Di01-R488) and the emission filtered and transmitted by the dichroic and a band pass filter (Semrock FF01-531/40).

However the lateral resolution of classical microscopy is limited by diffraction, resulting in a minimum distance d between two separable objects depending on the wavelength λ and the numerical aperture NA of the optical system [Abbe 1873]:

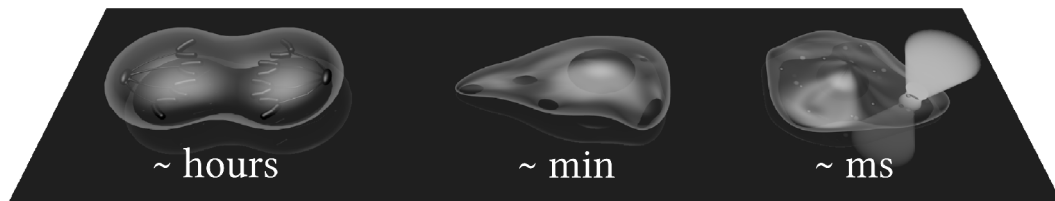
$$d = \frac{\lambda}{2 NA} \quad (\text{e 1.i})$$

For visible light, the typical scale of d is about 250 nm. Therefore classical microscopy is capable of observing a whole cell but cannot resolve multiple proteins below the diffraction limit, e.g. the range of interactions (*f 1.ii*).



f 1.ii: Sizes of cell, proteins and a diffraction limited spot.

Partly due to the length scale, the time scale of cellular processes varies from hours for cell division, over minutes for communication over the range of a whole cell and for resulting cellular behavior (e.g. cell migration), up to milliseconds for single protein interactions and diffusion through a diffraction limited spot (*f 1.iii*).



f 1.iii: Time scale of cell-biology. LTR cell division, migration and protein interactions.

Fluorescence microscopy can avoid this limitation but always struggle with the variety of actors inside a cell, the scales of lateral sizes and the duration of processes. The observed properties in fluorescence microscopy are localization (in up to three dimensions), time and detected emission intensity. The limitations for a specific microscope technique in tracing these parameters are cross bound. Any improvement of the resolution in one of the dimensions can only be achieved in expense of the resolution in one or more different dimensions.

In wide field microscopy, a broad area of a sample is illuminated and the excitation detected. With fast cameras, a high temporal resolution is possible at the expense of the detected excitation and sensitivity. The lateral resolution is diffraction limited, but the localization of single particles in a dilution with less than one particle in average per the diffraction limited volume can be increased if the profile of the detected emission is accurately determined (Super resolution microscopy) [Huang 2009]. The image of a single particle through an optical system

1.1. Introduction

is called the point spread function. Structured illumination microscopy increases the resolution in wide field by superposing multiple images taken with different excitation patterns [Gustafsson 2000] [Hirvonen 2009], thus it reduces the actual frame rate.

In confocal microscopy the light is focused to the diffraction limited volume [Minsky 1957] and scanned over the substrate. A pinhole excludes out of focus emission light, producing optical sectioning. The well defined illumination increases the localization and reduce the background.

For most scanning fluorescence microscopy methods, only lasers offer the desired conditions for coherence, controlled intensity and precise excitation wavelength. Additionally to the wide field illumination and a single spot, the light of a laser can be shaped to slices (Single Plane Illumination Microscopy, SPIM) [Huisken 2004] or aligned in an angle of total reflection (Total Internal Reflection Fluorescence Microscopy, TIRFM) [Ambrose 1956] to reduce the observation to a slice of the substrate or close to the glass (~ 100 nm). In laser scanning microscopy, the effective excitation volume can be reduced by two-photon excitation [Denk 1990]. In this illumination mode, a pulsed laser (~ 100 fs) is focused into the sample to generate a high local density of photons. The wavelength of the light is chosen to supply half the energy needed to excite the fluorophores (typically ~ 800 nm). The probability of co-localisation of two photons increase quadratically with respect to the intensity. Therefore only fluorophores in the focus are excited, achieving lower background and less bleaching. Additionally, due to reduced scattering of the typically infrared excitation light, deeper substrate penetration is possible.

Most observed concentrations inside cells are higher than one fluorophore per observed volume. To determine the position and the track of single fluorophores despite their concentration, photoswitchable fluorophores can be used to reduce the observed concentration. A few fluorophores are capable of being activated or deactivated by a specific wavelength or even could be switched between multiple spectra, in some cases in a reversible manner. Photoactivated Localization Microscopy (PALM) [Betzig 2006] and Stochastic Optical Reconstruction Microscopy (STORM) [Rust 2006] are based on the temporarily reduction of observable fluorescent molecules in the sample and allow single molecule tracking.

Another method to improve the resolution is based on stimulated emission of excited fluorophores in a donut shaped illumination, inhibiting red shifted excitation of parts of a diffraction limited volume (STED) [Klar 2001].

Still, only complex image systems or strongly diluted probes allow single molecule tracking. And in those cases, bleaching, the destruction of the fluorescent capacity, and the compromises of temporal and spatial resolution limitations of the illumination and detection are ongoing matters of system development. Some of the limitations are solvable for fixed, non living samples. For many biological questions, the tracks of single molecules are not necessary, but their distribution, concentration in a certain volume, their flow or their percental interaction with other molecules are sufficient. Many subclasses of fluorescence spectroscopy were developed to determine one or more of these parameters under a wide range of conditions and substrates, mainly depending on the properties of the fluorophores, the excitation illumination, the observed volume and the photon detection.

To show higher density flows from or to a specific location, the disadvantage of bleaching fluorophores on a specific volume can be utilized for Fluorescence Recovery After Photobleaching (FRAP) [Axelrod 1976]. A sequence of images can determine ensemble diffusion rate.

To detect co-localisation of proteins in the range of molecular interactions, another property of fluorophores can be used to overcome the diffraction limitation. Some fluorophores, here called donors, can transmit the energy of their excited state to an other fluorophore nearby, called acceptors. The acceptor needs to have a lower band gap and therefore has a longer excitation wavelength. This process, called Förster Resonance Energy Transfer (FRET) [Förster 1984] [Jares-Erijman 2003], enables co-localisation in a range of a few nm. The transfer of energy can be observed by the decrease of the mean fluorescence life time of the donor fluorophores, because of the additional path to depopulate the excited state. Using a precisely pulsed laser illumination, the fraction of molecules transferring energy to the acceptor can be determined, independent of their absolute concentration, by Fluorescence-Lifetime Imaging Microscopy (FLIM) [Wouters 2001]. But also other conditions are known to quench fluorescence, e.g. molecular oxygen [Kautsky 1939].

The temporal resolution and sensitivity of the fluorescence microscope systems are highly dependent of the detector. For each method a compromise between quantum efficiency, noise ratio, spatial and time resolution has to be found. Is the measured parameter independent of the intensity profile, non-linear light amplifier are usable. In some cases, the detection is modulated and linked to an illumination modulation (e.g. FLIM). Mainly the detectors could be

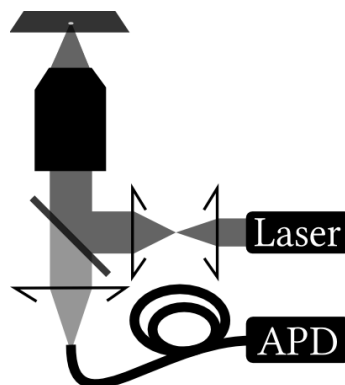
1.1. Introduction

separated in area detectors (cameras) and highly quantum efficient point detectors (e.g. avalanche photon detectors), although recently a cross-overs, single-photon avalanche photodiode arrays (SPAD) are released.

An extensive description about fluorophores, used light sources, detectors and methods can be found in “Principles of Fluorescence Spectroscopy” [Lakowicz 2006] and references therein.

1.2. Fluorescence Correlation Spectroscopy (FCS)

One method for high resolution temporal analysis of low concentrated fluorophores is Fluorescence Correlation Spectroscopy (FCS) [Madge 1972]. The method bases on fluorescence intensity fluctuations, e.g. caused by molecules crossing a small measurement volume. In most cases, a diffraction limited volume of about 1 fl is used [Rigler 1993] (*f 1.iv*).

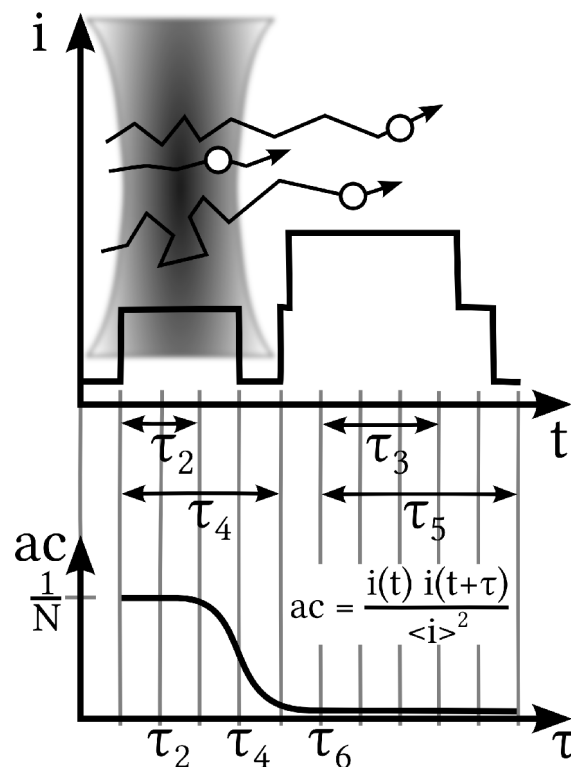


f 1.iv: Scheme of confocal FCS system with laser illumination and a fiber as pinhole, coupled to an avalanche photo diode (APD) detector.

In theory, FCS can determine any parameter resulting in such fluctuations, and therefore the diffusion rate of fluorophores crossing the volume, in one part of the substrate. The duration of freely diffusing fluorophores in the volume is in the range of about 100 microsecond. Due to Poisson statistics, also the concentration of the fluorophores is given. Scanning over the substrate, a map of precise diffusion rate and concentration can be determined, albeit in a too low temporal resolution for mapping many processes in the cytosol of the cell. To obtain accurate statistics from the fluctuations, each measured position typically takes about 10 s.

During the measurement, the time of arrival relative to the starting of the measurement is logged for each detected photon. Due to the finite time resolution of the detector, the arrival

times are already binned to short intervals (typically 50 ns - 2 μ s). After the measurement, the number of photons per interval, the intensities, at each time point are compared to the photon counts of those intervals with a specific relative time delay. The product of these intensities for the specific time delay, normalized by average intensity squared, is the autocorrelation. Plotting the autocorrelation against the delay time, a characteristic autocorrelation curve starts at zero delay with the normalized variance of the fluctuation, decline at the time delay, the fluorophores need to diffuse across the detection volume and ideally converge at the long time fluctuations to no correlation (*f 1.v*). The slope is broadened by the distribution of the diffusion rate and the ellipsoidal geometry of the detection volume. Additionally the inverse of the autocorrelation at time delay zero equals the number of fluorophores.



f 1.v: Principle of FCS. Confocal volume with particle tracks on the top, resulting in an intensity (i) time trace (t). Autocorrelation (ac) as a function of the time delays τ at the bottom. The curve shows a mean diffusion time of τ_4 and the particle number N .

This method is one foundation of this work and is described in more detail in *chapter 2*.

1.3. Introduction

1.3. Spatial Resolved Fluorescence Correlation Spectroscopy (SRFCS)

The main disadvantage of FCS is the limited spatial information. Scanning a confocal volume to measure on multiple positions, the time resolution between succeeding measurements decrease (sFCS) [Petersen 1986]. Only parallelizing the detection can increase spatial information in scale without losing time information. In Image Correlation Microscopy, whole images taken with a wide field illumination (ICS), are correlated in time to map dynamics [Petersen 1993] [Wiseman 2004]. This method is mainly used to observe slowly diffusing membrane proteins.

For faster diffusion, ICS methods with faster acquisition were developed to parallelize or to enlarge the observed volumes. The methods can be cataloged in relation to the used detector and the shape of the detection volumes [Conchello 2005]. Each represent a compromise about spatial and temporal resolution and signal-to-noise ratio. Most systems are based on EM-CCD cameras, which are high quantum efficient, but much slower in frame rate than the detection rate of a avalanche photo diode. As a result, still only comparable slow fluctuations are measurable. Additionally, cross talk between pixels and stray light have to be considered and limit the achievable resolution.

The Spinning Disk Confocal Microscope parallel the principle of the single 3D Gaussian confocal microscope by aligning a disk formed pinhole array and a disk formed microlens array. The laser illumination is split by the lens array and focused through the pinholes before the objective. The emission collected by the objective has to pass the pinhole array again, before reflected to the camera. The disks are rotating and depending on the frame rate up to 10^5 locations can be measured per frame [Sisan 2006]. Reducing the number of rows used of the camera, the speed can be improved by cost of the number of used detection volumes, e.g. using 10 volumes at 3300 Hz [Needleman 2009]. Besides from the speed, this method suffers from the sizes and converging of the single beams focussed by the objective, because a broader and collimated beam could be focused better [Hess 2002].

The spatial and temporal fluctuation microscope (STFM) uses a line as illumination and detection volume. The line-shaped illumination is created using a cylindrical lens and a line-shaped spatial filter in front of the objective. The same objective, lens and spatial filter is used

for the detection [Heuvelman 2009]. Illuminating a line of pixels, crosstalk and diffusive light between detecting pixels are unavoidable and increase the detection volume. This method is basis for the two following methods, which reduce the detection volume further.

Single Plane Illumination Fluorescence Correlation Spectroscopy (SPIM-FCS) uses a cuboid as detection volume and reduces the size of the observed line-shaped volume with a second objective for detection, perpendicular to the illumination plane [Wohland 2010]. The excitation is passing another cylindrical lens and a line shaped spatial filter before reaching the camera. Using a single line of the camera, the frame rate can be increased up to 25 kHz [Capoulade 2011].

Spatially resolved total internal reflection fluorescence correlation microscopy (TIR-FCM) combines a line-shaped illumination with a total internal reflection angled illumination [Kannan 2007].

To overcome the time resolution limitations of the EM-CCD camera, the detector has to be replaced. An attempt for fast single photon counting combines of a photon counting image intensifier coupled to a fast CMOS camera and a pulsed illumination, enabling detecting single photon arrivals at up to 250 kHz [Sergent 2010] [Petrášek 2010]. But with the release of single-photon avalanche photodiode arrays (SPAD), the benefits of APDs are combined with a resolution of some 'pixels'.

A SPAD array can parallelize the detection without losing temporal resolution. Using a spatial light modulator (SLM) to create an appropriate illumination, FCS could be parallelized even for fast fluctuations [Colyer 2010] [Colyer 2011]. The SPAD array detectors themselves are the detection pinholes. The light splitting is implemented by a lens array created with a SLM. Each single beam has a very small waist, which can be less focused [Hess 2002], and its phase front further disrupted by digitalized low resolution lenses. As a consequence, cross talk caused by diffusive focused light limits the actual resolution.

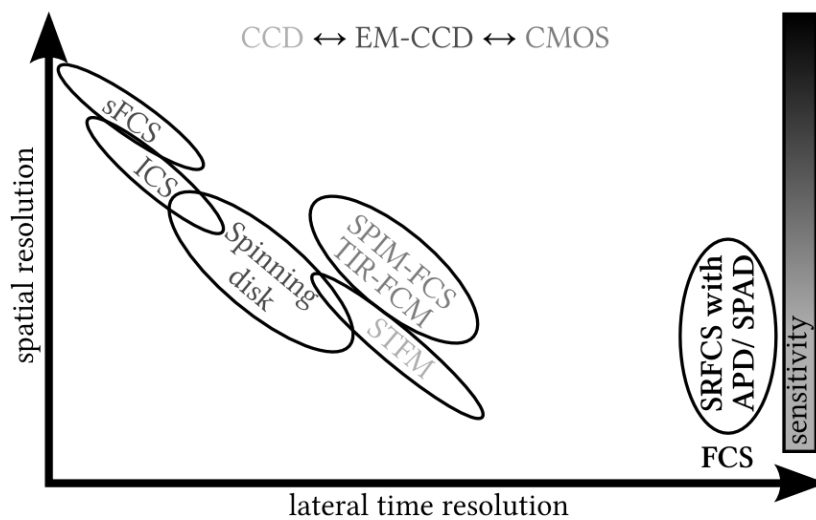
In an attempt of using of a SLM and conventional APDs with fibers as pinholes to create two separated confocal volumes to cross-correlate these volumes, the fibers were manually aligned accordingly to the illumination [Blancquaert 2008].

1.3. Introduction

Despite the attempts to overcome the spatial limitations of classic confocal FCS or replace FCS for certain issues, only parallelizing of measurements and APD detection can provide high temporal resolution and sensitivity for fast diffusing species in multiple positions (*f 1.vi*).

Our own approach for parallelizing FCS will adapt to the idea of using fibers as pinholes with conventional APDs as detectors and a SLM for illumination splitting and alignment. A fiber array with 16 fibers serves as an array of pinholes. A fiber array has the benefit of separated pinholes from the detector. It can be replaced to change their localization or diameter of the pinholes, or suit different ranges of wavelength. Moreover the separation simplifies further development to FCCS, as the same pinholes can be used for the detection volumes of both wavelengths.

The fibers of a solid fiber array can not be aligned to the illumination. Therefore the illumination has to be aligned to fit the fiber positions. For the optimal size of the confocal volumes, collimated beams of the width near to the size of the back focal plane of the objective are used. The alignment is automated and stable, compensating small misalignments of optics. It can be used for the visible range of wavelengths without manual alignment. Because of the well encircled fibers and the strong focus, no cross talk between the volumes occurs.



f 1.vi: Coarse comparison of SRFCS methods in resolution and sensitivity. The diffusion time resolution is primarily dependent on the detector: CCD → CMOS → EM-CCD → APD/ SPAD.

The equipment is designed to observe diffusion of tagged proteins in the cytosol of cells. Due to its robustness and an automated calibration and alignment, it can be used by various operators after short instruction.

1.4. Spatial Light Modulator (SLM)

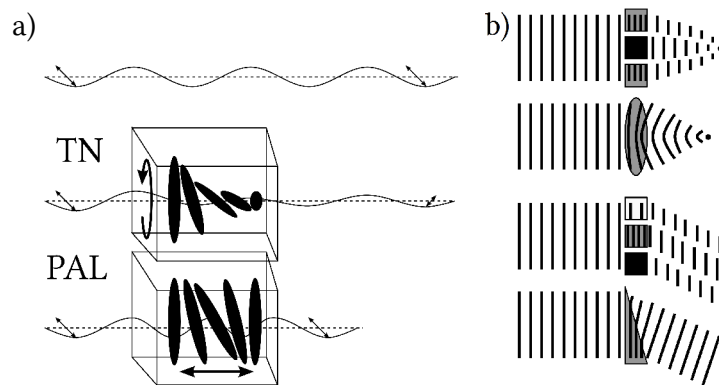
Non motorized mirrors, lenses, gratings and prisms are typical parts of optical systems to shape and deflect light in specific fixed directions. Other devices, like acousto-optic-tunable filters (AOTF), are highly flexible and their influence on the beam can be changed in time. The need to adapt the wavefront, for example to correct low-order aberrations in astronomy, brought deformable mirror-surfaces and micromirror devices (DMD), which have a low lateral resolution but are highly reflective and have a large fill factor. Another sort of devices to form the wavefront originate from Liquid Crystal Devices (LCD), well known as a display technology. LCDs can be produced as translucent or reflective devices, later ones named Liquid Crystal on Silicon (LCoS). Although LCD-devices are produced with fairly high resolutions, the efficiency of these devices can vary and due of the mechanism of action they are dependent of the polarization of the incoming light. Reflective LCDs can reach shorter reaction times, higher resolution and fill factors as the addressing circuitry can be positioned behind the optical elements.

Because of their ability to modulate the wavefront in a spatial resolution, DMDs and LCDs are called Spatial Light Modulators (SLM).

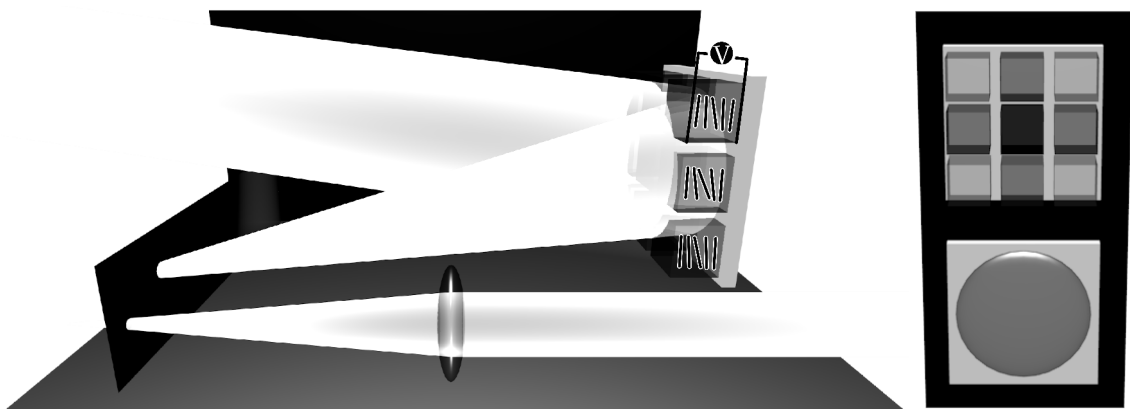
SLMs have to be classified according to two sorts of wavefront alterations, the amplitude modulation and the phase modulation. DMDs create purely phase modulation and only indirect due to the phase modulation an amplitude modulation. LCDs known from displays as calculators or watches create a mostly amplitude modulation. Other LCDs are also capable of phase modulation.

LCD can be produced with different crystals. Ferroelectric liquid crystals can switch very fast between two states, but only support a binary phase modulation. Twisted nematic (TN) materials were primary developed for video projection and are therefore enhanced for amplitude modulation. The illumination light passes a polarizing filter, the crystals rotate the polarization of the transited light and the light is passing a polarizing filter again, excluding a part of the illumination. Parallel aligned nematic (PAL) materials are most suitable for phase modulation (*f 1.vii*) (*f 1.viii*).

1.4. Introduction



f 1.vii: a) Alignment of TN and PAL based LCD pixels and b) the co-action of multiple phase modulating pixels to emulate optical elements as a lens (top) and a prism (bottom).



f 1.viii: Functionality of a PAL LCoS with 9 pixels compared to a lens. A specific voltage connected to each pixel rotates the liquid crystals parallel to each other, in the plane perpendicular with the light polarization and changes the optical density. Interference of light passing different pixels cause diffraction effects, e.g. like a lens. On the right side: the LCoS digitalizes the phase gradient of a classical lens. The pixel pitch acts like a grating.

Using a phase modulating LCoS offers many possibilities. In microscopy, depending of the position in the excitation path or in the imaging path or both, it can structure the illumination rapidly, or work as realtime fitting Fourier-filter. It is possible to use phase contrast methods, form different point spread functions (PSF), improve lateral and vertical resolution and achieve a fast 3D resolution. A good overview can be found in [Maurer 2010] and references therein. The low light efficiency of the LCoS device hinders the usage of such a device in the emission path while measuring low numbers of fluorophores.

It can also be used to correct for defects of the optical path or to split the light paths. Splitting the light and aligning a defined light distribution is e.g. used for light induced patterning on surfaces [Belisle 2009] and for optical tweezers [Neuman 2004].

While there are different ways to achieve multiple focused spots, commonly used as optical traps, mostly a holographic setup is chosen. A lens causing a Fourier transformation process the holographic pattern into the desired light distribution in the substrate plane. Various algorithms to calculate the holograms can be found in the literature, each with its own benefits and drawbacks in calculation speed and distribution quality [Leonardo 2007]. For small numbers of desired focused points, a fast solution can be achieved by using a combination of simple single holograms per focus point, prism and lenses, and adding these patterns to a single hologram (superposition algorithms). As drawbacks, these methods produce unwanted additional focus points due to pattern symmetries and low intensity uniformity between the spots. As a reverse method, the direct-search algorithm and simulated annealing could start with a known holographic pattern, but reduce the optimization to a high number of pattern changes and a try and error method. To find the best result, also changes resulting in a worse light distribution have to be considered initially. Measuring the magnitude of influence of changes and evolved algorithms, the required number of steps can be reduced. As a major benefit, this algorithm corrects for the optics of the whole beam path, including the imperfect mirror surface inside an LCoS.

The mirror surface of the LCoS is one of the drawbacks of these devices. Using a direct search algorithm, a phase front reading device or comparing a well known hologram with the resulting light distribution, it is possible to correct for it to a certain resolution. Another downside is the finite number of pixels and phase step size and a small phase range of, in most devices, 2π . The limitation of the range of the phase is easily overcome by taking the modulo of the phase value and breaking the pattern like done in Fresnel lenses. The influence of the digitization into pixels and phase steps can be reduced by using big holograms, e.g. avoiding the fragmentation of the pixels between multiple small patterns. A last, but for most applications unimportant negative effect of the liquid crystal based devices should be kept in mind, is that the alignment of the crystals can not stay constant for a long time without damaging them. Therefore together with the crystals, the efficiency of the devices oscillate in time, resulting in a fast oscillating illumination intensity while using in an illumination path.

2. Fluorescence Correlation Spectroscopy (FCS)

In this method fluorescence intensity fluctuations are measured. The signals collected are the detector arrival times of photons induced by single fluorophores entering or leaving the detection volume atop of counts created by other fluorophores and noise of the detector. From these data, the number of particles and the diffusion rate can be determined by calculating the autocorrelation (*chapter 2.1 & chapter 2.2*). The same data can also be processed with other algorithms, e.g. PCH or cumulant analysis (*chapter 2.3*).

In solitary cells, the pool of fluorophores during a measurement is strictly limited. Illumination will induce bleaching and can influence the measurement. A system for measurements inside cells have to fulfill a balance between signal and noise and prevent impact on the measured parameters (*chapter 2.4*).

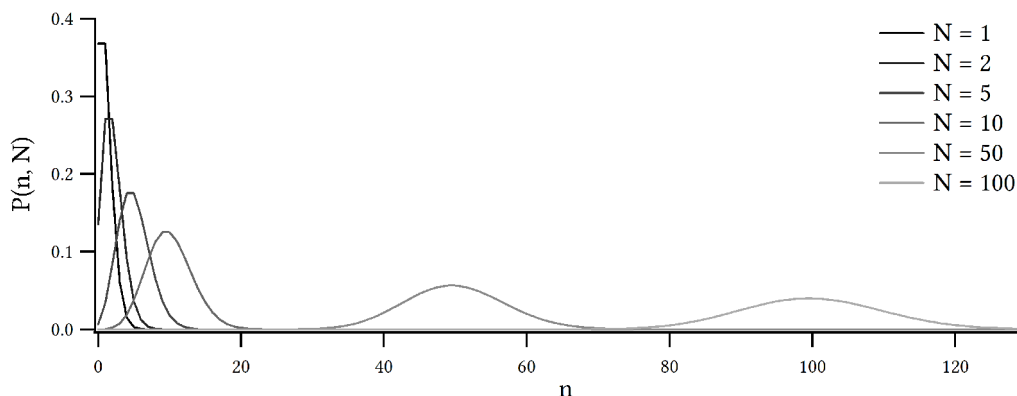
2.1. Fluorescence Correlation Spectroscopy (FCS)

2.1. Autocorrelation and diffusion model

FCS in a standard confocal microscope measures the fluorescent intensity fluctuations of free diffusion fluorophores in an ellipsoidal volume. In case of other shaped volumes, the diffusion model has to be adapted. If not declared otherwise, the chapter is based on [Lakowicz 2006]. In first approximation, assuming linear efficiency in detection and low concentrations of fluorophores, the detected intensities are proportional to the number of fluorophores. The occurrence of fluorophores in the volume for low concentrations are random discrete and binary events. Therefore they can approximately be described by the Poisson distribution. The probability P of n fluorophores in a volume with an average number of N fluorophores in the volume is given by:

$$P(n, N) = \frac{N^n}{n!} e^{-N} \quad (\text{e } 2.i)$$

The distribution broadens for an increasing average number of fluorophores (*f 2.i*), illustrating the significance of low numbers of fluorophores inside the volume. A compromise between total signal against background noise and signal fluctuations against noise has to be found.



f 2.i: Poisson distribution (e 2.i) for $N = 1, 2, 5, 10, 50$ and 100 .

To quantify the fluctuations, the intensity $F(t)$ at a given time t is compared with the intensity $F(t+\tau)$ with the time shift τ . For τ short compared to the time a fluorophore needs to cross the volume, the probability, that most of the fluorophores detected at time point t are still in the volume is high. Therefore the intensities $F(t)$ and $F(t+\tau)$ are similar. These similarities can be

2.1. Fluorescence Correlation Spectroscopy (FCS)

quantified by the autocorrelation. The value of the autocorrelation $R(\tau)$ for a specific τ is given by the product of the intensities $F(t)$ and $F(t+\tau)$ for all time points t of the measurement with a total length of T :

$$R(\tau) = \frac{1}{T} \int_0^T F(t) F(t+\tau) dt = \langle F(t) F(t+\tau) \rangle \quad (\text{e 2.ii})$$

The intensities can be replaced by their variance $\delta F(t)$, the fluctuations around the mean value $\langle F \rangle$:

$$\delta F(t) = F(t) - \langle F \rangle \quad (\text{e 2.iii})$$

In FCS, the autocorrelation normalized by average intensity squared is named autocorrelation function $G^*(\tau)$:

$$G^*(\tau) = \frac{\langle F(t) F(t+\tau) \rangle}{\langle F \rangle \langle F \rangle} = 1 + \frac{\langle \delta F(t) \delta F(t+\tau) \rangle}{\langle F \rangle^2} = 1 + G(\tau) \quad (\text{e 2.iv})$$

Due to the Poisson distribution, for the autocorrelation at $\tau = 0$ results:

$$G(0) = \frac{\langle \delta F(0) \delta F(0) \rangle}{\langle F \rangle^2} = \left(\frac{\sqrt{\langle (\delta F)^2 \rangle}}{\langle F \rangle} \right)^2 = \left(\frac{1}{\sqrt{N}} \right)^2 = \frac{1}{N} \quad (\text{e 2.v})$$

providing the average number of particles N in the sample.

To evaluate an autocorrelation, the data series should be time invariant and therefore the process monitored need to be reversible. This is achieved by approximation for $T \gg \lambda$ with λ the fluctuation period, although for long T , photobleaching of the fluorophores is predominant. The trace should be continuously, approximated by $\lambda \gg \Delta\tau$ with $\Delta\tau$ as time binning, and infinite. While a finite measurement duration in most cases affect accuracies, it influences the autocorrelation depending on τ because with increasing τ , less time intervals could be correlated.

To connect the fluctuations to physical variable, a model of the intensity fluctuations can be derived and fitted to the measured autocorrelation later on.

2.1. Fluorescence Correlation Spectroscopy (FCS)

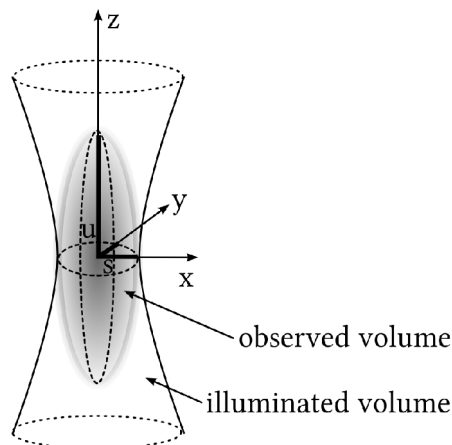
The observed brightness per fluorescent molecule B depends on the quantum efficiency for detection q of the emitted photons, the cross-section for absorption σ , and the quantum yield for emission of the fluorophore Q :

$$B = q \sigma Q \quad (\text{e 2.vi})$$

It is therefore not alone a molecular property of the fluorophore, but also depends on illumination and detection. The measured intensity $F(t)$ also not only depends on the brightness B and the actual fluorophore distribution $C(\vec{r}, t)$, but on the spatial distribution of the collection efficiency $\eta(\vec{r})$ and the excitation intensity $I(\vec{r})$. It is given by the integral of the fluorophore concentration over the observed volume:

$$F(t) = B \int_{\mathbb{R}^3} \eta(\vec{r}) I(\vec{r}) C(\vec{r}, t) d\vec{r} \quad (\text{e 2.vii})$$

$\eta(\vec{r})$ and $I(\vec{r})$ are instrumental parameters. For simplification, it is assumed the system work in a range where no overexposure occur and therefore $\eta(\vec{r})$ is independent of $I(\vec{r})$. Together, they form the detection profile $p(\vec{r})$. For a confocal microscope, a three dimensional Gaussian is assumed for $p(\vec{r})$, with a circle in x - y with the radius s and an ellipse along the optical axis z with a half length of u (f 2.ii). The radius s and the length u refer to a decrease to e^{-2} of the maximum illumination intensity I_0 :



f 2.ii: Geometry of a confocal volume. Characteristic scales are $s \cong 0.25 \mu\text{m}$, $u \cong 1 \mu\text{m}$, spanning a volume of about 0.35 fl.

$$p(\vec{r}) = I_0 \exp\left(-2(x^2 + y^2)/s^2\right) \exp(-2z^2/u^2) \quad (\text{e 2.viii})$$

2.1. Fluorescence Correlation Spectroscopy (FCS)

Because of the inhomogeneous intensity, the actual position of the fluorophore influences the autocorrelation function. With \vec{r} the position of the fluorophore at time point t and \vec{r}' the position at time point $t+\tau$, the autocorrelation function becomes:

$$G(t, \tau) = \frac{\langle \delta F(t) \delta F(t+\tau) \rangle}{\langle F \rangle^2} = \frac{B^2 \iint_{\mathbb{R}^3} p(\vec{r}) p(\vec{r}') \langle \delta C(\vec{r}', t) C(\vec{r}, t+\tau) \rangle d\vec{r} d\vec{r}'}{\left(B \langle C \rangle \int_{\mathbb{R}^3} p(\vec{r}) d\vec{r} \right)^2} \quad (\text{e 2.ix})$$

The brightness B can be canceled out. The autocorrelation is independent of B , but still, the signal $F(t)$ (e 2.vii) to noise ratio (detector noise and stray light) is not.

$\delta C(\vec{r}, t)$ has to be adapted to the type of the fluctuations. It differs for the boundary conditions of a diffusion or chemical processes that changes the brightness of fluorophores. The fluctuations in the local concentration caused by molecular diffusion are covered by Fick's Second Law [Fick 1855] with the diffusion coefficient D :

$$\frac{\partial}{\partial t} C(\vec{r}, t) = D \nabla_{\vec{r}}^2 C(\vec{r}, t) \quad (\text{e 2.x})$$

$$\frac{\partial}{\partial t} (\delta C(\vec{r}, t) - \langle C \rangle) = D \nabla_{\vec{r}}^2 (\delta C(\vec{r}, t) - \langle C \rangle) \quad | \quad \frac{\partial}{\partial t} \langle C(\vec{r}, t) \rangle = 0 \quad \wedge \quad \nabla_{\vec{r}}^2 \langle C \rangle = 0 \quad (\text{e 2.xi})$$

$$\frac{\partial}{\partial t} \delta C(\vec{r}, t) = D \nabla_{\vec{r}}^2 \delta C(\vec{r}, t) \quad (\text{e 2.xii})$$

The conditions set at (e 2.xi) are given, because the thermodynamic mean concentration of the fluorophore $\langle C \rangle$ is independent of position and time.

The differential equation can be solved in Fourier space [Elson 1974], see appendix (a 2.i):

$$\delta C(\vec{r}, \tau) = \int_{\mathbb{R}^3} e^{i\vec{\rho}\vec{r}} \frac{1}{(2\pi)^3} \int_{\mathbb{R}^3} e^{-i\vec{\rho}\vec{r}''} \delta C(\vec{r}'', 0) d\vec{r}'' e^{-\vec{\rho}^2 D \tau} d\vec{\rho} \quad (\text{e 2.xiii})$$

The autocorrelation $\langle \delta C(\vec{r}', t) \delta C(\vec{r}, t+\tau) \rangle$ can now be calculated. Because the autocorrelation is only dependent on τ and for reduction of the following calculations, t is set to 0:

$$\begin{aligned} \langle \delta C(\vec{r}', 0) \delta C(\vec{r}, \tau) \rangle &= \left\langle \delta C(\vec{r}', 0) \int_{\mathbb{R}^3} e^{i\vec{\rho}\vec{r}} \frac{1}{(2\pi)^3} \int_{\mathbb{R}^3} e^{-i\vec{\rho}\vec{r}''} \delta C(\vec{r}'', 0) d\vec{r}'' e^{-\vec{\rho}^2 D \tau} d\vec{\rho} \right\rangle \\ &= \frac{1}{(2\pi)^3} \int_{\mathbb{R}^3} e^{i\vec{\rho}\vec{r}} \int_{\mathbb{R}^3} e^{-i\vec{\rho}\vec{r}''} \langle \delta C(\vec{r}', 0) \delta C(\vec{r}'', 0) \rangle d\vec{r}'' e^{-\vec{\rho}^2 D \tau} d\vec{\rho} \end{aligned} \quad (\text{e 2.xiv})$$

2.1. Fluorescence Correlation Spectroscopy (FCS)

To obtain sufficient intensity fluctuations, the experiments are done with very diluted solutions. The statistics of the single fluorophores are therefore independent and the spatial correlation length of concentration fluctuations must be very small. Therefore the average correlation between molecules at positions \vec{r}' and \vec{r}'' is about zero, unless $\vec{r}' = \vec{r}''$. Therefore the correlation term can be simplified with the Dirac delta function. Since the distribution of fluorophores inside the confocal volume are determined by Poisson statistics, the mean-square fluctuation of C equals its mean [Elson 1974]:

$$\begin{aligned} \langle \delta C(\vec{r}', 0) \delta C(\vec{r}'', 0) \rangle &= \langle \delta C(\vec{r}', 0) \delta C(\vec{r}', 0) \rangle \delta(\vec{r}' - \vec{r}'') \\ &= \langle C \rangle \delta(\vec{r}' - \vec{r}'') \end{aligned} \quad (\text{e 2.xv})$$

Inserting (e 3.xv) into (e 3.iv) yields (a 2.ii) to:

$$\langle \delta C(\vec{r}', 0) \delta C(\vec{r}, \tau) \rangle = \frac{\langle C \rangle}{(4\pi D\tau)^{3/2}} e^{-\frac{(\vec{r}-\vec{r}')^2}{4D\tau}} \quad (\text{e 2.xvi})$$

Inserting (e 2.xvi) and (e 2.viii) into (e 2.ix) results into the formula used to fit the autocorrelation of the intensity trace (a 2.iii):

$$\begin{aligned} G(\tau) &= \frac{1}{\langle C \rangle s^2 u \pi^{3/2}} \left(\frac{1}{1 + \frac{4D\tau}{s^2}} \right) \sqrt{\frac{1}{1 + \frac{4D\tau}{u^2}}} \quad \left| \begin{array}{l} \pi^{3/2} s^2 u = V_0 \\ \frac{s^2}{4D} = \tau_D \end{array} \right. \\ &= \frac{1}{\langle C \rangle V_0} \left(\frac{1}{1 + \frac{\tau}{\tau_D}} \right) \sqrt{\frac{1}{1 + \left(\frac{s}{u}\right)^2 \frac{\tau}{\tau_D}}} \quad \left| \begin{array}{l} \langle C \rangle V_0 = \bar{N} \\ \frac{u}{s} = \sigma_s \end{array} \right. \\ &= \frac{1}{\bar{N}} \left(\frac{1}{1 + \frac{\tau}{\tau_D}} \right) \sqrt{\frac{1}{1 + \frac{1}{\sigma_s^2} \frac{\tau}{\tau_D}}} \end{aligned} \quad (\text{e 2.xvii})$$

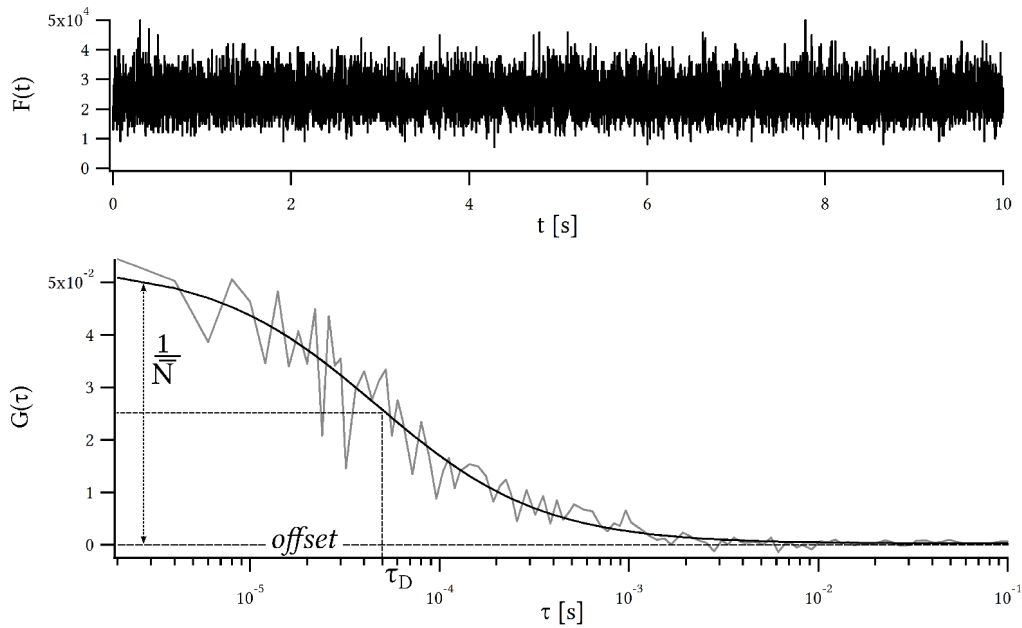
$\underbrace{\hspace{1.5cm}}_{G(0)} \quad \underbrace{\hspace{3.5cm}}_{D(\tau)}$

The volume V_0 of the confocal volume can be defined with different thresholds, resulting in different factors for the mean number of particles \bar{N} , resulting from the mean concentration $\langle C \rangle$ times V_0 . In this work, it is defined as given here. The mean number of particles in the volume therefore equals the inverse of the amplitude of the autocorrelation at $\tau = 0$. Using equation (e 2.xvii) + offset, the parameters amplitude $G(0)$, diffusion time τ_D , structure

2.1. Fluorescence Correlation Spectroscopy (FCS)

parameter σ_s and the offset of the lowest calculated correlation are fitted to the measured data (f 2.iii). The impact of the structure parameter in the fit is smaller than the other parameters and therefore the fitted value can vary more (f 2.iv).

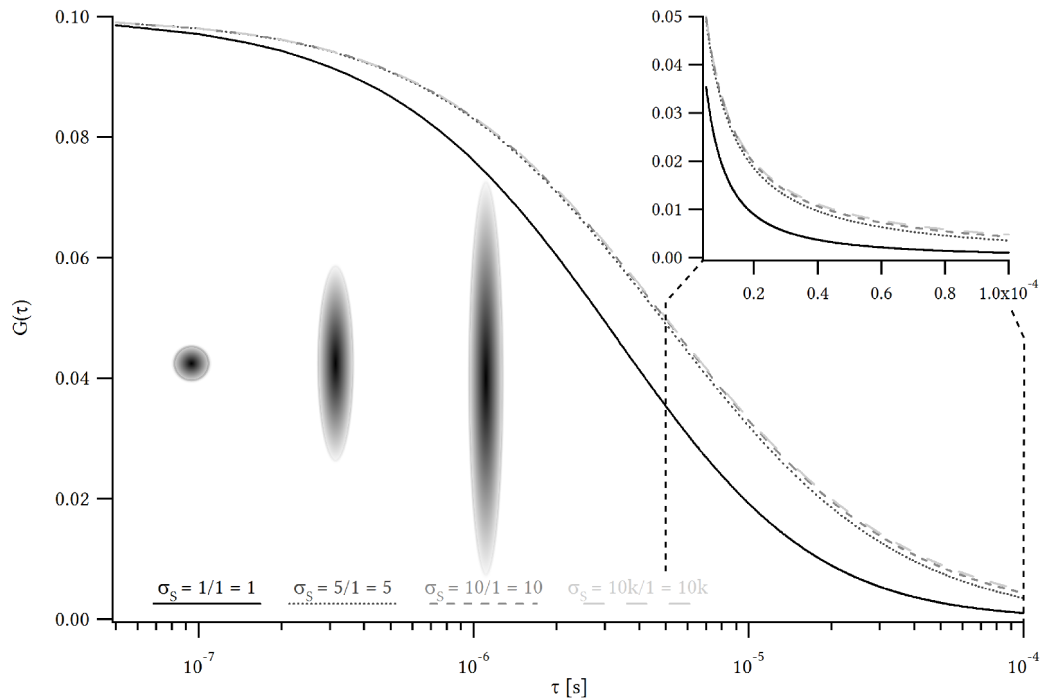
The *offset* is needed because the normalization of the measured autocorrelation is sensitive to long time intensity changes, like slow bleaching of the fluorophores or cell movement.



f 2.iii: Example of an FCS measurement, showing photon counts (top) and the corresponding autocorrelation $G(\tau)$ (bottom) with fitting parameter \bar{N} , τ_D and offset.

The structure parameter σ_s influences the position and the slope of the curve, because an increasing length of a single axis results in a broadened distribution of path lengths inside the volume. This effect compete with τ_D (position of slope) and impulses constraining free three dimensional diffusion, e.g. active transport, two dimension limited or hindered diffusion (changing slope).

2.1. Fluorescence Correlation Spectroscopy (FCS)



f 2.iv: Influence of the structure parameter σ_s on simulated diffusion curves for (curves LTR) $\sigma_s = 1$ (sphere), $\sigma_s = 5$ (typical range), $\sigma_s = 10$ and $\sigma_s = 1 \cdot 10^4$ (with $\bar{N} = 10$, $\tau_D = 5 \cdot 10^{-6}$ s and offset = 0). Upper right: section with linear scale.

2.2. Modifications of the diffusion model

The idealized diffusion model of one species of fluorophores inside a three dimensional Gaussian volume is invalid as soon as additional effects rise. To determine impulses constraining free three dimensional diffusion, in case of varying geometry of the measured volume, of multiple species of fluorophores or completely different origins of fluctuations, the model has to be adapted [Lakowicz 2006]. For example, if two different species of fluorophores with varying diffusion time τ_D are present, the autocorrelation shows an additional shoulder and the fitting model has to consider the two diffusion times and the concentrations of both species. Without a sufficient difference in τ_D , two species of one excitation wavelength can not be resolved as separate species. Fluorophores also have an excited triplet state with long lifetime due to a transition forbidden by quantum mechanics. The effect rise with the illumination intensity and the number of photons excited per fluorescent molecule per time. The resulting light fluctuations emulate a fast diffusing fraction of fluorophores.

2.2. Fluorescence Correlation Spectroscopy (FCS)

Of special interest is the dimerization of fluorescent tagged molecules in which two monomers diffuse together through the confocal volume. If all molecules dimerize, the (mean) number of molecules \bar{N} is halved and the number of fluorophores per molecule doubles. Since the total number of fluorophores and emitted total intensity $F = \int F(t) dt$ is constant, the number of photons emitted per molecule $F/\bar{N} = n$ also doubles. In most cases only a fraction of the molecules dimerize and therefore:

$$\begin{aligned}
 \bar{N}_{after} &= \frac{1}{\xi} \bar{N}_{before} \\
 F_{before} &= F_{after} \\
 n_{after} &= \xi n_{before} \\
 &\text{with } 1 < \xi \leq 2
 \end{aligned}
 \tag{e 2.xviii}$$

The increase of volume and mass and decrease of molecule concentration due to dimerization is not high enough to influence the diffusion time τ_D in a measurable scale. A gain in mass by factor M affects the diffusion coefficient D by a factor of about $M^{1/3}$, e.g. in dimerization by a factor of 1.26 [Lakowicz 2006], with $\tau_D \sim 1/D$. The diffusion model for one species is sufficient to gain the total number of particles and the diffusion time, but it is difficult to distinguish between monomers, dimers or further bonded oligomers.

Expanding the measurement to fluorescence cross-correlation spectroscopy (FCCS), detecting co-diffusion and connected movement of multiple fluorophores is possible [Bacia 2003]. For this method, two varying autocorrelations for two different fluorophores of separated emission wavelength are detected and both data sequences correlated. It is not scope of this work to implement FCCS, but a possible upgrade will be presented in the outlook.

2.3. Fluorescence Correlation Spectroscopy (FCS)

2.3. Alternative analysis methods for fluctuation data

Other algorithms were developed to process FCS data. A parameter derived from FCS measurements is the brightness (counts per particle). In FCS, the diffusion time can be used to separate two species of fluorophores inside a single measurement. The brightness per molecule is a weighted average over the separated species. While temporal resolution, as needed for determining the diffusion time, can be described best by autocorrelation, the amplitude of the fluctuations is characterized by probability distribution. As shown for FCS, the average number of particles can be determined from the detected mean intensity and its variance (e 2.v). Some methods furthermore use the relation between the variance of the mean intensity and the brightness per molecule to separate species of varying values.

Data acquired by ICS can gain from utilizing the variance in Number and Brightness analysis (N&B) [Digman 2008], because the variance is independent from the frame rate of the measurement, even though the sampling rate has still to be small compared to the diffusion time of the fluorophores and the measurement duration short compared to global changes.

For Photon Counting Histogram (PCH), the histogram of the photon counts is fitted by a model of convolved probability distributions of counts from single particles inside a confocal volume [Chen 1999]. The probability distribution per particle comply with a Poisson distribution (e 2.i) in each point of the volume, assuming the particles are not moving during the sampling time.

Fluorescence Cumulant Analysis (FCA) evaluates the factorial cumulants of the photon counts [Müller 2004]. The cumulants of a probability distribution provide an alternative mathematical series ($\kappa_{[1]}$, $\kappa_{[2]}$, ...) for the moments (mean, variance, ...) of the distribution. The factorial cumulants can be calculated from the moments of the photon counts k per time bin:

$$\begin{aligned}\kappa_{[1]} &= \langle k \rangle \\ \kappa_{[2]} &= \langle \Delta k^2 \rangle - \langle k \rangle \\ \kappa_{[3]} &= \langle \Delta k^3 \rangle - 3 \langle \Delta k^2 \rangle + 2 \langle k \rangle \\ \kappa_{[4]} &= \langle \Delta k^4 \rangle - 6 \langle \Delta k^3 \rangle - 3 \langle \Delta k^2 \rangle^2 + 11 \langle \Delta k^2 \rangle - 6 \langle k \rangle\end{aligned}\tag{e 2.xix}$$

An advantage of cumulants is the linearity in summing cumulants of statistically independent variables. The cumulants of the sum of statistically independent variables, e.g. multiple

2.3. Fluorescence Correlation Spectroscopy (FCS)

particles or even varying species, is equal to the sum of the cumulants of the individuals. This reduces the calculations for the cumulants of the counts emitted by diffusing particles in a defined volume to:

$$\kappa_{[r]} = \gamma_r \sum_{i=1}^s \varepsilon_i^r N_i \quad (\text{e 2.xx})$$

with the coefficients γ_r describing the confocal volume and ε_i and N_i the brightness per particle and the number of particles of the species i of s .

The model has to adapt the number of cumulants to the number of expected variables, ε_i and N_i per species, to solve the equations. As a drawback, the number of expected species affects the analysis and is always fulfilled afterwards. γ_r is usually approximated from the theoretical assumption of a three dimensional Gaussian confocal volume and therefore is subjected to systematic error.

Because the cumulants are independent from the frame rate, same as the variance in N&B, an advantage of FCA is the ability to cumulate data from various, separated measurements of the same sample type. To combine data from different confocal volumes, the contributions from the microscopy system have to be separated from the observed values ε_i and N_i (*chapter 7.3*).

2.4. Requirements for FCS measurements in cells

Although FCS was already implemented in 1972 [Madge 1972], poor signal-to-noise ratio impaired its application inside cells. To increase the signal, the intensity fluctuations have to increase in relation to the detector noise and the average light intensity. The average intensity can be reduced by decreasing the number of fluorophores, e.g. by decreasing the detection volume. Therefore FCS was strongly improved by the implementation of confocal detection, decreasing detection volume (factor $\sim 10^4$) [Rigler 1993]. To increase the fluctuations created by a single fluorophore, the brightness of single fluorophores has to increase. This can be achieved by exciting efficient fluorescent dyes (brightness of single particle) with stable lasers at specific wavelengths. Ultrasensitive and fast detectors, e.g. avalanche photodiodes, reduce noise (e.g. APDs with ~ 200 dark counts/ s) and improve temporal resolution. A protocol for assembling an FCS system for living cell measurements can be found in [Kim 2007].

2.4. Fluorescence Correlation Spectroscopy (FCS)

Living samples are never in steady states. The measurement duration has to be small compared to the processes observed. Apart from that, cells have only a small volume. Considering the small concentration of fluorophores required for FCS, the total number of fluorophores is small and photochemical reactions can change the visible ratio. The photochemical destruction of the fluorescent property of fluorophores is called bleaching. It can influence the accuracy of single fits or complicate the interpretation of measured sequences. In pauses between intervals and in case of diffusion, the local ratio of bleached and visible fluorophores can recover up to an equilibrium with the environments ratio.

To reduce the influence of bleaching on fits, the interval time has to be chosen short enough, typically 10 s. During this period, enough intensity fluctuations have to be measured. For shorter collection times, the number of intensity count data to correlate with data after a time delay τ up to 1 s will not be sufficient. The bleaching is proportional to the excitation light. Therefore each measurement is a compromise between photon counts and signal to noise ratio against bleaching. Any additional light source has to be avoided because it increases the background and the bleaching.

In case of parallel FCS inside a single cell, the bleaching is a particular problem, for the photon counts depend on the excitation of each single confocal volume, while the bleaching is proportional to the total light intensity summed up from all confocal illuminations. For this reason, the number of observed and illuminated confocal volumes has to be minimized while fulfilling the purpose of the measurement. E.g. a process of accumulation of fluorophores in the nucleus, it could be sufficient to measure one volume inside the nucleus and one volume in the cytosol. If a gradient is to be observed, a line of 3 or more volumes would be efficient. Still, more observed volumes can increase the statistics. In this work, up to six volumes proved to be a suitable compromise.

For calculating absolute values from autocorrelation curves, the size of the volumes have to be calibrated. Although the theoretical detection volume of a confocal microscope with known pinhole and optical system could be calculated, it is more feasible to correct for aberrations and alignment by determining its volume by measurements. This can be performed with a known dilution of fluorophores, either using a known concentration or a known diffusion rate. Knowing the size of the volume, the time needed by the fluorophores to diffuse through the volume yields the absolute diffusion rate and the number of fluorophores to their absolute concentration respectively.

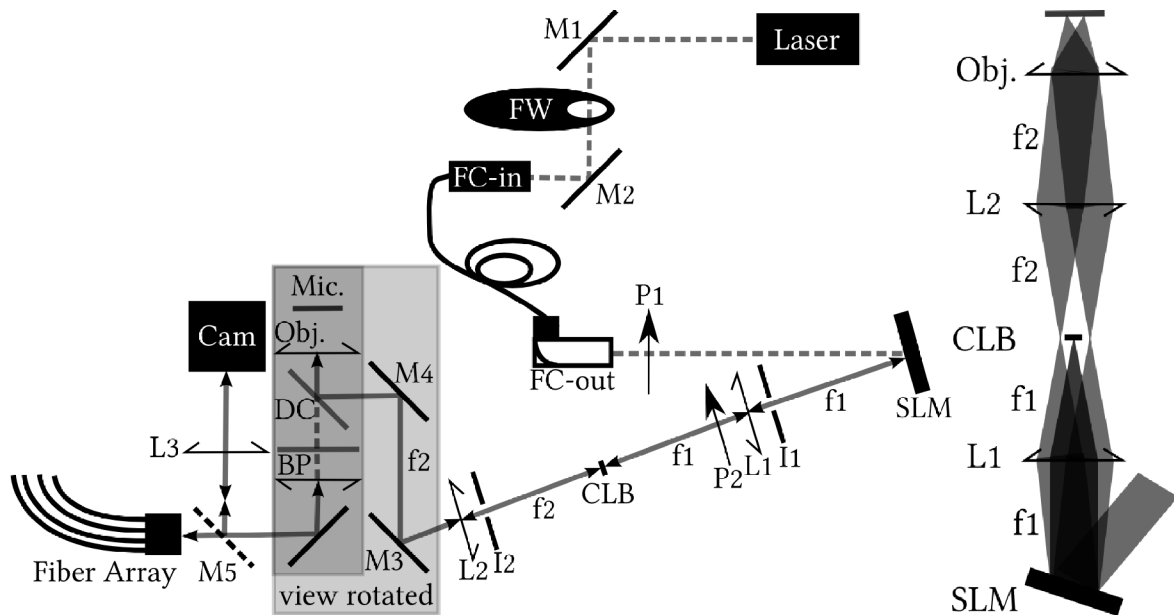
3. Optical System

The optical system is comprised of three main parts. In the first part the multiple excitation beams are created and aligned (*chapter 3.1.1*). The second component focus the beams into the sample and collects the fluorescence (*chapter 3.1.2*). The third part is the multiple point detection (*chapter 3.1.3*). This chapter is split into the design of the fixed optical components, e.g. fixed lenses, mirrors, the microscope and the detectors, (*chapter 3.1*) and the adaptive optical component. The description of the adaptive optic starts with an introduction to the basic idea of the implementation of a phase modulating Liquid Crystal on Silicon devices (LCoS) to distribute the illumination in a microscope system (*chapter 3.2*). Two LCoS devices were compared (*chapter 3.3*). Next, the calculations of the implemented LCoS controlling phase patterns are explained (*chapter 3.4*). These patterns are used for an automated calibration of the illumination, described in *chapter 3.5*. For further optimization and correction a Direct search and simulated annealing algorithm (*chapter 3.5.3*) is implemented.

3.1. Optical System

3.1. Design of the fixed optical system

The system was designed for robustness and the possibility of changing the wavelength while having the required performance for multifocal FCS measurements (*f 3.i*).



f 3.i: Fixed optical system of the SRFCs system.

<i>M1 and M2</i>	<i>mirrors for coupling into fiber.</i>
<i>FW</i>	<i>filter wheel with a selection of neutral density filters and a light blocker.</i>
<i>FC-in</i>	<i>fiber coupler input.</i>
<i>FC-out</i>	<i>achromatic fiber coupler output.</i>
<i>P1 and P2</i>	<i>polarizer.</i>
<i>SLM</i>	<i>spatial light modulator, a LCoS.</i>
<i>I1 and I2</i>	<i>irises for manual alignment.</i>
<i>L1 and L2</i>	<i>lenses – telescope with focal lengths f_1 and f_2.</i>
<i>CLB</i>	<i>center light blocker.</i>
<i>M3 and M4</i>	<i>mirrors for coupling into microscope.</i>
<i>DC</i>	<i>dichroic mirror.</i>
<i>Obj.</i>	<i>Objective.</i>
<i>BP</i>	<i>band pass filter.</i>
<i>M5</i>	<i>switchable mirror in dual-port C-mount adapter.</i>
<i>L3</i>	<i>focus lens for camera.</i>

An Argon (Coherent Innova 305C) and a Krypton (Coherent Innova 302C) gas laser, operating in single wavelength mode, are used as light sources. A motorized filter wheel (Thorlabs FW102) is used to switch between multiple neutral density filters to attenuate the laser intensities or to block the beam.

To obtain efficient spatial light modulation, the laser beam arriving at the LCoS has to be linearly polarized and reflected in a small angle. For a high effective resolution it should have a diameter close to the length of the short side of the rectangular LCoS (8.64 mm for the Holoeye Heo 1080P, 12 mm for the Hamamatsu X10468-01). At least one telescope is needed, to have a focused point between and a fixed image plane at the back focal plane of the objective while tilting the beam. It is chosen to create a beam diameter close to the back focal plane of the objective. The focus is needed for a beam blocker as described below. The fixed image plane will be point of rotation used for the adaptive optical system described in the next chapter. A high beam diameter and a collimated TEM 00 mode beam at the focusing lens are desired to achieve the optimal focusing and the smallest illuminated confocal volume. The beam enters the objective and images the Fourier transform of the complex amplitude in the LCoS into the sample plane (*chapter 3.2*).

3.1.1. Illumination

A single mode fiber fitting the wavelength range of interest (450 – 600 nm; $NA_{\text{fiber}} 0.13$) and a reflective, achromatic collimator ($f_{\text{coll}} = 33$ mm; $2 \cdot NA_{\text{fiber}} \cdot f_{\text{coll}} = 8.58$ mm beam diameter; RC08FC-P01, Thorlabs) are used to produce a homogeneous and wide beam for the LCoS. Because of the achromatic collimator, several laser beams with varying wavelength in the visible range will be collinear, as soon as they are coupled into the fiber. Only the phase patterns of the LCoS have to be adjusted for different wavelengths. A polarizer before and after the LCoS exclude light not fitting the required polarization for the LCoS.

Behind the LCoS, a system with either one or two telescopes was considered. Because of the geometry of the microscope, the last lens needs to have a focal length of at least 200 mm to produce the image plane at the back focal plane of the objective. A focal length of 300 mm allows two alignment mirrors, forming a periscope at the side port of the microscope. To find the best lens combination from a number of lenses with defined steps of focal lengths, the beam path was optimized using ABCD-Matrix calculations [Kogelnik 1966], the optical

3.1.1. Optical System

requirements and a brute force script written in Mathematica 6.0 (Wolfram Research). It was found, that the system with two telescopes produced a beam waist that fits the back focal plane better, but the single telescope produced a suitable beam waist while being more robust and easier to maintain. For a single telescope, it yields 500 mm and 400 mm, producing a beam width at the back focal plane of 0.68 mm.

Between the lenses, at the focus, the centered light is blocked by a round spot of ink on a glass slide. The centered light includes the light not affected by the LCoS and most of the stray light created by imperfect phase modulation. The lenses, the light-blocker and two irises for alignment are mounted on a rail.

There are other possibilities to eliminate the light not affected by the LCoS, e.g. using an additional deflection prism and block the non affected light outside of the beam path or using a lens pattern to block the center spot even more efficient [Polin 2005]. Using the grating effect of pattern, it is also possible to use the 1st order diffracted light for the beam path [Maurer 2010], however this would require additional alignment for wavelength changes. All these solutions would also need additional patterns which could, due to the imperfect digitization, affect the beam and the confocal volume.

3.1.2. Microscope

The system is mounted to an Olympus IX 81 microscope. A periscope is used to align the beam path into the side port of the microscope filter wheel (IX-FRFACA, Olympus), equipped with a side port filter cube (IX2-MFB-SP-R, Olympus). Additionally to a Fluorescence illumination system (MT20, Olympus) connected to the back port of the microscope, using a lens phase pattern on the LCoS, the side port can be used for a laser based wide field illumination without the need of changing the filter cube.

3.1.3. Detection

In the left camera port of the microscope, a dual-port C-mount adapter (U-DPCAD, Olympus) is used to switch between confocal and wide field detection. A 4×4 fiber array (core diameter 105 μm, NA = 0.22, fiber pitch 250±2 μm; Fiberguide Industries) is connected via a matched solid spacer. The aperture of the fibers are used as pinholes to create a confocal detection volume. For wide field detection, an EM-CCD (Hamamatsu C9100-13) is mounted. In front of the camera, a 25.4 mm lens shifts the image plane through a lens tube while enlarging the image 3x. An optional 50:50 beam splitter can be mounted inside the dual-port C-mount adapter for calibrations.

Depending of the chosen objective, the attached fiber array can span over an area of approx. 7.6×7.6 μm² (100x Oil 1.4 UplanSApo, Olympus) to approx. 37×37 μm² (20x Air 0.7 UplanSApo, Olympus). The mostly used 40x oil (1.3 UplanFLN, Olympus) and 60x oil (1.35 UplanSApo, Olympus) objectives spans over an area of approx. 19×19 μm² and 12.25×12.25 μm² respectively. The fibers are connected with four single photon counting module arrays (SPCM-AQ4C, Perkin Elmer), each with four avalanche photodiodes (APDs). The resulting event pulses are counted and correlated by a 16-channel photon correlator card (DPC-230, Becker & Hickl GmbH). For measurements in diluted fluorophores and in cells with 4 to 6 parallel confocal volumes, the laser power before the SLM was in the range between 2 mW and 6.3 mW. For one positioned illumination volume, about 50% of the light reaches the substrate behind the objective. The losses rise with the number of separated illumination volumes.

It needs to be considered, that the fiber array is fixed in the imaging plane and cannot be moved in z. Therefore an iterative alignment of an objectives correction ring and the z position of the 'pinholes' is not possible. However, any alignment would suffer from the need of precise adapted light deflections created by the SLM. For any change of the correction ring or the z position, a new alignment of the illumination light, further called calibration, is needed. The optimal setting of the correction ring cannot found by using the photon counts through the fibers, but iteratively by focusing with the camera, changing the correction ring and refocusing, until the sharpest image is achieved.

3.2. Design of the adaptive optical system

To achieve a multifocal system, the beam has to be split into multiple beam paths. This system will use a LCoS to split and align the light. One possibility is to create multiple lenses on the phase modulating LCoS. The lenses are easily aligned to the detectors. This method is used in SPAD-array based systems [Colyer 2010] [Colyer 2011], but was neglected because of the small beam diameter of each beam after the SLM. A wider beam should result in a sharper focus and therefore a smaller confocal volume [Hess 2002]. Moreover, multiple small lens pattern could suffer from the digitization limits of the SLM. Another possibility is the use of a phase-contrast filter (PCF) [Eriksen 2002]. In the focus of a telescope between a phase modulating SLM and the microscope, a small pinhole acts as a phase-contrast filter. Two irises, in the collimated beam lines before and after the telescope, are matched to the pinhole to increase the contrast of the intensity distribution. The advantage is an even more simplified, binary phase pattern results in focused spots behind the objective. As a drawback, the optimal diameter of the pinhole is wavelength specific. Furthermore, the system is quite sensitive to misalignment resulting in low contrast and high background illumination.

To use the full width of the beam and to enable the adaptive optics to overcome small misalignments, an iterative method using the objective for Fourier transformation and focus is the best solution. Many theoretical methods used for optical traps fulfill these conditions. The fastest and easiest method is the superposition of prisms and lenses. Although this method causes ghost traps (unwanted focused spots caused by symmetries) and a non uniformity of the intensity in the different spots, its linearity drastically simplifies the calibration of the spot positions. Ghost traps will cause unwanted bleaching, but in case of single cells, the additional spots are mainly outside of the observed cell. The intensity variation between spots will be determined by the same FCS calibration measurement done to determine the size of the confocal volumes. The variations and sizes can differ for each combination of activated confocal volumes. The software implementation of the calibration allows future developments to other linear holographic algorithms, e.g. the random mask encoding [Leonardo 2007].

To calculate a holographic phase pattern that produces a specific light distribution, the incoming beam, represented as complex amplitude u of the electric field with the real valued amplitude profile a and the phase front φ_{inc} , has to be known and integrated over the front:

$$u = a \exp(i \varphi_{inc}) \quad (\text{e 3.i})$$

The phase SLM introduces a phase shift φ_{SLM} . The phase shift is bound to be constant over the range of each single pixel:

$$u_{SLM} = a \exp(i(\varphi_{inc} + \varphi_{SLM})) \quad (\text{e 3.ii})$$

In addition the imperfect optics behind of the induced phase modifications φ_{opt} should be considered. The uneven number of lenses result in a Fourier transformed complex field u_{opt} in the image plane:

$$u_{opt} = F \left\{ a \exp(i(\varphi_{inc} + \varphi_{SLM} + \varphi_{opt})) \right\} \quad (\text{e 3.iii})$$

Although, assuming a uniform light distribution as input and perfectly formed and positioned lenses, most parts of the beam propagation can be simplified, the system can be even more simplified and improved by calibrating it in an actual measurement with a homogeneous fluorescent sample.

3.3. Optical System

3.3. SLM Devices

Two different phase modulating LCoS were tested. While the first device (Heo 1080P, Holoeye Photonics AG) featured a high pixel resolution, only the second device (X10468-01, Hamamatsu) showed the stability required for FCS.

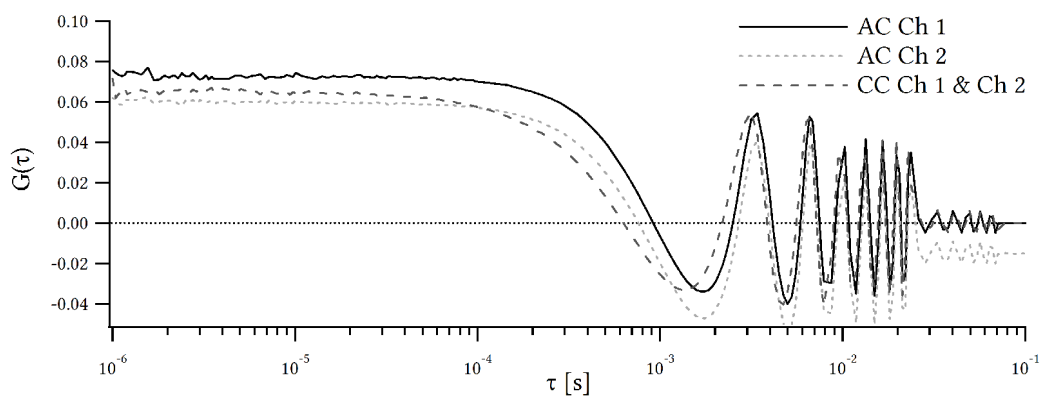
3.3.1. Holoeye Heo 1080P

The Heo 1080P from Holoeye Photonics AG has a full HD resolution of 1920×1080 and up to 256 phase step levels and nematic aligned crystals. The high resolution reduces the effect of the digitalization of the optical elements and the disruption of the phase front and therefore improve the confocal volume. The active area is $15.36 \times 8.64 \text{ mm}^2$. Provided the width of the beam reflected by the LCoS (8.58 mm), the number of effectively used pixels is reduced to a circle with a diameter of 1072.5 pixels.

For the device, no correction pattern for the uneven reflecting back of the LCoS was given. But there are many known ways to achieve those, even without a phase wavefront detector. Any defined and known theoretical illumination pattern can be compared with the actual result, e.g. a grid of lens pattern with the relative spot position distribution. Another way is the use of a direct search and simulated annealing algorithm which improves the pattern till all errors were corrected.

To create a linear phase shift per level, a series of calibration measurements and calculations for each used laser wavelength on a calibration setup had to be done and loaded to the device. This is done using two pinholes, illuminating two different phase steps on the LCoS with one laser, changing the phase difference and measuring the shift of the interference pattern behind a lens. Although, the calibration could probably be adapted to be performed without changing the optical system, it would be slow in switching between multiple wavelengths and impossible to use with multiple wavelengths parallel on different parts of the LCoS. Depending of the calibration, the whole range of phase steps produced a total phase shift from 2 to 2.5π . The controller of the device is connected and addressed as a second monitor by a controlling computer. For addressing the high number of pixels, a digital addressing for communication between the controller and the LCoS is used. Different addressing sequences, resulting in

different refresh rates and different amount of phase step levels (≤ 256 , homogeneous distributed), were tested. In pulse-width modulation (PWM), the alignment of the crystals is modulated by the length of a constant voltage signal [Lizana 2009]. After the alignment the crystals can move freely. A pattern using different phase levels and therefore different alignment durations, creates a band of time dependent phase modulations. These modulation result in a time dependent illumination in the same range as the estimated fluorescence fluctuations due to diffusion of fluorophores measured in FCS. To distinguish these fluctuations from fluorophore diffusion, a non diffusing fluorescence plate can be used or the cross-correlation between two separated fibers calculated (*f 3.ii*).



f 3.ii: Autocorrelation curves of three channels and cross-correlation between two of them while measuring a fluorescent plate (no diffusion) with a Holoeye Heo 1080P in the illumination path. The curves vary because the confocal volumes have varying volumes. The oscillations fit the refresh rate of the LCoS ($1/\tau = 300$ Hz) and its higher harmonics.

The fluctuations induced by the LCoS were independent of the control computer or any graphical settings of the computer. To reduce the fluctuations, different addressing sequences were tested without major improvement. Cooling the device down to 8 °C with a peltier element and using pattern with two phases reduced the fluctuations, but only a uniform phase pattern showed sufficient fluctuation suppression. Cooling further down to lower degree will hinder the alignment of the fluid crystals of the LCoS.

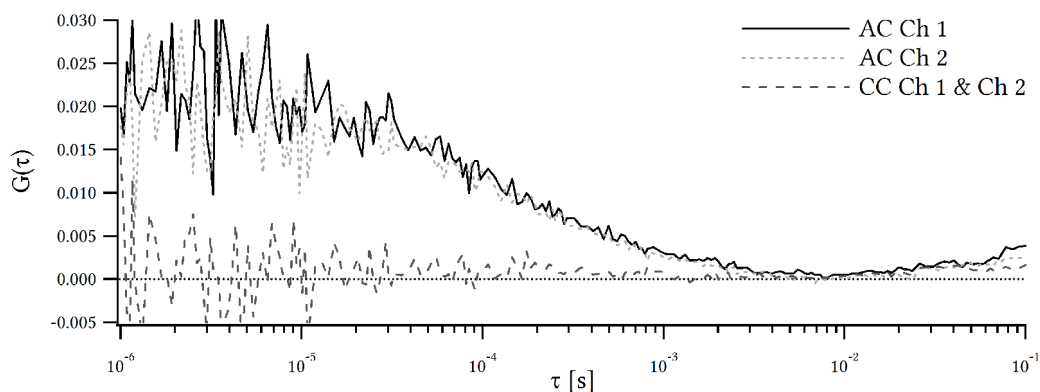
3.3.2. Optical System

3.3.2. Hamamatsu X10468-01

The second LCoS was chosen to use analog addressing and parallel aligned crystals (PAL) [Jepsen 2005]. With analog addressing, all crystals are aligned for the same amount of time and the alignment is modulated by the height of the voltage signal. The X10468-01 is optimized for a range of wavelength from 400 nm to 700 nm. It has a resolution of 792×600 pixels (addressed with 800×600 pixels) and up to 256 phase step levels depending of the wavelength of the affected light. E.g. for our device and 488 nm, 139 phase step levels are given to produce a total phase shift of 2π (1 to 139, while 140 to 256 are not used). The width of the beam reflected by the LCoS (8.58 mm) reduces the number of effectively used pixels to a circle with a diameter of 429 pixels.

To change a pattern between different wavelengths, only another number of phase steps resulting in a 2π phase shift has to be modified in the last step of pattern calculation or the phase step size be corrected.

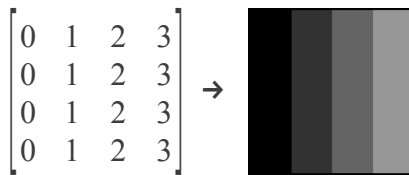
Different parts of the LCoS phase pattern are allowed to use different amounts of phase steps without affecting each other. Therefore, probably different wavelengths using different parts of the LCoS can be modulated separately. Most importantly, in the range of interest no visible FCS on a fluorescence plate and no cross-correlation between different fibers was detected. *f 3.iii* shows two autocorrelation curves of neighboring fibers measured in Alexa488 in dilution in water with about as much as 50 particles per volume.



f 3.iii: Autocorrelation curves of two channels and cross-correlation between them while measuring Alexa488 in dilution in water with a Hamamatsu X10468-01 in the illumination path.

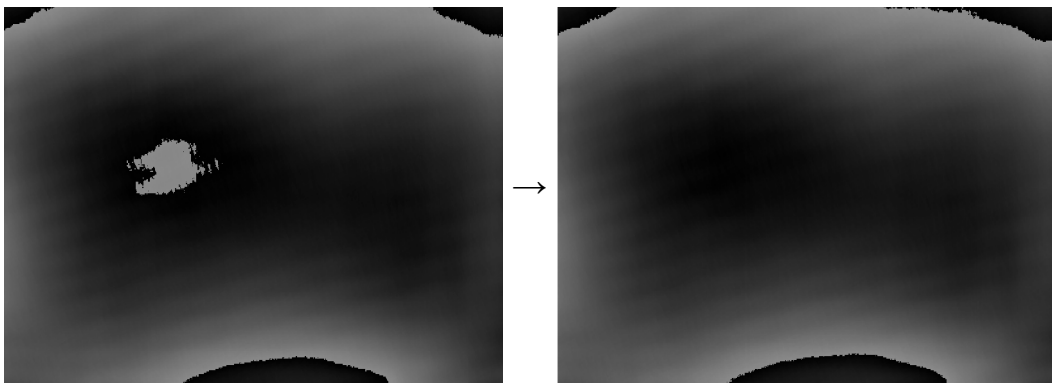
3.4. SLM control pattern creation

The pixels of the SLM are arranged in an array and addressed as a matrix of values controlling the alignment of the fluid crystals. The matrices are represented and transferred to the LCoS as 8-bit grey level images (*f 3.iv*).



f 3.iv: Matrix represented as 8-bit grey level image.

The reflecting surface of the LCoS is uneven and can disturb the phase front of the beam. These irregularities can be corrected by the LCoS itself with a correction pattern. These wavelength dependent patterns were provided by Hamamatsu and improved to move any Fresnel lens like phase jumps to the sides of the pattern and out of the beam path (*f 3.v*).



f 3.v: Background correction and improved background correction for our specific LCoS for 488 nm.

The background correction B is added (*e 3.xi*) to any used pattern before merging (*e 3.v*).

3.4. Optical System

Starting with a perfect mirror, patterns were created to mimic the phase front distortion introduced by optical elements. These patterns were calculated as matrix M_{nm} , with each value correlating to a grey color, and n times m elements fitting the resolution of the SLM. To improve the speed of the implemented software, all pattern start with two matrices X_{nm} and Y_{nm} :

$$\begin{bmatrix} 0 & 1 & 2 & \cdots & n-1 \\ 0 & 1 & 2 & \cdots & n-1 \\ \vdots & \vdots & \vdots & \ddots & \vdots \\ 0 & 1 & 2 & \cdots & n-1 \end{bmatrix}_{nm} - \frac{n}{2} = X_{nm} \quad \begin{bmatrix} 0 & 0 & \cdots & 0 \\ 1 & 1 & \cdots & 1 \\ \vdots & \vdots & \ddots & \vdots \\ m-1 & m-1 & \cdots & m-1 \end{bmatrix}_{nm} - \frac{m}{2} = Y_{nm} \quad (\text{e 3.iv})$$

The subtrahend $n/2$ and $m/2$ can be changed to move the center of the pattern. Otherwise, it is centered on the SLM.

The quantity of phase steps is limited by the LCoS. Both LCoS used in this work have a scale resolution of 8 bit. While 8 bit gray colors allow 256 colors (counted 0-255), a pattern can be calculated with a smaller (darker) maximum gray color (c_{max}) or with less number of total elements (c_{total}) with ($c_{total} \leq c_{max} + 1$). For the Hamamatsu LCoS the specific values for c_{max} , and therefore the maximal c_{total} , for phase shifts up to 2π depend on the wavelength. To define a matrix inside these phase resolution boundaries, the matrix M_{nm} is merged to M_{merged} before the pattern is send to the LCoS controller:

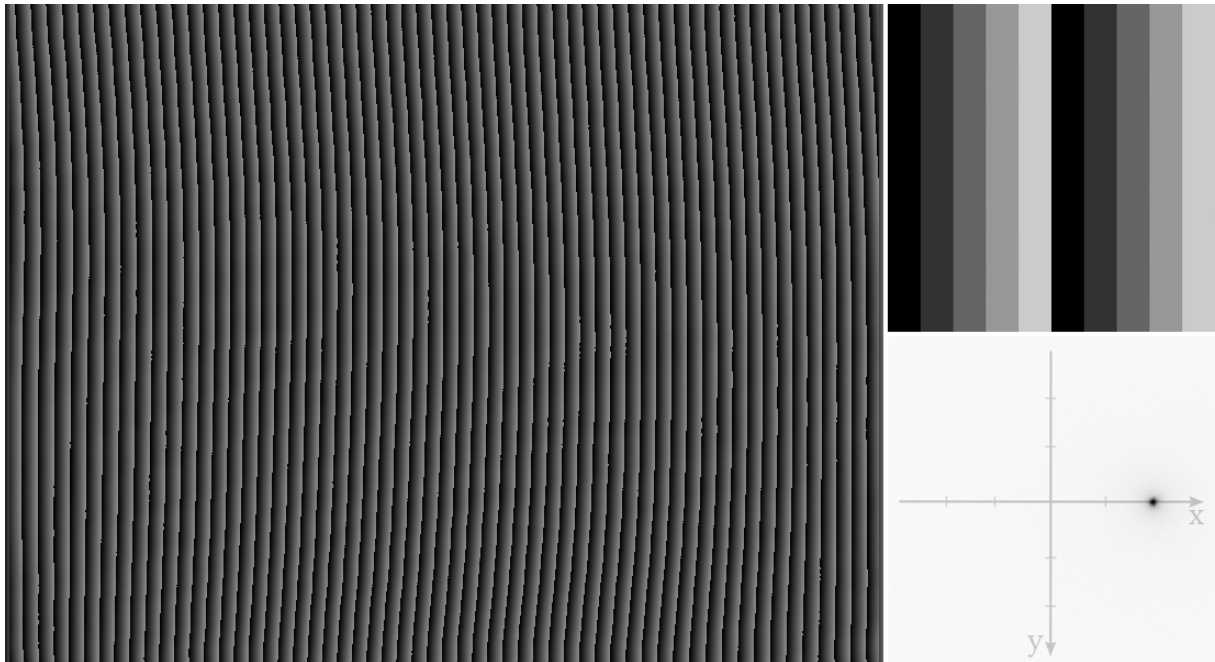
$$M_{merged} = \left[M_{nm} - c_{total} \cdot \left[\frac{M_{nm}}{c_{total}} \right]_{floor} \right] \cdot \frac{c_{max}}{c_{total}} \quad (\text{e 3.v})$$

3.4.1. Prism and superposition

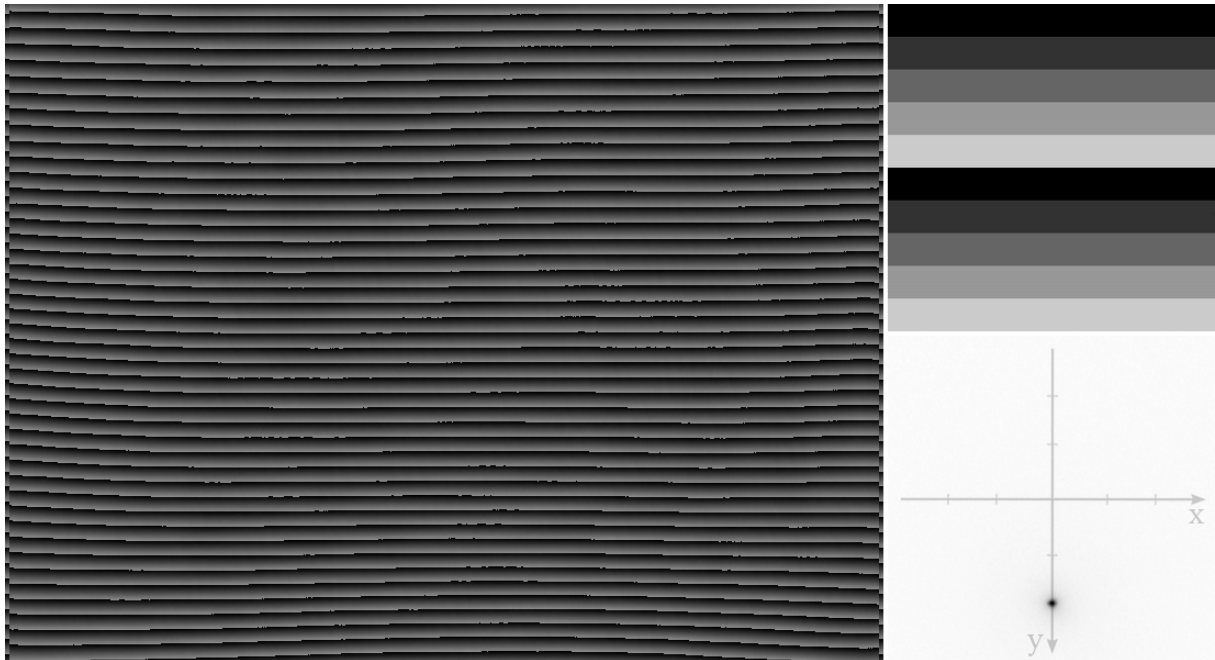
A prism can be emulated by a gradient of gray levels. The slope depends on the on the axes parameters x and y as in the linear equation:

$$X_{nm} \cdot x + Y_{nm} \cdot y = MP_{nm} \quad (\text{e 3.vi})$$

As the resulting deflection of the illumination is linearly dependent on x and y , these parameters create a coordinate plane with the non deflected light at $(x; y) = (0; 0)$ as point of origin (*f 3.vi*) (*f 3.vii*) (*f 3.viii*).

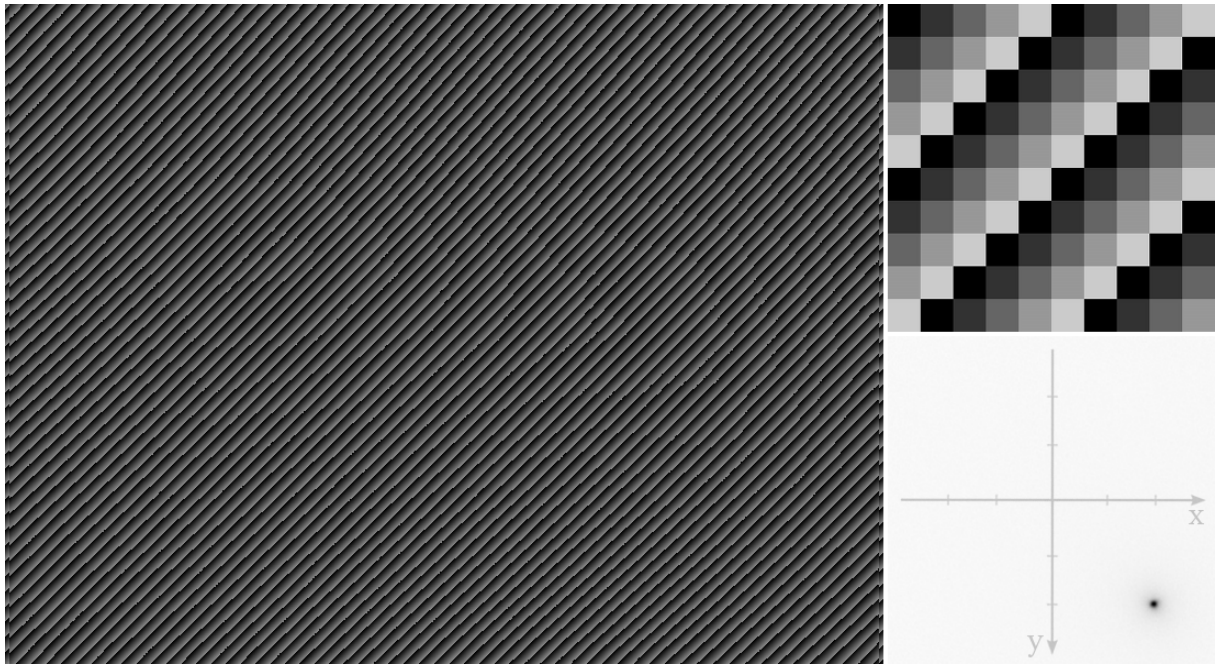


f 3.vi: Prism pattern to create an illumination spot behind a lens. Left side actual used pattern incl. background correction, 800×600 pixels, $c_{max} = c_{total} = 139$, $(x; y) = (10; 0)$. Upper right: 10×10 pixels, $c_{max} = 255$, $c_{total} = 10$, $(x; y) = (2; 0)$. Lower right: resulting illumination of pattern shown left.



f 3.vii: Prism pattern to create an illumination spot behind a lens. Left side actual used pattern incl. background correction, 800×600 pixels, $c_{max} = c_{total} = 139$, $(x; y) = (0; 10)$. Upper right: 10×10 pixels, $c_{max} = 255$, $c_{total} = 10$, $(x; y) = (0; 2)$. Lower right: resulting illumination of pattern shown left.

3.4.1. Optical System

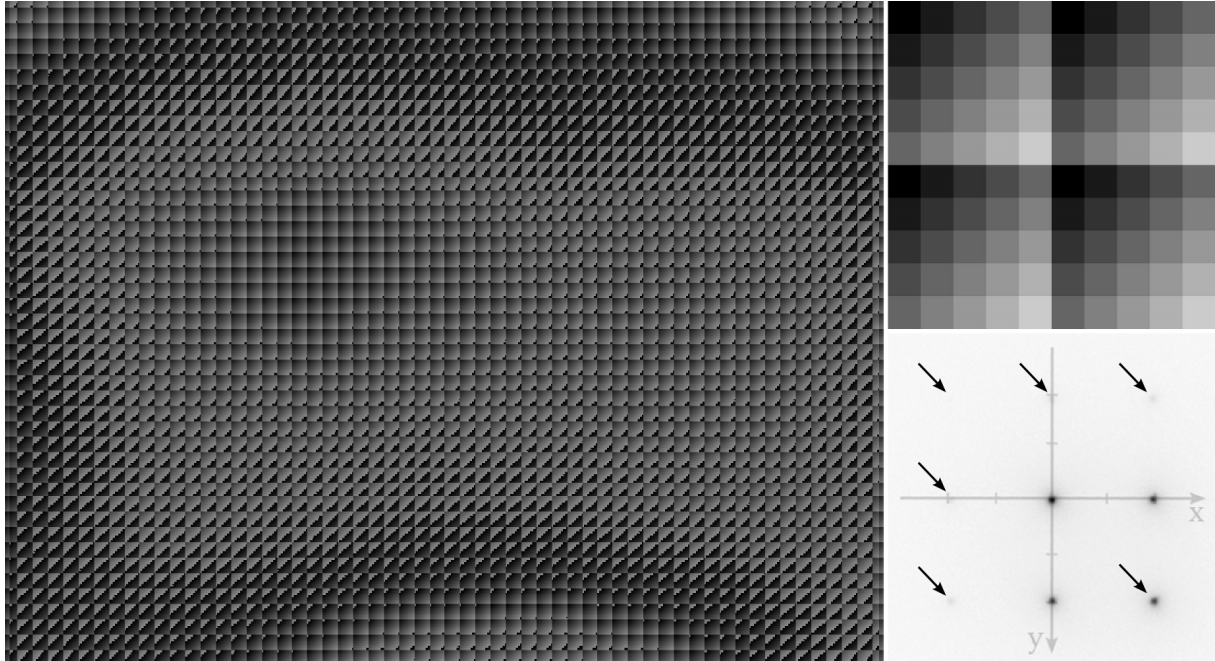


f 3.viii: Prism pattern to create an illumination spot behind a lens, merged sum of the pattern of f 3.vi and f 3.vii. Left side actual used pattern incl. background correction, 800×600 pixels, $c_{max} = c_{total} = 139$, $(x; y) = (10; 10)$. Upper right: 10×10 pixels, $c_{max} = 255$, $c_{total} = 10$, $(x; y) = (2; 2)$. Lower right: resulting illumination of pattern shown left.

Because of the linearity of the calculations, any patterns summed before merging act as a single pattern creating a single effect. If multiple patterns should create separated effects, the simplest way is to divide the sum of patterns by their number k before merging:

$$M_{add} = \frac{M_1 + M_2 + \dots + M_k}{k} \quad (\text{e 3.vii})$$

Still, these added patterns also create additional combined effects, resulting in so called ghost traps (*f 3.ix*). The intensity and the distribution of the ghost traps changes with the number of combined patterns. Diffusive light accumulate at the center position as the number of patterns rise.



f 3.ix: Prism pattern to create two illumination spots and multiple ghost traps behind a lens. Left side actual used pattern incl. background correction, 800×600 pixels, $c_{max} = c_{total} = 139$, $(x_1; y_1) = (10; 0)$, $(x_2; y_2) = (0; 10)$. Upper right: 10×10 pixels, $c_{max} = 255$, $c_{total} = 10$, $(x_1; y_1) = (2; 0)$, $(x_2; y_2) = (0; 2)$. Lower right: resulting illumination of pattern shown left, showing ghost traps at pointed positions (brightest 120%, second order < 15%, third order < 5% of intensity per aimed spot) and diffusive light focused at (0; 0) (150% of intensity per aimed spot).

The values have to be converted to integers and therefore the center of the patterns can shift by one pixel due to rounding. In case of patterns symmetric to their center, this shift can affect the illumination distribution. However, since the maximal shift is only one pixel and this is much smaller than the error introduced by a non perfectly centered beam in the LCoS, the effect can be neglected in most cases. Non center symmetric pattern, like prism pattern, are not affected at all.

Additionally, when adding multiple patterns, each pattern after the first can be shifted slightly ($X_{nm} \rightarrow X_{l,nm}$, with l = number of pattern; Y_{nm} accordingly) to enable light distributions totally symmetric to the center. This is only needed in perfectly symmetric cases with $(x_1; y_1) = -(x_2; y_2)$, because the phase gradients of the added pattern vanish otherwise, and only enabled for seldom cases in the software implementation:

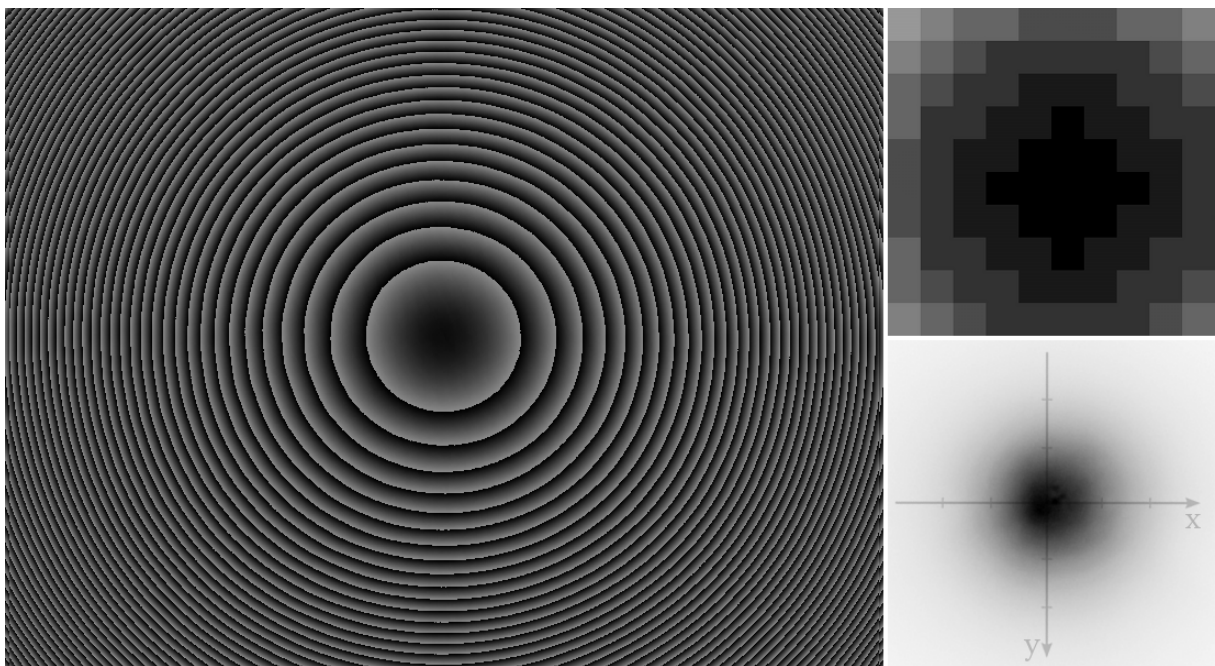
$$X_{l,nm} = X_{nm} + (l-1) \cdot \frac{255}{k} \quad (\text{e 3.viii})$$

3.4.2. Optical System

3.4.2. Lenses

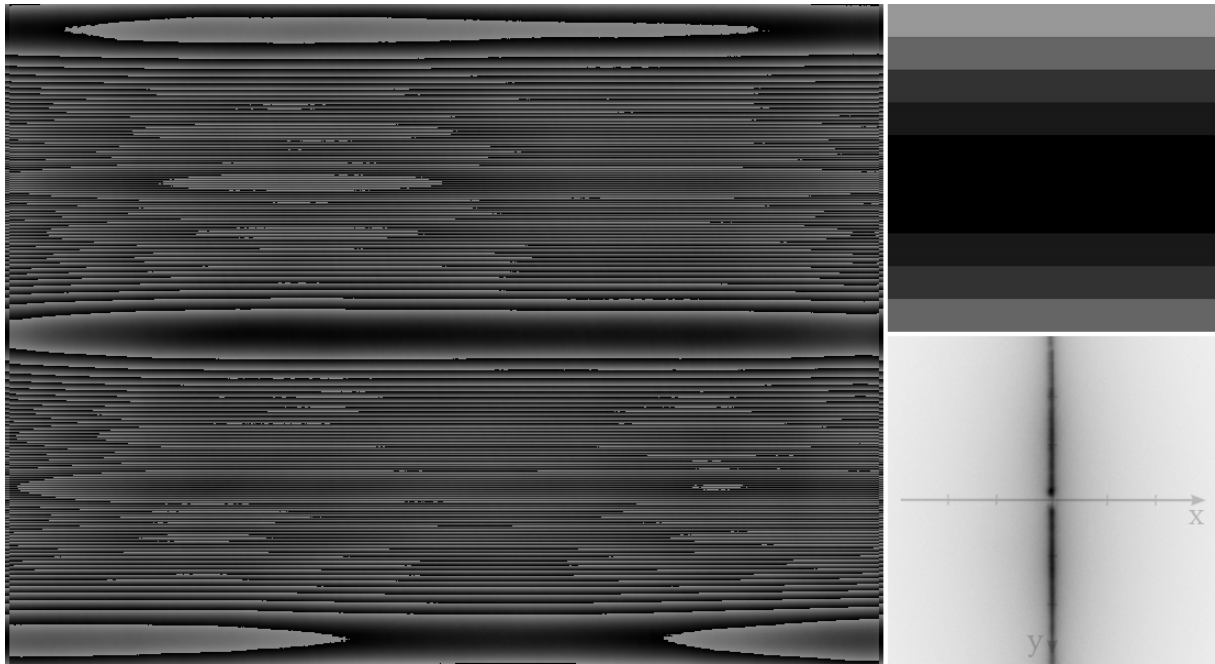
Using X_{nm} and Y_{nm} , it is also possible to create patterns that act as a lens with the focal length $f = f_x = f_y$. For the geometry of pixels of the Hamamatsu X10468-01 and $c_{max} = 139$ for 2π (488 nm), $f = 1$ happens to describe a focal length of about 25 cm (*f 3.x*).

$$\frac{X_{nm}^2}{4f_x} + \frac{Y_{nm}^2}{4f_y} = ML_{nm} \quad (\text{e 3.ix})$$



f 3.x: Lens pattern to create a magnified illumination spot behind a lens. Left side actual used pattern incl. background correction, 800×600 pixels, $c_{max} = c_{total} = 139$, $(x; y) = (0; 0)$, $f_x = f_y = 10$. Upper right: 10×10 pixels, $c_{max} = 255$, $c_{total} = 10$, $(x; y) = (0; 0)$, $f_x = f_y = 1$. Lower right: resulting illumination of pattern shown left.

In the limit $f_x \rightarrow \infty$ or $f_y \rightarrow \infty$, only one summand remains and the matrix creates a cylindrical lens, generating a line shaped illumination behind the objective lens (perpendicular to the cylindrical lens) (*f 3.xi*). For simplification, only lines parallel to the axes x and y were realized. In the software implementation for a line one of the summands is removed. The length of the line depends of the focal length of the remaining f .



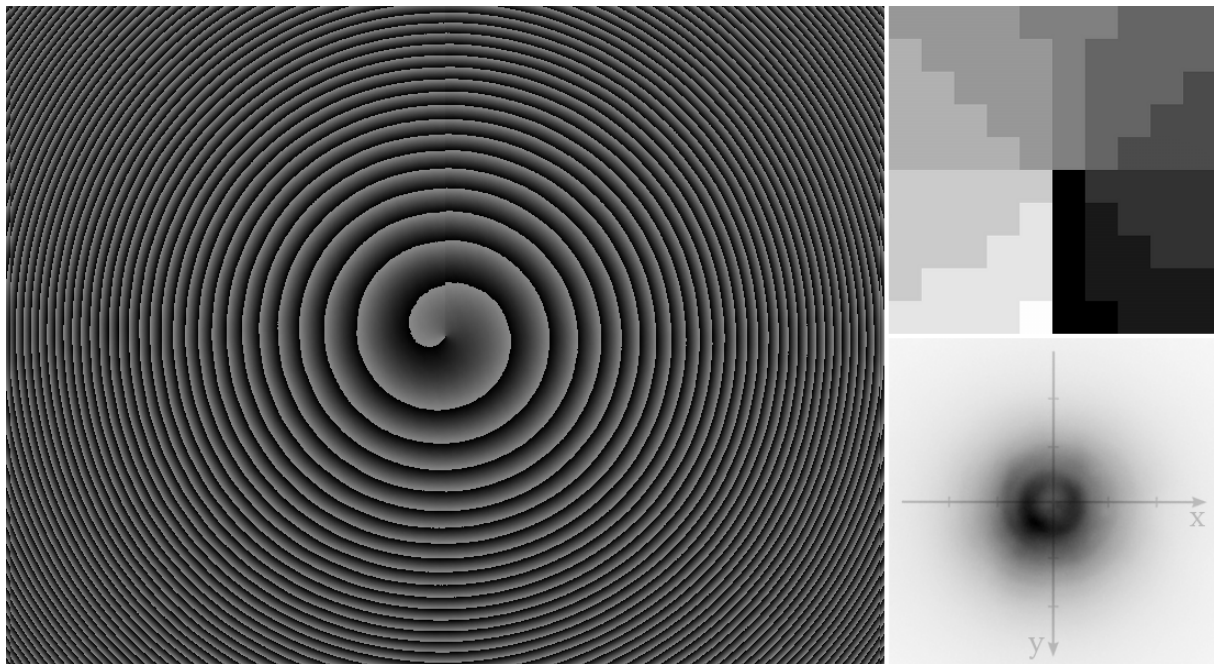
f 3.xi: Line pattern to create an illuminated line behind a lens. Left side actual used pattern incl. background correction, 800×600 pixels, $c_{max} = c_{total} = 139$, $(x; y) = (0; 0)$, $f_x = 10$, $\lim f_y \rightarrow \infty$. Upper right: 10×10 pixels, $c_{max} = 255$, $c_{total} = 10$, $(x; y) = (0; 0)$, $f_x = 1$, $\lim f_y \rightarrow \infty$. Lower right: resulting illumination of pattern shown left. Defect at $(0; 0)$ for lines at $(x; y) = (0; 0)$.

3.4.3. Donut

Donut shaped illumination is created by phase pattern producing a 1π phase shift between each pixel of the LCoS with point symmetry with respect to the center of the illuminating laser beam [Šlekys 1994] (*f 3.xii*). The phase shift results in an extinction of the light in the middle of the donut. Such a pattern can be created with the matrix MD_{nm} :

$$c_{total} \cdot \sin \left(L \cdot \arctan \left(\frac{X_{nm}}{Y_{nm}} \right) \right) = MD_{nm} \quad (\text{e 3.x})$$

3.4.3. Optical System



f 3.xii: Donut pattern to create an illumination donut behind a lens. Left side actual used pattern incl. background correction and lens pattern for magnification, 800×600 pixels, $c_{max} = c_{total} = 139$, $(x; y) = (0; 0)$, $f_x = f_y = 10$, $L = 1$. Upper right: 10×10 pixels, $c_{max} = 255$, $c_{total} = 10$, $(x; y) = (0; 0)$, $f_x = f_y = 0$, $L = 1$. Lower right: resulting illumination of pattern shown left.

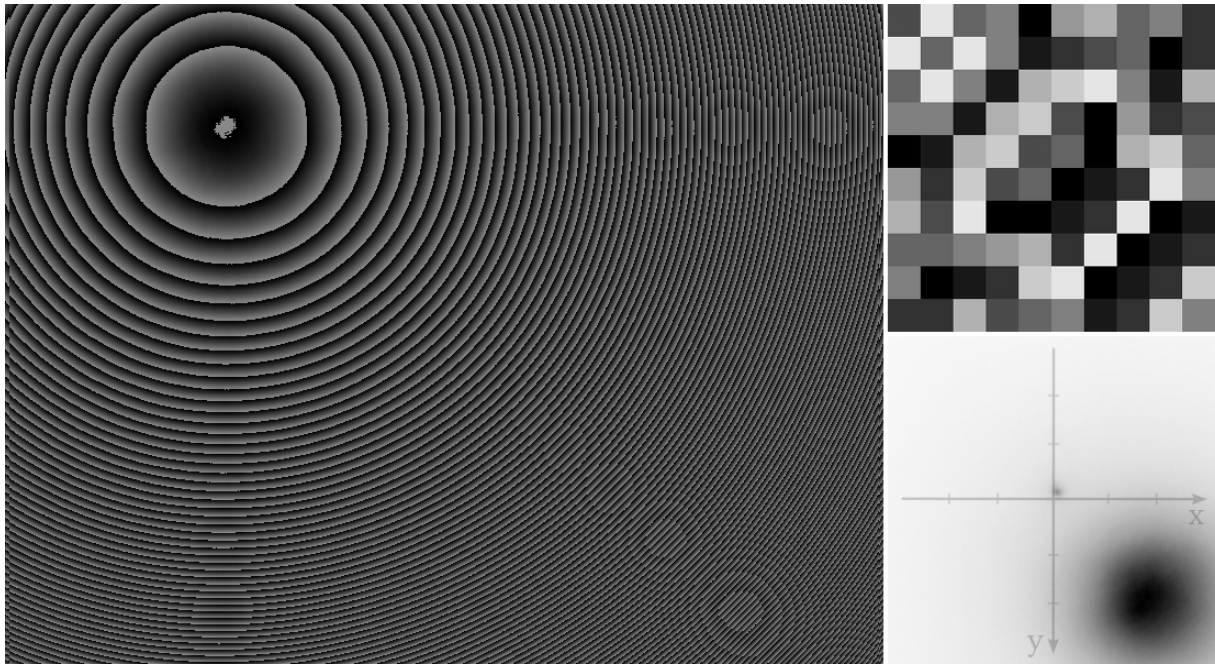
3.4.4. Combined patterns

To create an illumination spot depending on multiple parameters as x , y (shift), f_x , f_y (focus or line) or L (donut), the matrices have to be added to the background correction B to create MT_{nm} and merged (e 3.v) (example: f 3.xiii). In the software, all patterns are defined by these parameters:

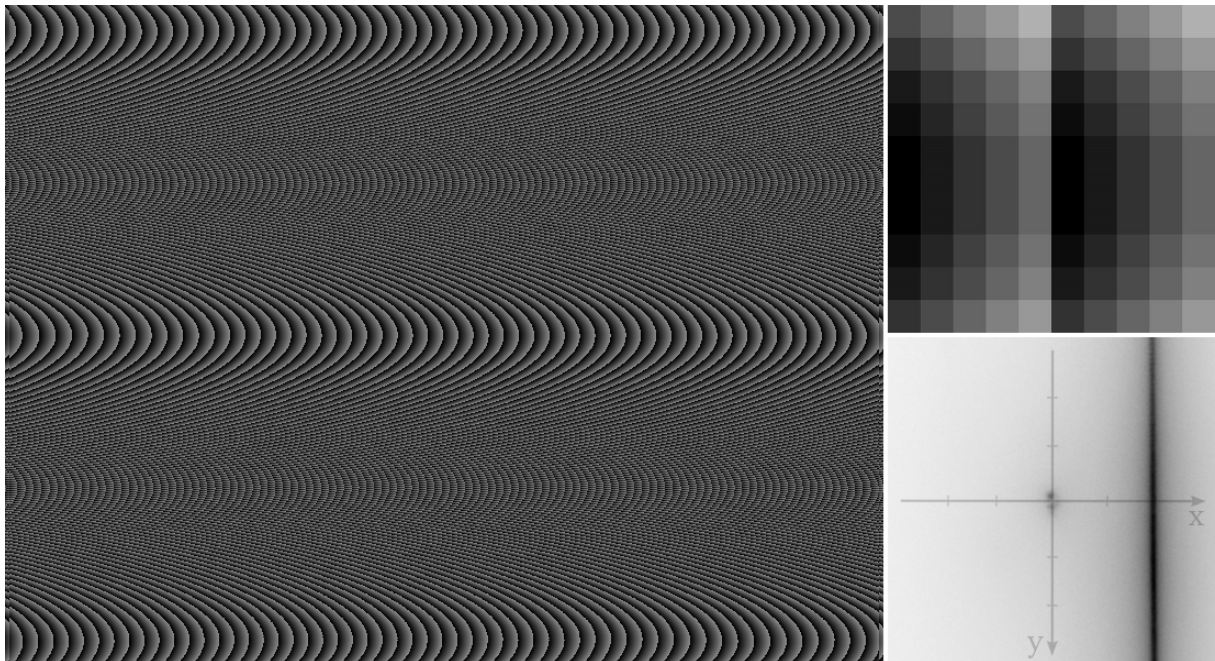
$$MT_{nm} = MP_{nm}(x; y) + ML_{nm}(f_x; f_y) + MD_{nm}(L) + B \quad (\text{e 3.xi})$$

To create multiple spots with varying parameters, for each spot the pattern is created and merged (e 3.v) separately, these pattern combined by (e 3.vii) and the resulting pattern merged again (e 3.v).

For the software implementation of the calibration of the system, the movement of a line (f 3.xiv) is of special interest, as will be discussed in chapter 3.5.2.



f 3.xiii: Lens with prism pattern to create a magnified illumination spot behind a lens. Left side actual used pattern incl. background correction, 800×600 pixels, $c_{max} = c_{total} = 139$, $(x; y) = (2; 2)$, $f_x = f_y = 10$. Upper right: 10×10 pixels, $c_{max} = 255$, $c_{total} = 10$, $(x; y) = (2; 2)$, $f_x = f_y = 1$. Lower right: resulting illumination of pattern shown left.



f 3.xiv: Line with prism pattern to create an illuminated line behind a lens. Left side actual used pattern incl. background correction, 800×600 pixels, $c_{max} = c_{total} = 139$, $(x; y) = (10; 0)$, $f_x = 10$, $\lim f_y \rightarrow \infty$. Upper right: 10×10 pixels, $c_{max} = 255$, $c_{total} = 10$, $(x; y) = (2; 0)$, $f_x = 1$, $\lim f_y \rightarrow \infty$. Lower right: resulting illumination of pattern shown left.

3.5. Optical System

3.5. Calibration of system

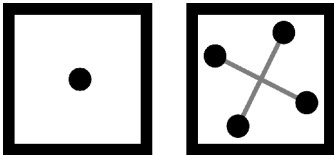
To control the distribution of the illumination, in particular position confocal volumes, the effect of the LCoS can be predicted due to model calculations. However, due to misalignments or aberrations in the optical system an in-situ calibration is desired. Two calibrations will be introduced. The first calibration is based on a camera sensor as coordinate system. The second calibration directly aims the positions of pinholes, e.g. fibers. Furthermore a direct search and simulated annealing algorithm for corrections and improvement of phase pattern is implemented.

3.5.1. Camera based calibration

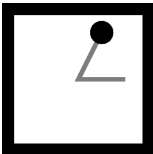
A phase pattern representing a prism is created and deflects a single focused spot from the center position. The spot position is determined by the mean of the center of the bright spot in a sequence of a few images and the deflection is quantified. Stepwise the slope of the prism is increased. As a result, the focused spot on the image plane will move further away from the center position (*f 3.xv*). Saving values representing the prism and the resulting deflection and interpolating between measured deflections, the spot can be positioned freely on a line, while correcting for positional errors of lenses and mirrors perpendicular to the beam path or the reflection angle of the LCoS. Using a pattern calculation based on a linear superposition and normalization of single prism patterns, only four series of prism pattern representing the axes directions x , y , $-x$ and $-y$ are required to achieve a free two dimensional positioning. For example, to position a spot at $(x_a; y_a)$ it is enough to know the patterns of positioning it at $(x_a; 0)$ and at $(0; y_a)$ (*f 3.xvii*). As described before, to create multiple spots, the pattern were simply added and the sum divided by the number of spots. This form of calibration can be used with a camera as detector and is used for the “Self calibrating, free positioning software” (*f 3.xvi*). The duration of calibration is about 30 min. An example is shown in *chapter 4.1.1*.

The complete process of the “Self calibrating, free positioning software” calibration can be broken into 7 steps:

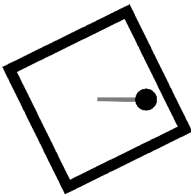
- 1. **determine center-position:**
 non deflected light
 or
 4 one-axis-deflections



- 2. **determine angle**
 one-axis-deflection series

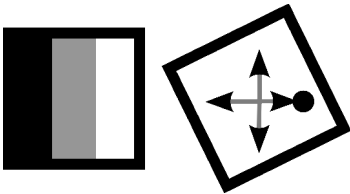


transform coordinate



- 3. **determine center-position**

- 4. to 7. **one-axis-deflection series**
 pattern in x , y , $-x$ or $-y$



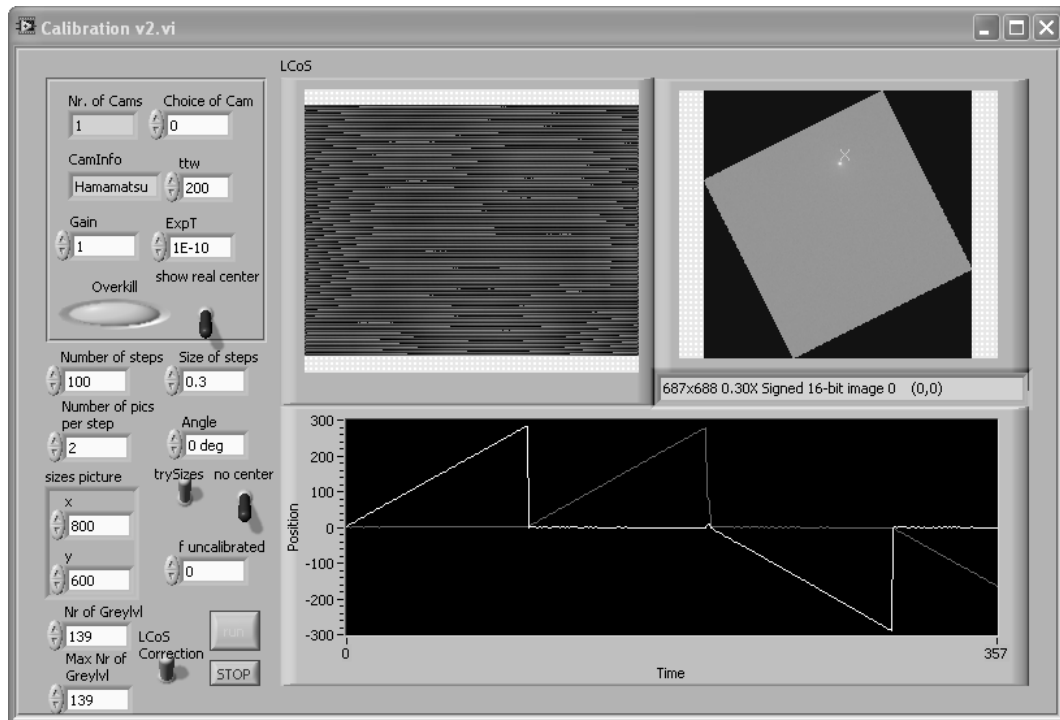
deflection from center-position



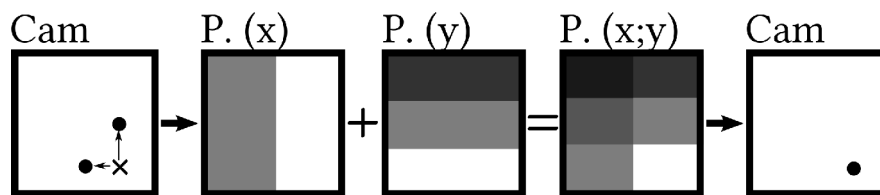
Pattern	Cam	Pattern	Cam	Pattern	Cam	Pattern	Cam	Pattern	Cam

f 3.xv: Calibration with prism and spot, exemplified steps of stages 4 to 7. Pattern used, measured camera image and resulting deflection calibration curve in x and y .

3.5.1. Optical System

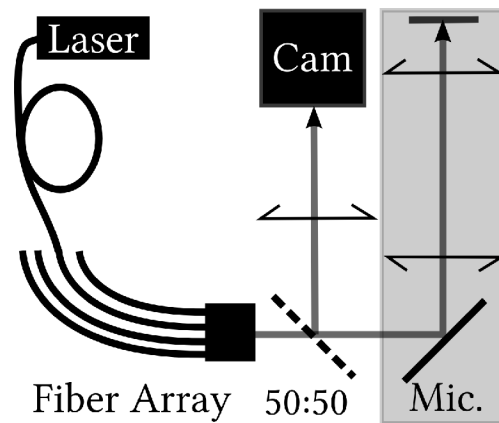


f 3.xvi: LabVIEW user interface of implementation (pattern presentation distorted due to resolution limitations).



f 3.xvii: Free positioning of spot. Position separation in x and y, single axis pattern addition, pattern sum and resulting illumination Cam image.

This method already allows positioning of the spots inside the sample. To find the fiber positions, instead of the APDs an alignment laser was connected to the fibers and a beam splitter mounted into the dual-port C-mount adapter in the image path of the microscope (*f 3.xviii*). The light emanating from a fiber follows the beam path to the objective, is reflected back and partly reflected inside the dual-port adapter towards the camera. Knowing two fiber positions and the symmetry of the fiber array, all 16 positions can be calculated. Since the positioning of the spots is already calibrated to the camera image, it is now possible to create a pattern on the LCoS that result in 16 spots overlapping with the fibers. Afterwards, the positions could be optimized manually to correct for the tolerances of the positions in the fiber array.



f 3.xviii: System with alignment laser connected to a fiber of the fiber array to determine relative position of the fibers towards the camera.

Although the imaging system should be stable and the changes of the optical path towards the camera are corrected fast and automatically, the correct alignment of the spots towards the fibers needed corrections too often due to relative mechanical drift of the camera and the fiber array.

3.5.2. Point detector based calibration

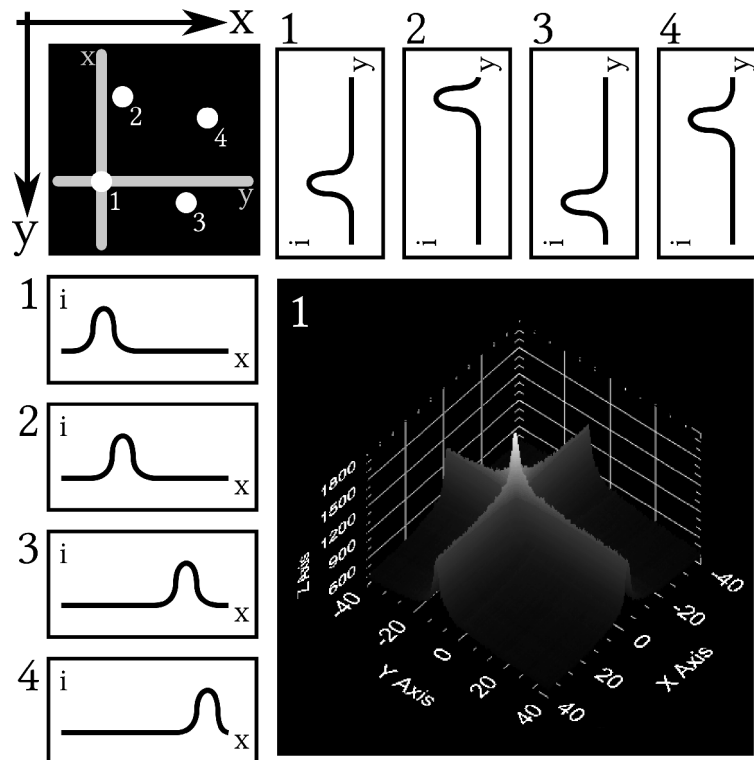
The hardware controlling the illumination and the APDs were combined to allow a direct calibration. In case of point detectors, it is more suitable to scan with line illumination as shown in (f 3.xi) and (f 3.xiv). For each line illumination, the light is focused in one axis. And due to the linearity of the pattern creation, each spot positioned along the line would have the same coordinate values in this axis. The calibration runs comparable with the spot based “Self calibrating, free positioning software”. While scanning with the line in $(x; 0)$ or $(0; y)$, the intensity at each detector is observed (f 3.xvix). Fitting a Gaussian to find the line positions $(x_{max}; 0)_f$ and $(y_{max}; 0)_f$ that create the maximal intensity at fiber f , the needed spot illumination for this fiber is at $(x_{max}; y_{max})$ (f 3.xx). The same corrections for position errors of lenses and mirrors perpendicular to the beam path or the reflection angle of the LCoS are included. This procedure is implemented in the “Self calibrating fiber coupling software”. The duration of calibration is about 3-5 min. An example is shown in chapter 4.1.2.

Because the deflection of the light is created by tilting the beam relative to the lens of the back focal plane of the objective (f 3.i), the calibration is balancing a non perpendicular beam.

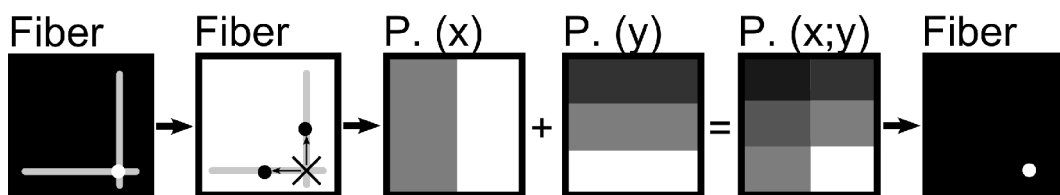
3.5.2. Optical System

But still it is important to pass the objective along its center line with a collimated beam to achieve the smallest confocal volume.

Calibrations done for a specific range of colors (c_{max}) representing a 2π phase-shift for wavelength I can be adapt to another range for a different wavelength II by multiplying x and y with a correction factor $f_{cor} = c_{max, II} / c_{max, I}$.



f 3.xvix: Calibration with line, exemplified steps. Lines on fiber array with 4 detectors are scanned in x and y .



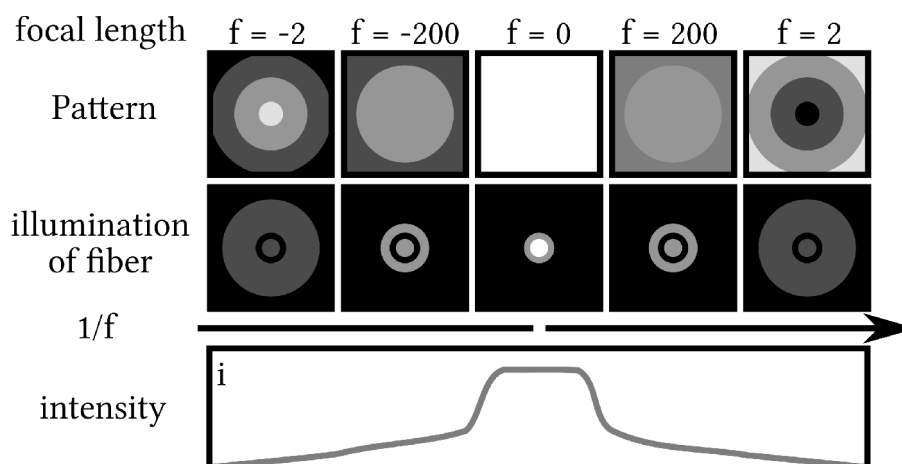
f 3.xx: Positioning of spot. Position separation in x and y , single axis pattern addition, pattern sum and resulting illumination of fiber.

As a further improvement of the position of the illumination spots, a calibration in the axial dimension was implemented. Using the calibration resulting out of the “Self calibrating fiber coupling software”, the light is aligned to all fibers. If the excitation volume is not positioned in the conjugated plane of the detectors, the emitted light will be focused before or after the fiber.

Therefore the light will not be efficiently collected by the fiber. Using a single lens patterns for each fiber, the focal length was scanned for converging and diverging lenses and the collected photons measured. A double Gaussian fit on the intensity graph finds the maximum intensity, representing the optimal lens correction. Substituting $1/f$ for f and ignoring $f = 0$, a linear axis for the focal length parameter working for a fit was accomplished (*f 3.xxi*). The axis transformation is not linear and therefore the fit had to be weighted accordingly. The duration of calibration is about 10 min. An example is shown in *chapter 4.1.2*.

Single lenses per fiber are not only preferable to correct each fiber independently (e.g. to correct a tilted fiber array) but needed because a single lens would change the z position of the rotation center of the x - y correction. The positioned spots would migrate out of position.

For the z correction it is important to consider the influence of the pattern to the illumination path. If the (non deflected) beam does not pass the objective lens perpendicular, also the single lens pattern will result in a slight shift and no calibration can be achieved. The best result with respect of alignment will be found by an iterative calibration in x - y and z . Opposite to the x and y correction, the z correction does not only displace the position of the confocal volume, but also influences the total diameter of the illuminated confocal volume, because it changes the collimation of the beam in front of the back focal plane. In case of a perfect positioned fiber array in the image plane of the microscope, the z correction will optimize the collimation for this will fit best.



f 3.xxi: Calibration of focus with lenses. Focal length, pattern of lens, resulting illumination of fiber end and the intensity graph against $1/f$.

3.5.3. Optical System

3.5.3. Direct search and simulated annealing algorithm for pattern improvement

In a first attempt, the algorithm was planned to correct the uneven reflecting back of the Holoeye LCoS and the imperfect optical lens system. Primarily it should increase the intensity of each illuminated spot and the uniformity of the intensities of all spots. Furthermore the shape of the confocal volume should have been adapted to a perfect autocorrelation curve using a well known fluorophore in dilution. While a background correction was given for the later used Hamamatsu LCoS, the optical lens system is already partly corrected by the calibration software. A phase modulation pattern found with other methods could be corrected for daily variability of the system alignment by testing additional merged prism and lenses atop the known patterns. This was no longer needed after the implementation of the fast “Self calibrating fiber coupling software”. To improve the uniformity, another phase pattern addition algorithm would be faster and therefore more suitable. The use of the autocorrelation curve as parameter suffers from long measurements per step (full run would take 800×600 pixels \times 256 colors \times 10 s measurement \cong 38.9 a) and a too high noise compared to the influence of pattern changes.

Improving the noise ratio, reducing the number of changes and using a long time stable system, the algorithm can improve any pattern.

The simplest way to find a solution to a discrete problem is testing all possible parameters. In many cases, such brute-force methods need too many steps. But in some cases, the problem can be minimized and the number of required steps can be reduced by changing only some parameters and quantifying the influence of the change. Changes resulting in an improvement were accepted, changes resulting in a degrading were mostly discarded. To overcome local extrema and converge to the absolute minimum, degrading changes must have a probability to be accepted.

Provided that the signal to noise ratio is sufficient, the influence of each change is measurable and given enough time, any measured parameter can converge to an optimum. The implementation of such algorithm had been described for finding or optimizing phase patterns for optical traps [Leonardo 2007].

The algorithm was implemented as described in [Meister 2002]. In the direct search algorithm a cost function C describes the inverted quality of an approach and should be minimized. Primary only changes reducing the cost were accepted. For an SLM device with M pixels and c_{total} possible values per pixel:

$$L = (c_{total} - 1) \quad (\text{e 3.xii})$$

M tested changes were defined as one search cycle. Due to the changed influence of each pixel after changing any other, the search cycles have to be repeated till no lower cost can be found. Introducing a finite chance for accepting changes resulting in a higher cost, local minimum on the cost function can be overcome. In this process, known as simulated annealing, the probability of accepting those changes is set to:

$$p = \exp(-\Delta C_i / T), \quad (\text{e 3.xiii})$$

depending on the increase of the cost ΔC_i and a value named temperature T . In a first attempt, T could be decreased for each following cycle by a constant factor $0 < \alpha_T < 1$. The temperature in cycle $k+1$ is therefore given by:

$$T_{k+1} = \alpha_T T_k \quad \text{with } 0 < \alpha_T < 1. \quad (\text{e 3.xiv})$$

From this point, several obvious improvements of speed can be made. First, the number of steps of each cycle could be reduced by decreasing M (merging several pixels) or c_{total} (using less number of different values). Secondly, a more accurate temperature would reduce the number of required cycles and reduce the probability of dead ends in local minimum. This step was implemented by replacing the factor of decreasing temperature α_T with a factor to decrease the probability of accepting bad changes:

$$p_{A,k} = \alpha_p p_{A,k+1} \quad \text{with } 0 < \alpha_p < 1 \quad (\text{e 3.xv})$$

3.5.3. Optical System

Furthermore the temperature was derived from $p_{A,k}$ and costs ΔC_i of the last cycle of changes. The cycle L was divided in sub cycles of the length $m = L/n$. Each cycle of m changes uses a constant temperature, accepting bad changes with a probability of $p_{A,k} = \exp(-\Delta C_i/T)$. During the cycle, all ΔC_i of an accepted bad changes were recorded. After each cycle of m , a new temperature will be calculated with:

$$p_{A,m} = \sum_{i=1}^a \exp\left(\frac{-\Delta C_i}{T}\right) \quad (\text{e 3.xvi})$$

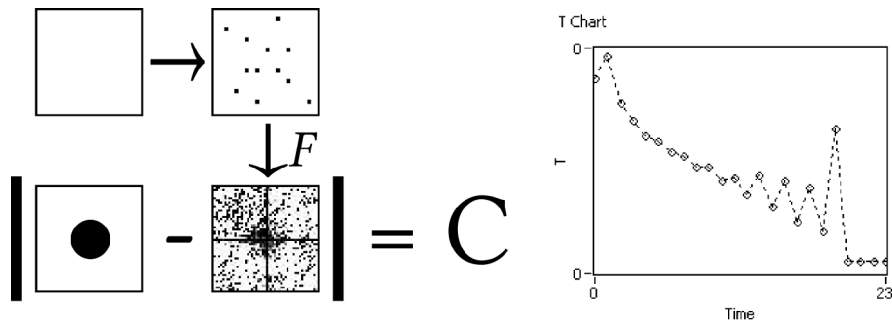
Following n cycles of m changes, equal to one cycle of L , p_A will decrease by factor α_p and the next temperature T is calculated with the new value. The cycles of L were repeated until a certain value of the resulting cost function is achieved (*f 3.xxii*).

Even using an iterative approach of finding a correct temperature, a single cycle with a wrong chosen or unfortunately calculated T could result into too many bad changes. This could happen in particularly while the first cycle after choosing a start temperature and a start condition (e.g. SLM pattern) of unknown quality and cost function. Therefore, the first cycle should only be used to find an acceptable T and all changes done in the first cycle were undone by reloading the starting conditions afterwards.

In addition, a securing algorithm inside a cycle of m compares the changes in cost of all accepted changes, good as bad ones, with a threshold, creating a so called quasi-equilibrium [Lam 1988]:

$$-dC_- < (C - \Delta C_i) < dC_+ \quad (\text{e 3.xvii})$$

If a certain number of changes outside this threshold is accepted, before the same number of changes inside the threshold were made, the temperature was badly chosen and the cycle of m ends to restart with a newly calculated T . Otherwise, the securing algorithm ends and the cycle of m proceeds. While the upper limit is good to avoid destroying a given pattern with a single bad calculated temperature, the lower limit reduces the risk of becoming trapped in a local minima caused by some few steps reducing the cost function too fast.

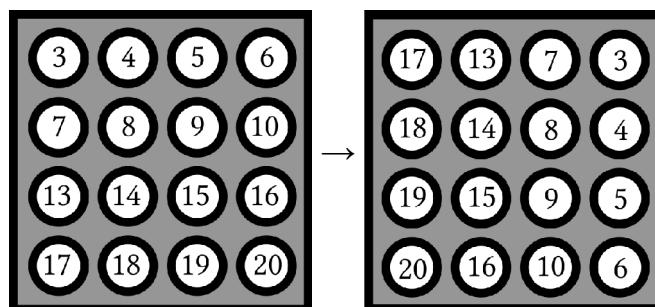


f 3.xxii: Example of a dbp cycle. On a empty image, a pixel is added. After a Fourier transformation, representing a lens, the image is compared with a desired image. The temperature is adjusted until a stable minimum is found. Example shows a 100×100 pixel binary image after 2 h of optimization.

The software is able to compare images (with or without Fourier transformation) and correct them per changing pixel or per shifting (LCoS control pattern), including live images taken with the Hamamatsu camera.

4. Applications

The SRFCS system is designed for multifocal fluorescence correlation spectroscopy. Before it can be used, a sequence of calibration measurements have to be done to align the confocal volumes towards the fiber array (*f 4.i*) (*chapter 4.1*).



f 4.i: Numeration of the 16 fiber channels. Because of the rotation of the camera, the fiber array on images is tilted. Following the drivers of the photon correlator card, channels 1, 2, 11 and 13 belong to different connections. Channels 3-10 and 13-20 use separated memory on the photon correlator card.

To achieve interpretable results, a linear dependency between fluorophore concentration and the detected photon counts is utterly required and signal saturation of the detector has to be avoided. Furthermore the sizes of the confocal volumes need to be known (*chapter 4.3*).

4. Applications

Aware of the position of the fibers and the measurement conditions, the system is applied to living cells in microscope dishes.

A positive control for dimerization is done with with mono and double Citrine transfected cells (*chapter 4.4*).

To map dimerization, Rapamycin-induced fusion of FRB and FKBP (*chapter 4.5*) was observed. As a complex biological problem, EGF-induced dimerization of Erk2 (*chapter 4.6*) was observed with additional negative (inhibited) control measurements.

All measurements were performed at room temperature (20°C) with a 488 nm laser, a 488 nm dichroic mirror (Semrock Di01-R488), a 531/40 emission band pass filter (Semrock FF01-531/40) and a 60x Oil objective (NA 1.35, UplanSApo, Olympus). If not otherwise stated, the laser intensity in front of the SLM was 6.3 mW.

All cellular experiments were performed using HeLa human cervical adenocarcinoma cells (American Type Culture Collection) [Gey 1952] (*a4.i*). HeLa are robust, easy to transfect and to handle, and respond to epidermal growth factor (needed in *chapter 4.6*).

For all calibrations and measurements, software written in LabVIEW 2010 (National Instruments) and based on drivers provided by the companies Hamamatsu (camera) and Becker & Hickl GmbH (photon correlator card) was used. The data extraction, autocorrelation and fit were performed by Python scripts written by Dr. Hernán Grecco.

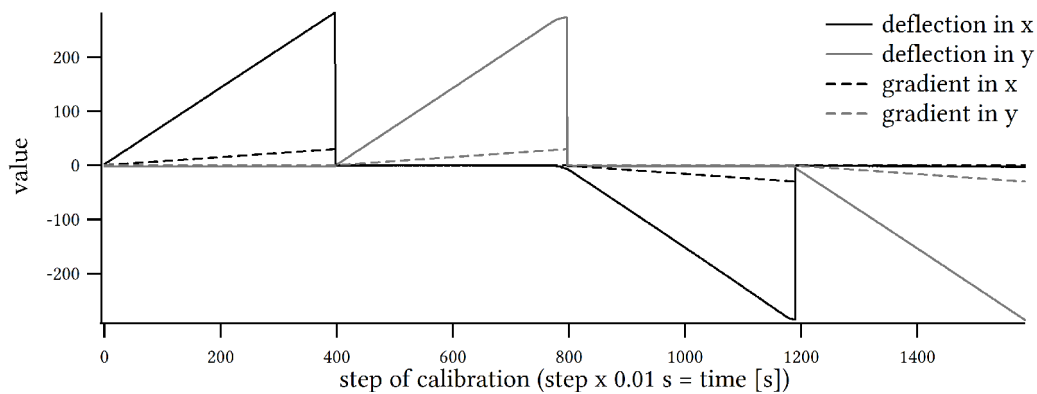
To determine the ratio of monomeric and dimerized fractions and separate the brightness per fraction, Fluorescence cumulant analysis (FCA) (*chapter 2.3 & chapter 7.3*) was performed. The analysis was performed by Python scripts written by Dr. Hernán Grecco.

4.1. Calibration of the positioning

Three modes of calibrating the positioning of the illumination distribution were operated, one mode for free positioning in x and y on a camera plane (*chapter 4.1.1*) and two modes for automated aligning in x and y , respectively in z , to the fiber array (*chapter 4.1.2*).

4.1.1. Camera based calibration

The first method used for calibration of the x and y position of the light distribution traces the position of a single illumination spot on the camera, as further described in *chapter 3.5.1*. After calibration, each position on the camera is allocated to parameters x and y . The axes starting from the origin at the center of the camera is measured sequentially up to a threshold, creating a sawtooth shaped calibration curve. For camera based calibration with a fluorescent plate, 1% of the laser power is used (~ 0.063 mW).



f 4.ii: Calibration of x and y on a fluorescent plate with camera, allocates a deflection value (in pixels) to each gradient value defining a prism pattern.

If the origin is not centered or the maximum deflection created by the gradient is too high, the deflected spot will leave the camera sensor in one or multiple slopes. This will result in an aberration in x and y first, as the slope of the Gaussian laser illumination is near the border of the sensor area (slightly visible in *f 4.ii* on the second maximum) and random data afterwards, as the tracing script determines the position of the brightest camera noise signal.

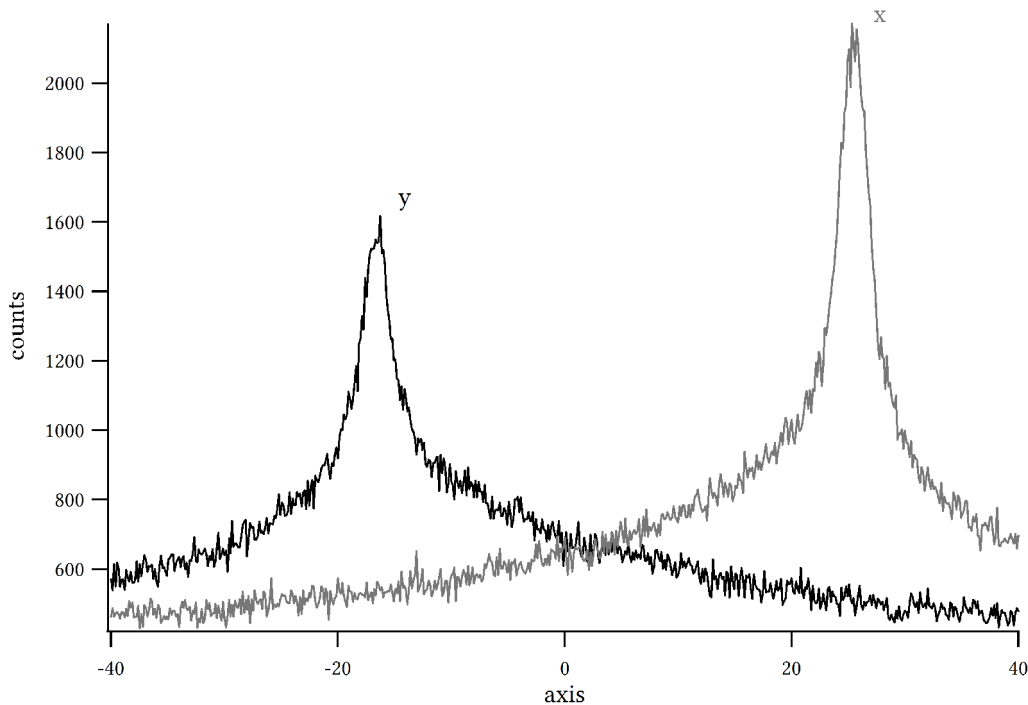
As each point of measurement is detected for an exposure time of about 10 ms, the intensity fluctuations induced by the device should be compensated.

To achieve a consistent calibration, each slope is fitted with a line and statistical outliers (found in case of Holoeye Heo 1080P) are dismissed. Positions between measured deflection points can be extrapolated. If the calibration is done properly, positioning can be achieved with one pixel precision.

4.1.2. Applications

4.1.2. Point detector based calibration

The second method directly determines the gradient parameters x and y for the positions of the fibers (*chapter 3.5.2*). To correct for the glass plate of the microscope object dishes, this calibration is performed using a solution of diluted fluorophores (preferable in the same kind of microscopy slide used for further measurements). An illuminated line is scanned up to a chosen threshold, while the photons in each fiber are detected by APDs. The dwell time per scan step is 10 ms.. The illumination intensity has to be adapted to the fluorescent dilution, but is in the same order of magnitude as for a single volume FCS measurement: about 4% of the laser intensity is used (~ 0.25 mW) for a $1 \mu\text{Mol/l}$ Oregon Green 488 dilution in water.

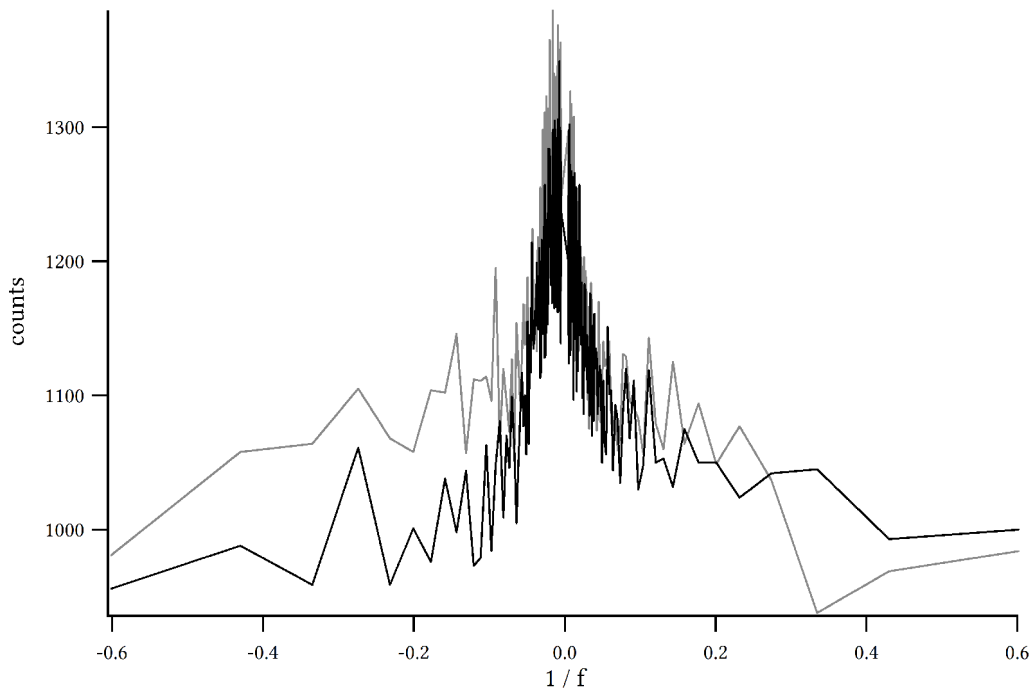


f 4.iii: Calibration of a fiber position in x and y on Oregon Green 488 in dilution with a 488 nm laser and an APD. Exposure time per position 10 ms.

The calibration curves are the convolution of a Gaussian beam profile and a detection pinhole (*f 4.iii*). To determine the peak position, it can be fitted with a double Gaussian fit. This is performed by subtracting the first Gaussian fit with a broad threshold value for the full width at half maximum (FWHM) and a second Gaussian fit to determine the center of the Gaussian afterwards. Even by manually changing the gradient parameters, it is not possible to improve the emission adjustment in x and y .

The z calibration in usage of additional lens pattern (as described in chapter 3) is very sensitive to the angle of the laser hitting the back focal plane of the objective. If it is not 90° , the z correction is not discrete to x and y and the illuminated spots migrate while the focal length of the lens pattern is changed. The calibration can be run alternating to the calibration shown before. Because the illumination beam is split into 16 beams, for this calibration the laser power has to be increased. At least 10% of the laser power is used (~ 0.6 mW) for a $1 \mu\text{Mol/l}$ Oregon Green 488 dilution in water.

For the calibration a threshold for the maximal used focal length (parameter) and for the minimal used focal length (parameter), each the same for positive and negative have to be chosen.

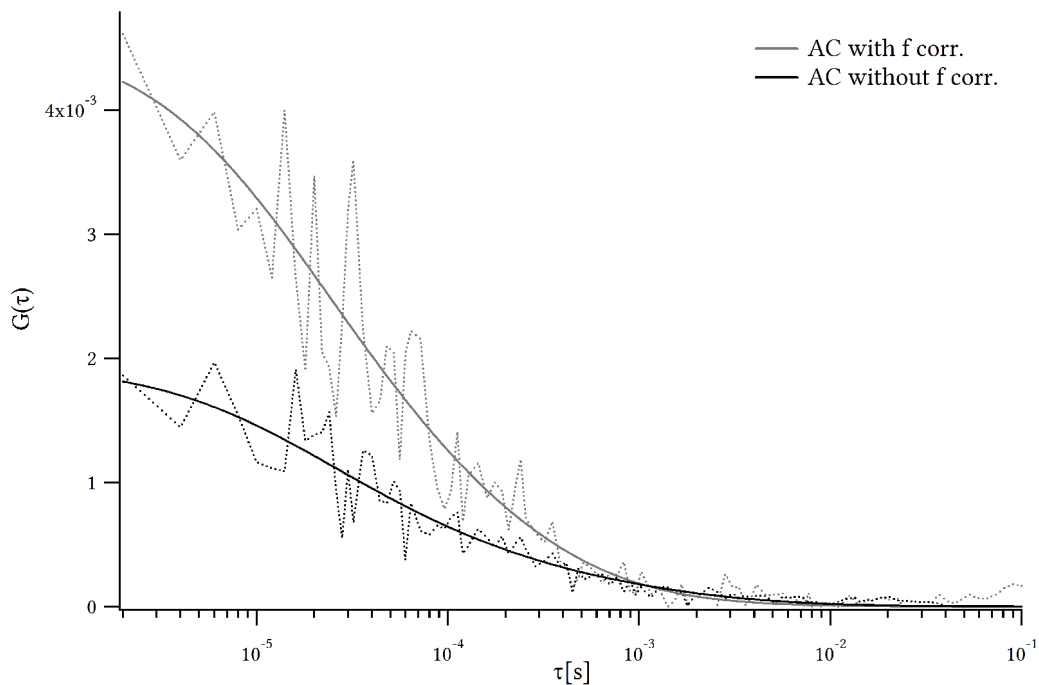


f 4.iv: Calibration of two fiber positions in z on Oregon Green 488 in dilution with a 488 nm laser and APDs. Exposure time per position: 20 ms.

For the calibration curve, the axes representing the focal length parameter is transformed to $1/f$. Because of this transformation, the amount of points decrease logarithmic to the slopes ($f 4.iv$). The measured points have to be weighted for the fits to compensate the axes transformation. The shape of the calibration curve depends on the threshold parameter. A Gaussian fit can be used to determine the center position, once the Gaussian shaped background is subtracted.

4.1.2. Applications

Decreasing sizes of the confocal volume were found (*f 4.v*).

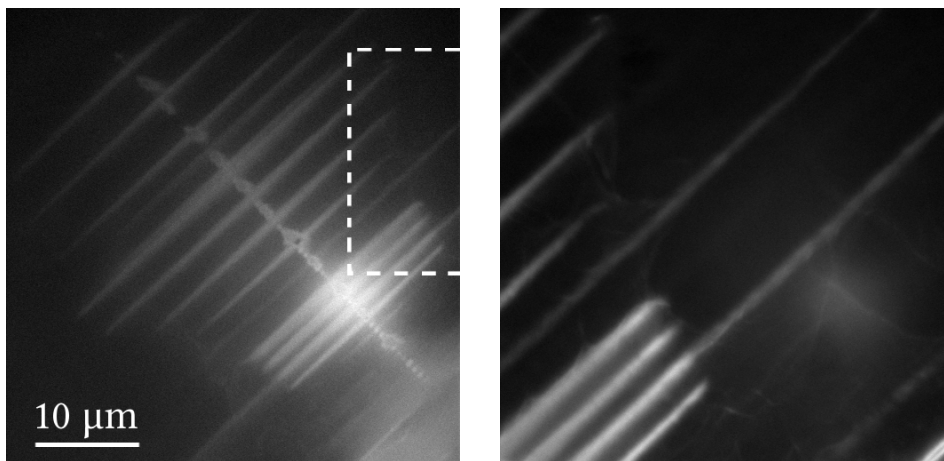


f 4.v: Autocorrelation of Oregon Green 488 in dilution in water with a 488 nm laser done with a calibration in x and y and x , y and f respectively. Measurement duration: mean of 3 times 10 s per trace.

4.2. Light distribution geometrics for patterning of proteins

Using the calibration of the spot deflections, it is possible to position dots, donuts, and lines. These illumination distributions were used for light induced patterning on surfaces following a slightly changed recipe from literature [Belisle 2008] (*a 4.ii*). With SLM modulated illumination: [Belisle 2009].

The images were taken using the Fluorescence illumination system and a RFP filter cube (U-MRFPHQ, Olympus).

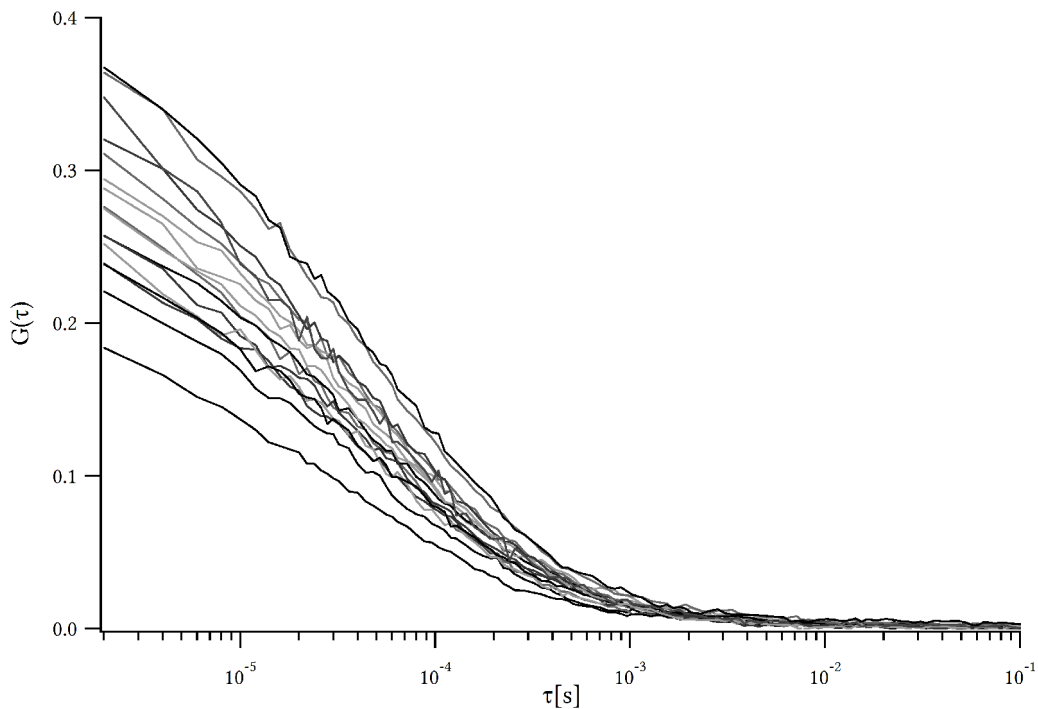


f 4.vi: Example of line illuminated pattern with varying length of line and illumination duration. Left side: 20x Air, on the right the marked area with a 40x Oil objective.

The images show pattern with various line lengths created with a 20x Air objective and illumination durations between 1 s and 60 s per line (*f 4.vi*). The width increase with the illumination duration and intensity. It varies between 1.032 μm and 1.892 μm . On the middle line perpendicular to the line pattern, various ghost dots illuminated the substrate during each bleaching duration. For regular application, complex pattern of multiple lines, dots or donuts can be illuminated and printed parallel.

4.3. Calibration of confocal volume and intensity distribution

After aligning the illumination to the fiber array, autocorrelation for up to 16 channels can be measured (*f 4.vii*).



f 4.vii: Autocorrelation measured in 16 spots in mCitrine dilution in water. Measurement duration: 10 s.

Although the concentration of the dilution sample is homogeneous, the autocorrelation curves differ. This indicates that the confocal volumes differ (standard deviation about 19%). The differences are caused by the illumination distribution, detector noise distribution of varying APDs, aberrations of the optics including the objective and fiber angle misalignments inside the solid array. To interpret the measurements, the characteristics of each confocal volume and the illumination has to be known.

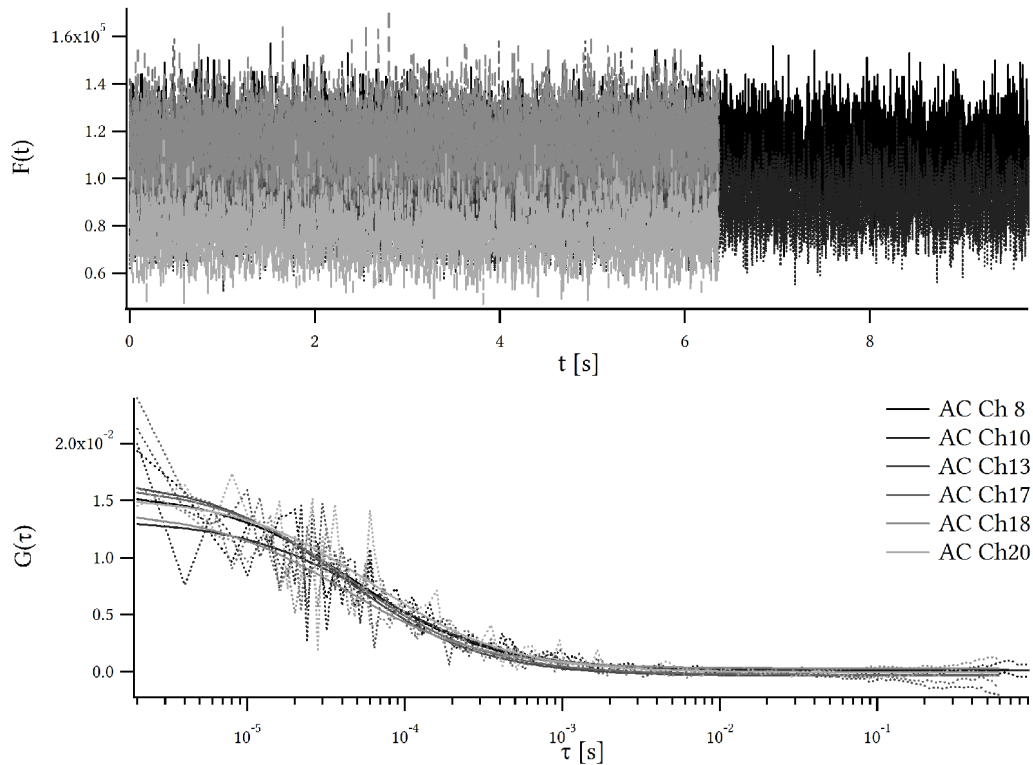
Furthermore, the detection efficiency has to be linear over the range of detected and processed photon counts. The results of the autocorrelation has to change linear to the concentration of measured fluorophore dilution (*chapter 4.3.1*).

The illumination of the varying confocal volumes have to be in the same scale and a compromise between number of counts and bleaching of the fluorophores (*chapter 4.3.2*).

4.3.1. Linearity of detected fluorescence intensity

Typically multiple intervals of 10 s are acquired as one 'repeat' of the measurement. The software is programmed to measure a repeat in a single recording, but saves and process sequences of about intervals length. The actual intervals length can differ for < 0.01 s. This influences the total counts detected, but not the shape of the autocorrelation curve. If the total counts of multiple channels have to be compared, the counts could be normalized to counts per second using the measurement duration or a single interval per repeat should be used. As an advantage, the intervals can be joined to a continuous sequence. Furthermore, due to continuous readout, the solution increased the maximum counts processable. Linearity of the quantum efficiency of the detection and processing hardware is given in all measurements. The APD array consists of four arrays with each four APDs. A single four channel array can count up to $1.5 \cdot 10^6$ counts/ s continuously (peak count rate $4 \cdot 10^6$ counts/ s). Two of these arrays are connected to one working memory of the photon correlator card. It was empirically found, that the working memory and the communication between the photon correlator card and the computer limits the counts per $2 \cdot 4$ APDs to about $1.2 \cdot 10^6$ counts/ s. Therefore the photon correlator card and processing is the limiting factor during measurement. If the photon correlator card recognize an overflow of the working memory, the developed software stops the measurement interval and the measurement data remain consistent (*f 4 viii*). However sequently measured intervals are no longer consistent and therefore can not be joined to a continuous sequence.

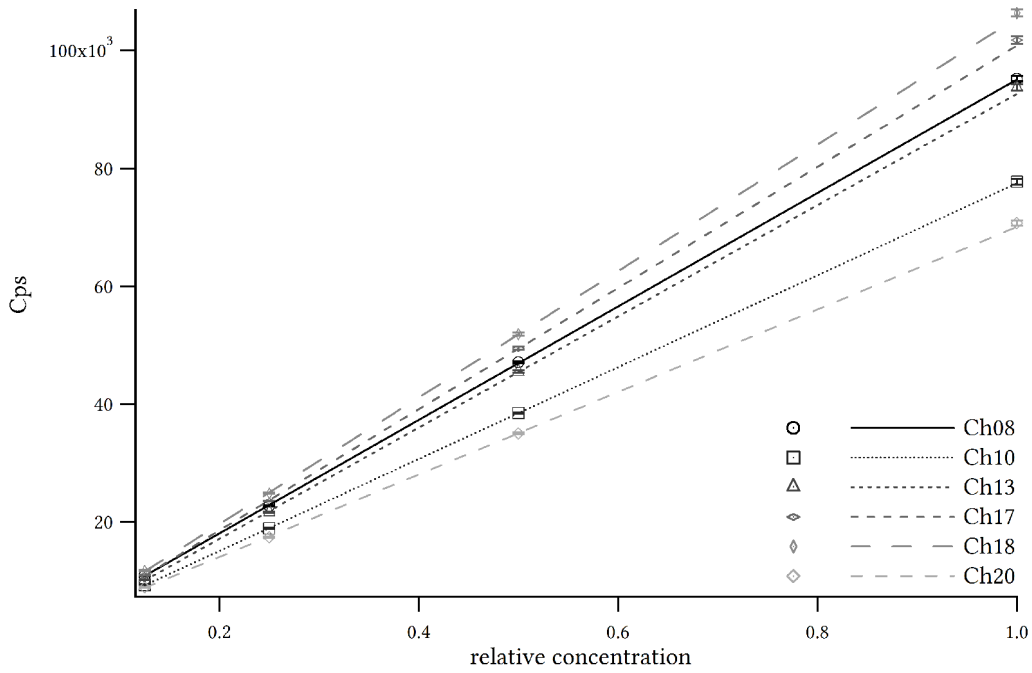
4.3.1. Applications



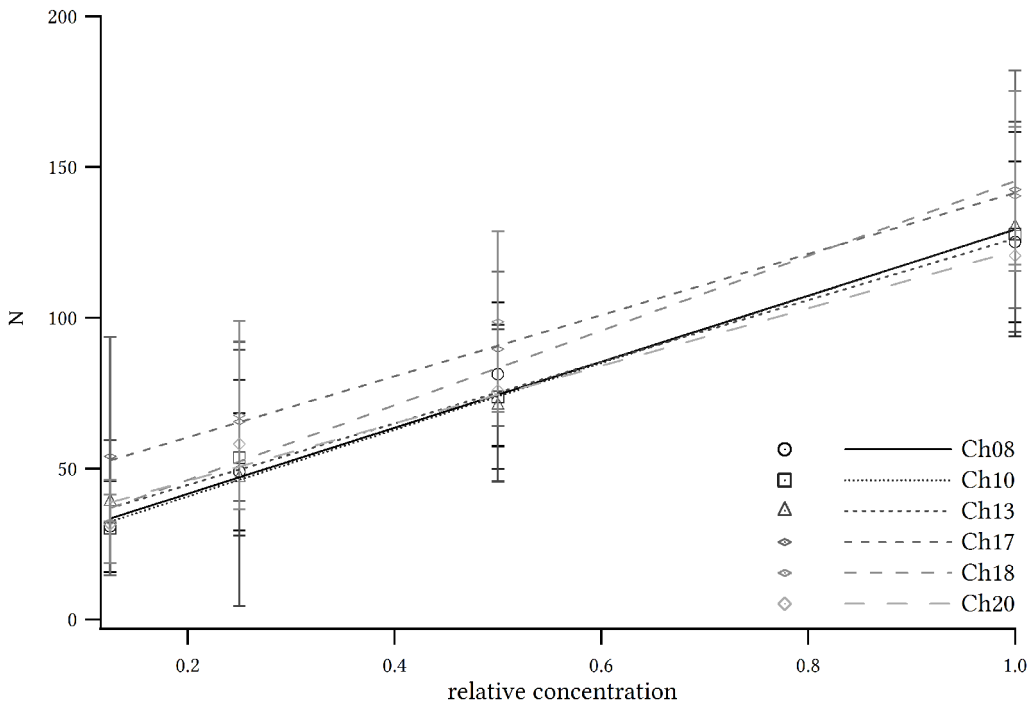
f 4.viii: Example of Oregon Green 488 dilution in water measured in 6 volumes parallel. Intensity traces for Oregon Green 488 dilution in water measured in 6 volumes parallel. Measurement duration: Channel 8, 10 for 10 s, Channel 13, 17, 18, 20 continuously/ without reduction of counts until overflow break-off after 6.37 s.

For *f 4.viii* six channels of comparable detector noise were chosen and result in similar autocorrelation curves (standard deviation about 10%).

To prove the linearity, dilution series of fluorophores in water were measured. *f 4.ix* shows the intensity traces for six parallel measured channels with constant illumination. The measured sequence started with 100% and was diluted to about one eighth of the initial concentration with water. The intensities follow these steps proportionally, although bleaching reduces the counts for low concentration. The curves for the different channels converge, because the start counts at 100% differ because of varying confocal volume sizes (e.g. $100 - 60 = 40$, but $100/4 - 60/4 = 10$).



f 4.ix: Counts per second of a series of varying dilutions of Oregon Green 488 excited with a 488 nm laser for six parallel aligned confocal volumes. Each point measured for 10×10 s.

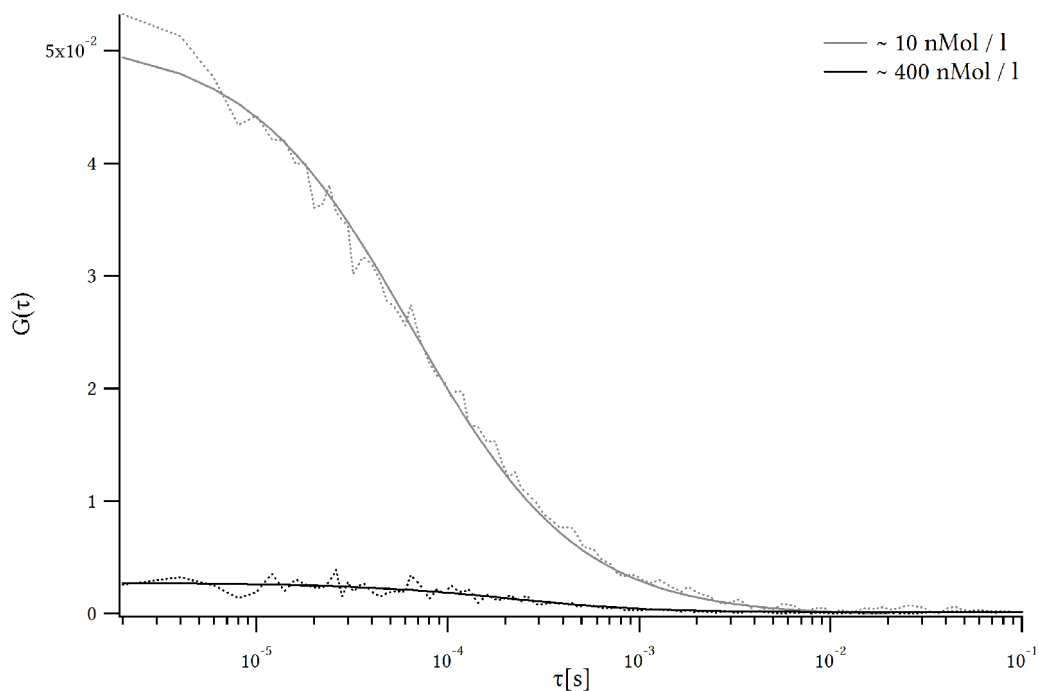


f 4.x: Number of particles in six parallel aligned confocal volumes for varying dilutions of Oregon Green 488 excited with a 488 nm laser. Each point measured for 10×10 s.

4.3.1. Applications

After processing the time data with autocorrelation and fitting the curves, the number of particles measured for each measurement is plotted in *f 4.x*. The error bars rise, as the quality of the fits can vary. Five of the volumes show a proportional decrease with the concentration as expected. Channel 18 decreases not parallel to the other channels. This can be induced by a non perfect alignment creating a non Gaussian confocal volume and complicating a precise fit.

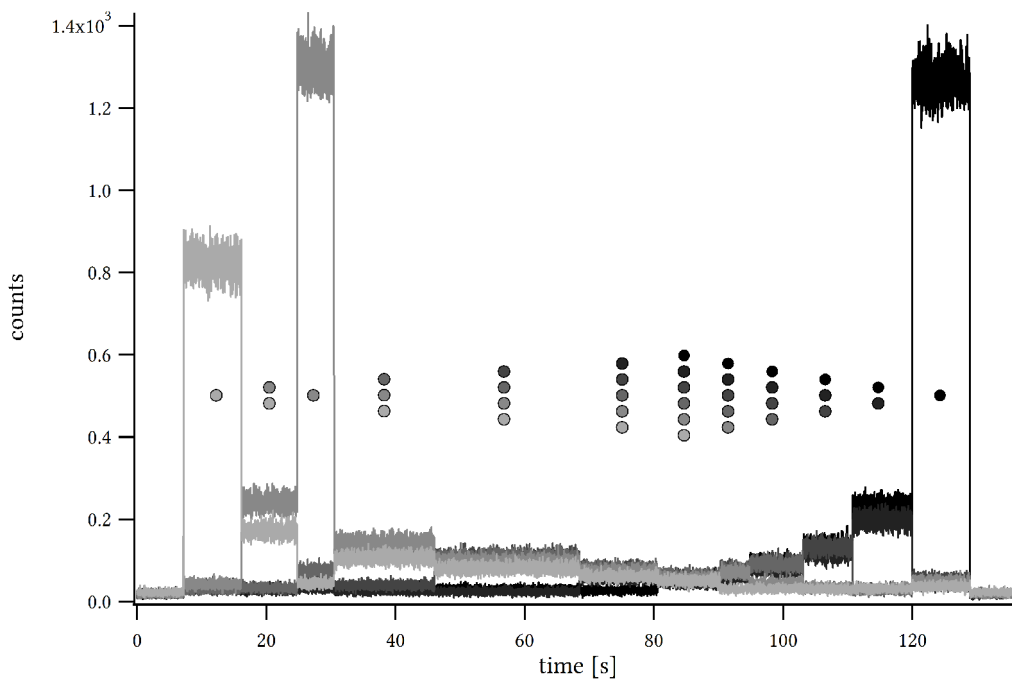
The dilution series covers the range of counts measured in cells. Much higher counts overflow the photon correlator card and lower counts can produce imprecise fits. The actual concentrations measurable depend also on the illumination intensities. With varying illumination, a range of Oregon Green 488 concentrations from about 10 nMol/ l to 400 nMol/ l in water were measured (*f 4.xi*).



f 4.xi: Examples of the range of Oregon Green 488 dilutions in water measured in 6 volumes. Measurement duration: 10 s.

4.3.2. Excitation distribution

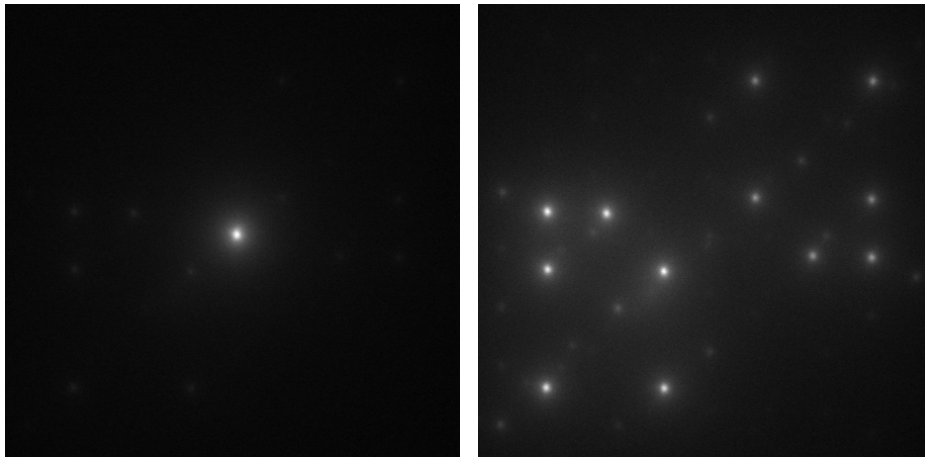
To estimate the laser power per volume and to estimate the uniformity, measurements comparing the photon counts for varying numbers of parallel illuminated volumes were performed.



f 4.xii: Intensity measured at 6 fibers with varying number of excited volumes and fixed total laser power. The first single aligned fiber is weaker, indicating a non perfect aligned volume. As multiple fibers are aligned, the light is split between them and additional, not measured ghost traps.

In average, one spot out of 6 illuminated spots is excited by 5% of the light, a single positioned spot would be exposed to (*f 4.xii*). The rest is partly blocked by the center light blocker, but partly be focused into ghost traps.

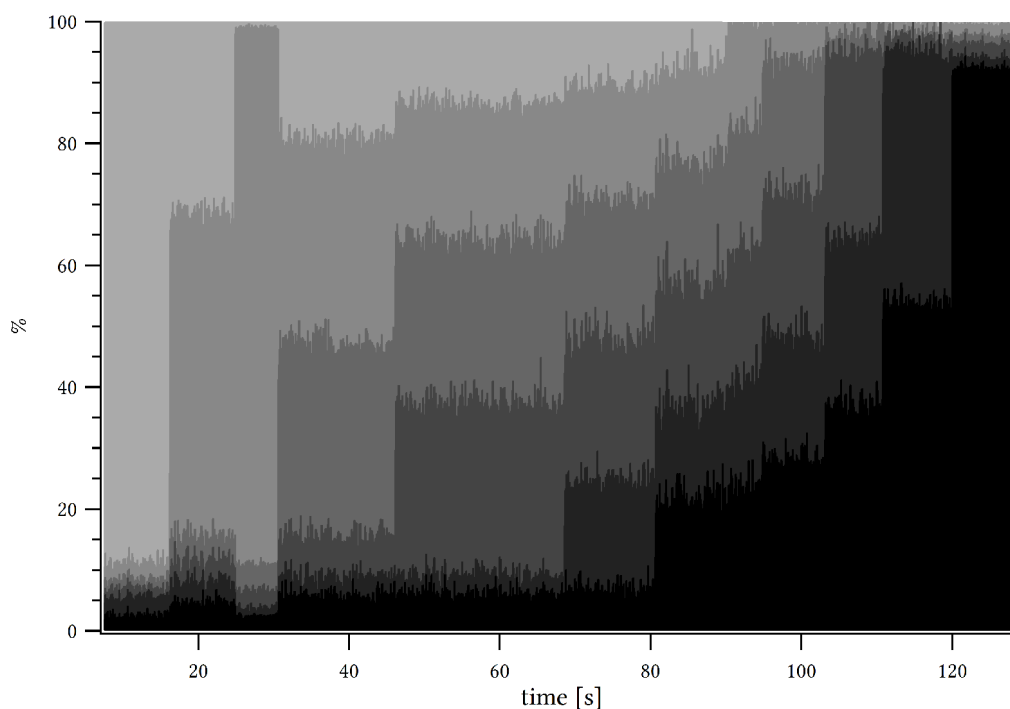
4.3.2. Applications



f 4.xiii: Image of 6 spots in Oregon Green 488 without the centered light blocked and with blocker. Aimed spots lower left of center position.

The centered light binds about 11 times the light of a single aimed spot, therefore more than 50% of the excitation light (*f 4.xiii*). About 15% are focused in the six strongest ghost traps on a position point symmetric mirrored to the center light position.

In FCS, typical laser power in the sample for a single confocal volume were recommended between 0.25-0.5 mW [Rigler 1993]. For this system, a good compromise between bleaching and signal to noise ratio for 6 confocal volumes was found for an average intensity of about 0.05-0.16 mW per volume. For these intensities, the sample plane is exposed to 1-3.15 mW (a single positioned spot in *f 4.xii*), or 50% of it in case the centered light is blocked (*f 4.xiii*). A higher intensity bleaches most cells too fast or exceed the capacities of the photon correlator card, while a lower intensity mostly results in a too weak signal to noise ratio. No autocorrelation curves were achieved with intensities below about 0.015 mW (0.3 mW for a single positioned spot).



f 4.xiv: Percental distribution of light intensity between 6 fibers in various configured illuminations as shown in f 4.xii.

Comparing the intensity distributions between different fibers while illuminating them (*f 4.xiv*) shows a sufficient uniformity between the illuminated fibers (standard deviation for 6 fibers about 4.5%). However, to be able to compare measurements of different fibers, not only the volumes per fiber were determined for each day with a solution of Oregon Green 488, but the brightness, the number of particles and the brightness per particle are normalized separately with the values measured per fiber and in solution.

4.3.3. Applications

4.3.3. Sizes of confocal volumes

It is to consider, that the size of the confocal volumes are influenced by many factors. Small misalignments in the range of micrometers of the lenses of the illumination path, the pinholes (fiber array) or the position of the LCoS affect the volume size. The calibration can correct the misalignment of the excitation path and in case of a perfect excitation path it can correct the illumination path. But any digitalized pattern introduces phase front disruptions whose influence in focusing are not known.

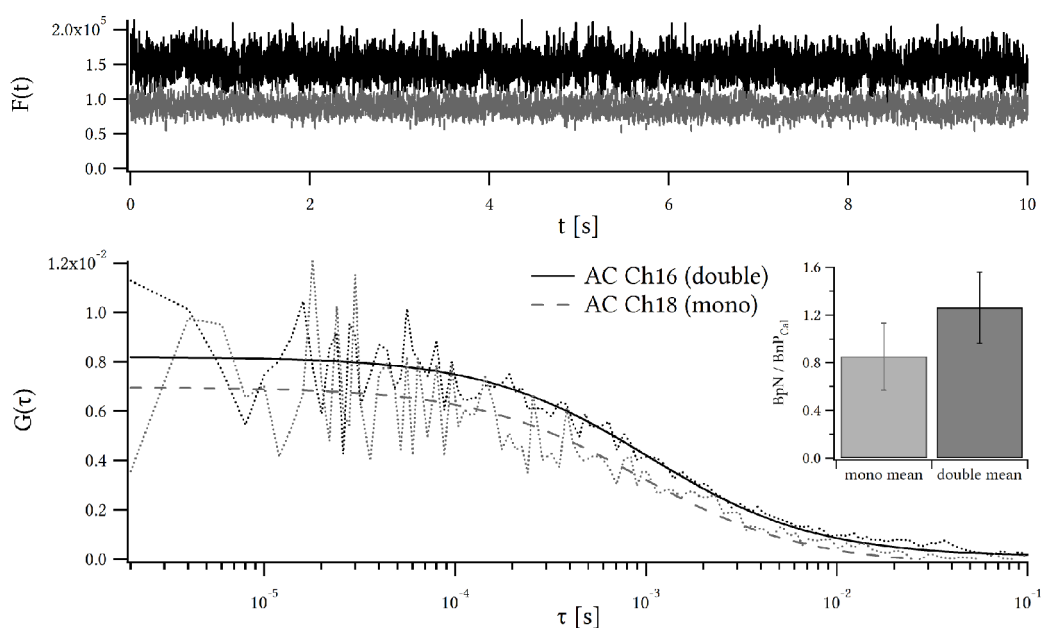
For most calibrations, a dilution of Oregon Green 488 in water was used. Measurements on a Zeiss 510 showed about 14 ± 1.7 particles in a diffraction limited volume with $s = 214$ nm and a volume of 0.22 fl, a concentration of about 65 Molecules/ fl, 101.53 nMol/ l respectively. Typical measurements with 6 confocal volumes counted 60 to 70 (*f 4.viii*), in cases of manual misalignments (corrected by the calibration) up to 100 particles per volume for the same dilution. Therefore the typical confocal volumes are 4.3 to 5 times the volume achievable with the Zeiss (0.95 to 1.1 fl).

Tests to scan the confocal volume with a fluorescent bead in x - y failed because of the imprecise positioning of the automated stage. Vertical line scans in z showed a diameter of at least $1.5 \mu\text{m}$ in comparison to $1.16 \mu\text{m}$ in the Zeiss 510.

The confocal volume size can also be determined if the diffusion coefficient of a fluorescent molecule is known. From the fit and the known diffusion coefficient, the volume can be calculated. As shown in *f 2.iv*, the structure parameter is of weak influence on the fit. Therefore the factor can vary strongly without strong influence on the fit, but on the calculated volumes. In the measurements shown, the structure factor is can either be in the range of 3 to 8 or clearly above up to 200000. The diffusion coefficient of Oregon Green 488 is about $4.11 \pm 0.06 \cdot 10^{-6} \text{ cm}^2/\text{ s}$ at 25°C [Müller 2008] but can vary for stored dilutions because of agglutination. Confocal volumes calculated from with structure factors below 10 resulted to volumes from 0.22 fl to 0.9 fl. The structure parameter and the calculated volume for a single volume resulting from measurements with 10 s duration can vary over this range. An improvement could be achieved by fitting to a mean curve of 10×10 s measurements or joining sequently intervals to a long time measurement and a threshold parameter for the structure parameter for the fit ($1 \leq \sigma_s \leq 10$).

4.4. Discrimination of mono and double Citrine

In order to discriminate between the brightness of monomers and dimers, and to achieve proper positive control measurements, monomeric and dimeric Citrine were transfected in HeLa cells (*a 4.iii*). This approach has the advantage to be not dependent on the requirements of any chemical compound during the measurement.



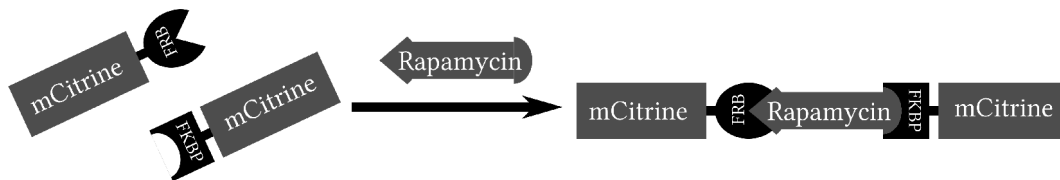
f 4.xv: Autocorrelation and intensity trace in one of 6 channels measured in a cell transfected with monomeric and a cell with dimeric Citrine. The number of particles in the mono cell is higher (amplitude of $G(\tau)$ is lower) while the counts are lower than in the double Citrine cell. Measurement duration: 10 s. Small graph: with a calibration measurement normalized average brightness per particle of all measurements.

Comparing the counts per particle of nine monomeric and eleven dimeric transfected cells, in six confocal volumes each (total measurements: 981 in monomeric, 1129 in dimeric transfected cells, measured with a single calibration), a ratio of 1.48 ± 0.41 was found. The results normalized to the Oregon Green 488 calibration suggest a mixture of monomeric and dimeric, partially bleached double Citrine or reduced quantum efficiency of fluorophores in dimers in the dimeric transfected cells. The counts per molecule for monomeric Citrine in cells is below the counts per molecule of Oregon Green 488 in solution. For the monomeric cells, $0.85 \pm 0.28 \text{ BnP} / \text{BnP}_{\text{Cal}}$ were found, for dimeric cells $1.26 \pm 0.30 \text{ BnP} / \text{BnP}_{\text{Cal}}$ (*f 4.xv*).

4.5. Applications

4.5. Rapamycin-induced dimerization of FRB and FKBP

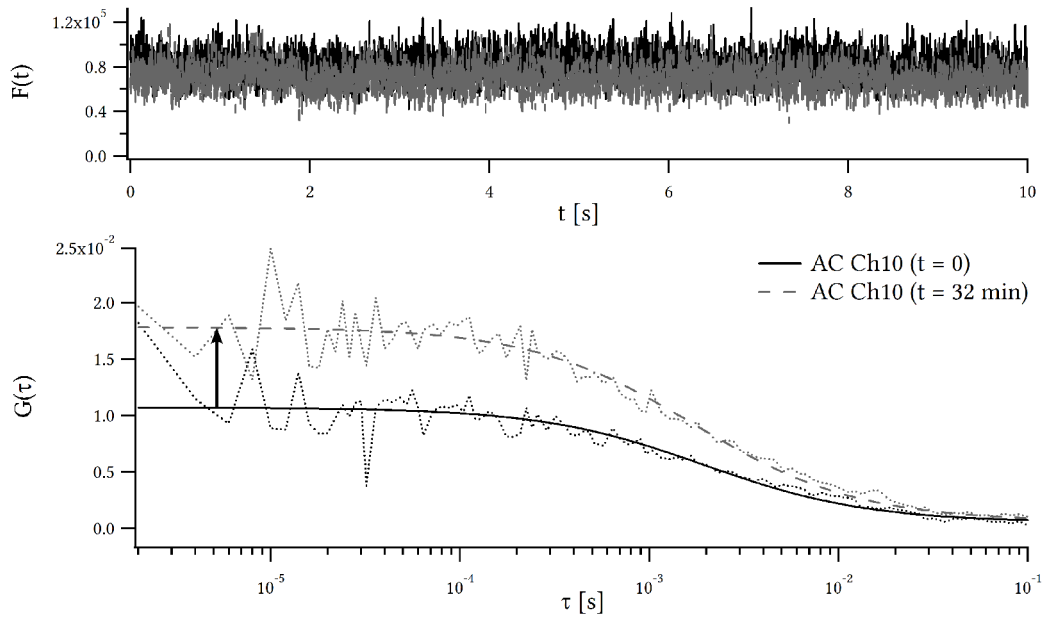
In order to test the system for its compatibility with biological samples and its applicability to observe dynamic processes, known biological systems were used. The rapamycin-induced dimerization of FKBP (FK506 binding protein) and FRB (FKBP-rapamycin binding domain), where both protein-fragments are labeled with the same monomeric fluorescent tag (e.g. mCitrine), displays an ideal system [Chen 1995] to discriminate between mono and dimer fluorophores using sequential FCS measurements. Protocol at (a 4.iv). Rapamycin is a macrolide antibiotic that was discovered in 1975 and isolated from a soil sample, containing *Streptomyces hygroscopicus*, from the Easter Islands. Upon rapamycin-addition, FRB and FKBP are fused together (f 4.xvi). The dissociation constant is 0.2 nM and suppresses dissociation between the fragments. The resulting measurements should then represent constant values for the initial as well as the final intensity, whereas the number of photons per dimerized molecule doubles (e 2.xviii).



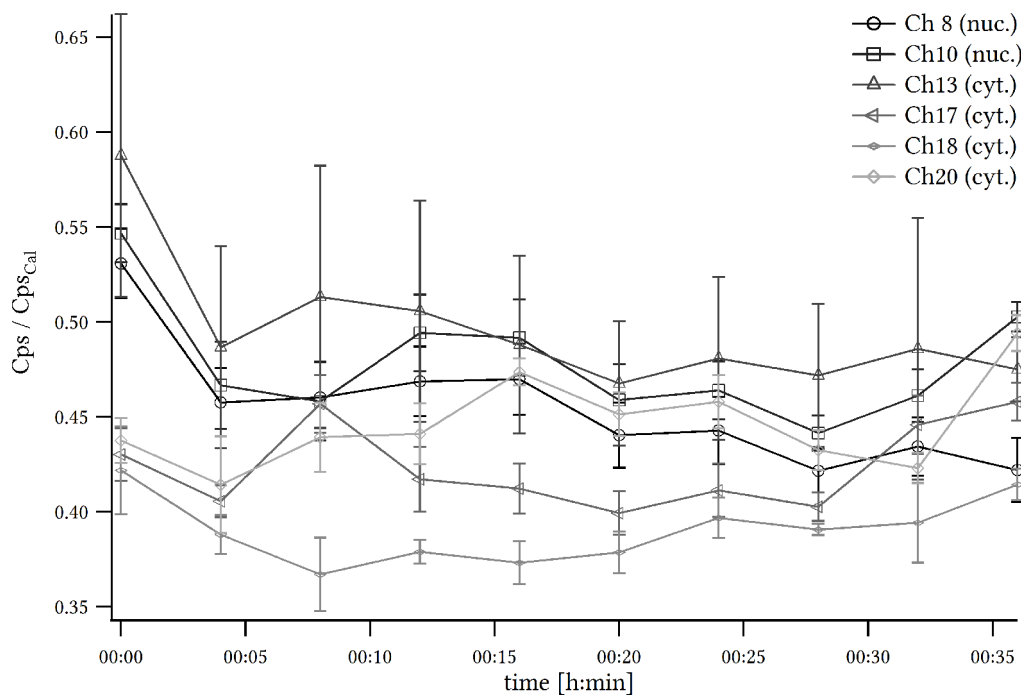
f 4.xvi: Rapamycin-induced fusion of FRB and FKBP

Several cells were observed. At each time point, three subsequent measurements of 10 s were performed with a constant laser intensity (2 mW or 6.3 mW in front of the LCoS). Between the measurements, a shutter was closed. The measurements were normalized to a calibration measurement done with Oregon Green 488 (example: f 4.viii). The normalization does not interfere with relative changes during the time sequence, but allows a comparison of the results of varying confocal volumes. Rapamycin was added directly after time point 0:00 measurements.

Examples of autocorrelation curve (f 4.xvii) and a sample sequence are shown.

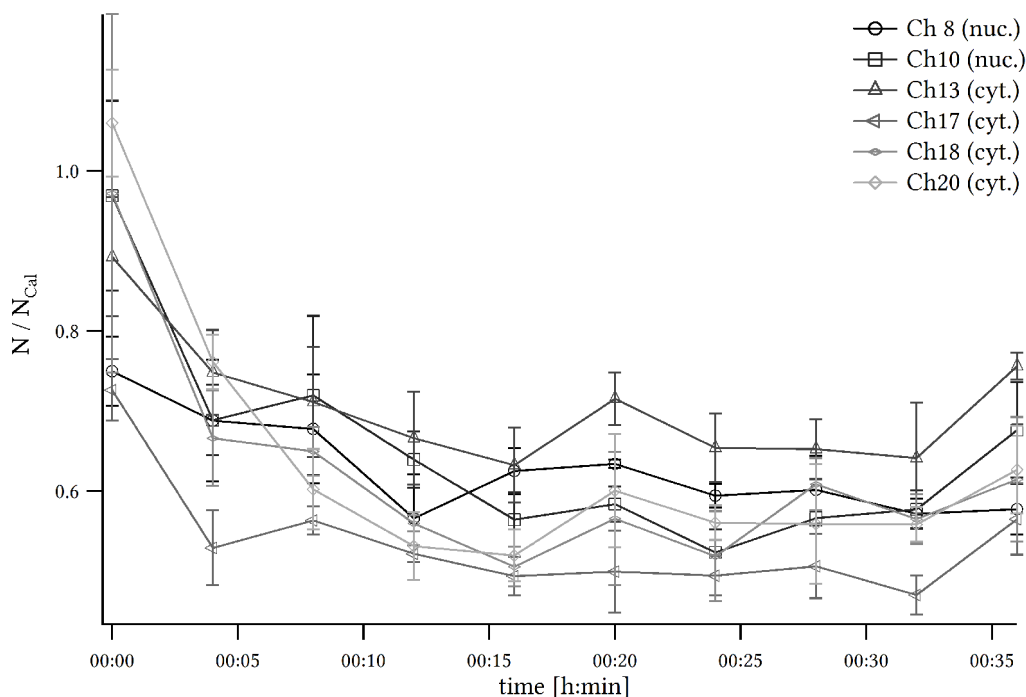


f 4.xvii: Autocorrelation and intensity trace in one of 6 channels measured in a cell before ($t = 0$) and after ($t = 32$ min) Rapamycin-induced fusion of FRB and FKBP. The number of particles decreases (amplitude of $G(\tau)$ increases) while the counts are almost equal. Measurement duration: 10 s.



f 4.xviii: Counts per second, normalized to the counts of Oregon Green 488 calibration for six channels, measured in a cell during Rapamycin-induced fusion of FRB and FKBP. Channel 8 and 10 inside the nucleus. Rapamycin addition at 0:00.

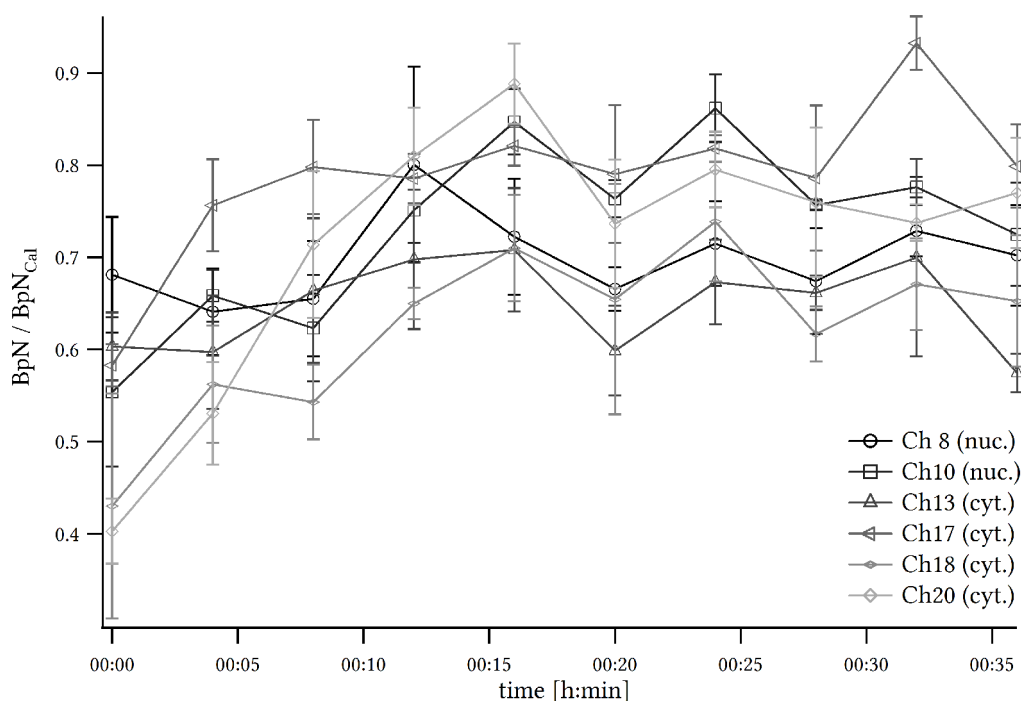
4.5. Applications



f 4.xix: Numbers of particles, normalized to the numbers of particles of Oregon Green 488 calibration for six channels, measured in a cell during Rapamycin-induced fusion of FRB and FKBP. Channel 8 and 10 inside the nucleus. Rapamycin addition at 0:00.

The photon count histogram is constant in the error range (*f 4.xviii*). The number of particles found inside the confocal volume decreases in about 15 min after addition of Rapamycin (*f 4.xvix*). The amount of dimerization varies between the cells, but was never complete. In this example, the number of particles declines to 66 ± 10 %. To calculate the absolute concentration, the normalized number of particles has to be multiplied by the concentration of the calibration dilution (about 65 Molecules/ fl).

For the same amount, the number of particles declines, the counts per particle have to increase. In this example (*f 4.xx*), the counts per particle increase to 141 ± 31 %. The error of the counts per particle is higher due to two measurement error influences.

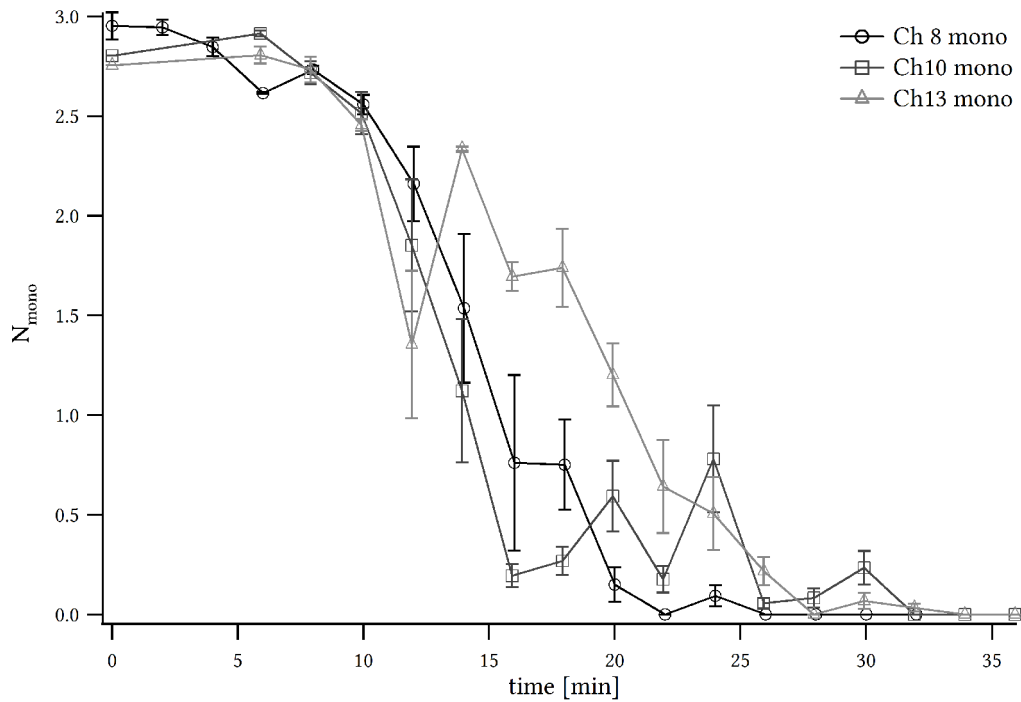


f 4.xx: Counts per particle per second, normalized to the counts per particle per second of Oregon Green 488 calibration for six channels, measured in a cell during Rapamycin-induced fusion of FRB and FKBP. Channel 8 and 10 inside the nucleus. Rapamycin addition at 0:00.

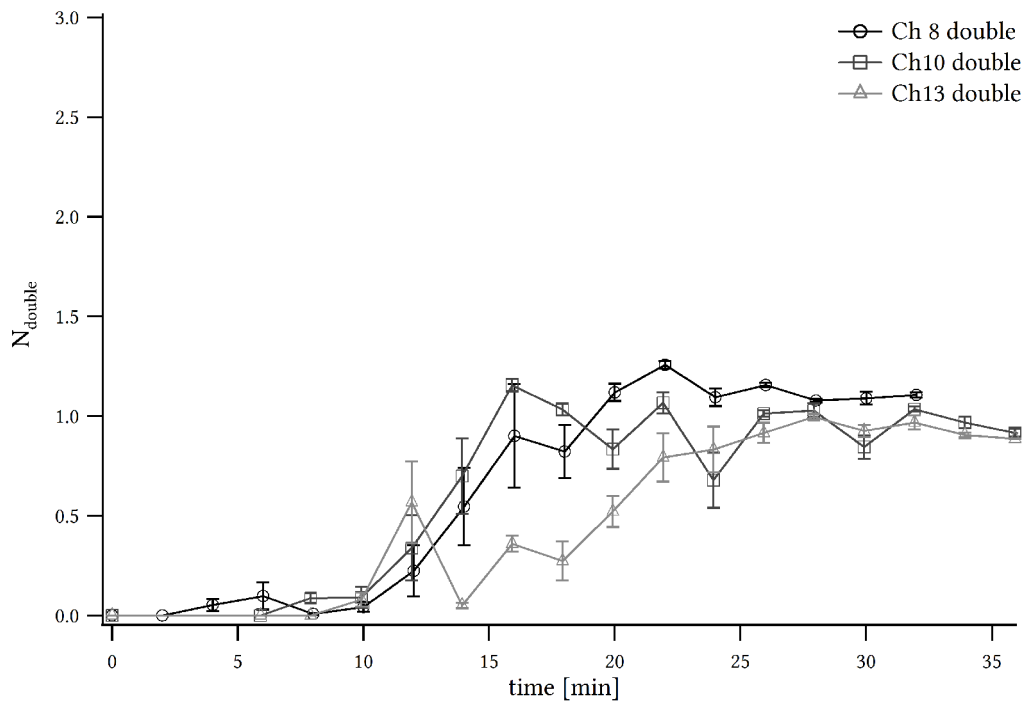
To determine the ratio of monomeric and dimerized fractions and separate the brightness per fraction, Fluorescence cumulant analysis (FCA) was performed.

FCA shows a clear reduction of monomers over the observed period (next page: *f 4.xxi*), while the number of dimers increase (next page: *f 4.xxii*). During the interval in which the concentration of monomers and dimers are changing quickly, the errors are larger as they are calculated from three measurements taken 10 seconds apart.

4.5. Applications



f 4.xxi: Number of monomers in a cell while Rapamycin-induced fusion of FRB and FKBP, determined by FCA. Three of six channels shown. Rapamycin addition at 0:00.



f 4.xxii: Number of dimers in a cell while Rapamycin-induced fusion of FRB and FKBP, determined by FCA. Three of six channels shown. Rapamycin addition at 0:00.

4.6. EGF-induced translocation and dimerization of Erk2

A well known and widely studied process inside living cells is the Membrane Associated Protein Kinase (MAPK) pathway [Seger 1995]. Until now, there is clear evidence of Erk (extracellular signal-regulated kinase) dimerization after its activation by EGF (epidermal growth factor) [Chen 2001]. Nevertheless, it is still unclear whether the dimerization is required for entering the nucleus or even more precisely where the dimerization process takes place inside the cell. Therefore, the Mek-induced activation of Erk2 provides an excellent model to be studied by SRFCs. Protocols at (*a 4.v*).

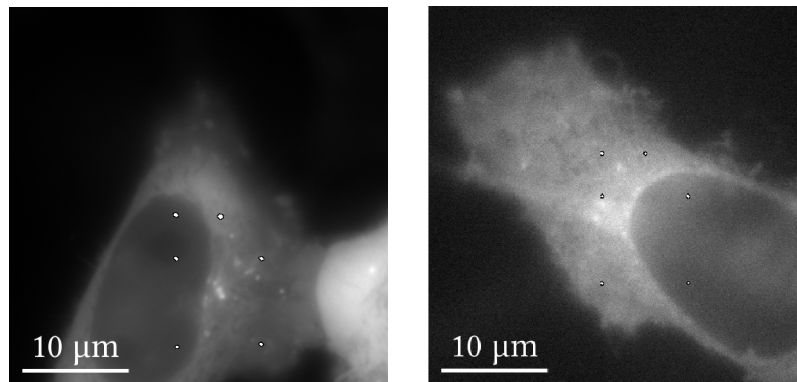
4.6.1. Wild type

Erk2, also known as MAPKKK, dimerizes after EGF-stimulation and translocates to the nucleus where it activates the cellular transcription machinery. The Epidermal Growth Factor Receptor (EGFR) is a receptor tyrosine kinase (RTK) and functions as the entry point of the stimulatory signal, caused by EGF. EGF is a mitogenic factor, which is able to activate EGFR specifically by causing dimerization of two receptor molecules in close proximity. Once the receptors are activated, the kinase domain of each EGFR molecule cross-phosphorylates the c-terminal tyrosine residues (TYR) of the corresponding receptor. Phosphorylated EGFR is able to activate multiple signaling pathways inside the cell. The MAPK (MAP kinase) pathway acts downstream EGFR and encodes for proliferative signals. After EGF-stimulation and phosphorylation of various autophosphorylation sites (TYR residues) on the c-terminal domain of the receptor, adapter proteins containing Src-homology domain 2 (SH2), e.g. Grb2, are recruited. Subsequently after recruitment of Grb2, son of sevenless (SOS) is activated and this leads to activation of Ras on the plasma membrane. Ras is a small GTP-ase, known as an oncogene, and able to activate the MAPK pathway. Upon activation, Ras undergoes a nucleotide exchange reaction, mediated by GEFs (Guanidin-nucleotide exchange factor), e.g. SOS, and GDP (Guanosin-nucleotide di-phosphate) is replaced by GTP (Guanosin-nucleotide tri-phosphate). The GTP-bound form of Ras induces translocation of a Serine/Threonine kinase (Ser/Thr kinase) Raf (MAPK) to the Ras molecule by its Ras-binding domain (RBD). Active Raf is then able to activate its downstream target Mek (MAPKK) by phosphorylation.

4.6.1. Applications

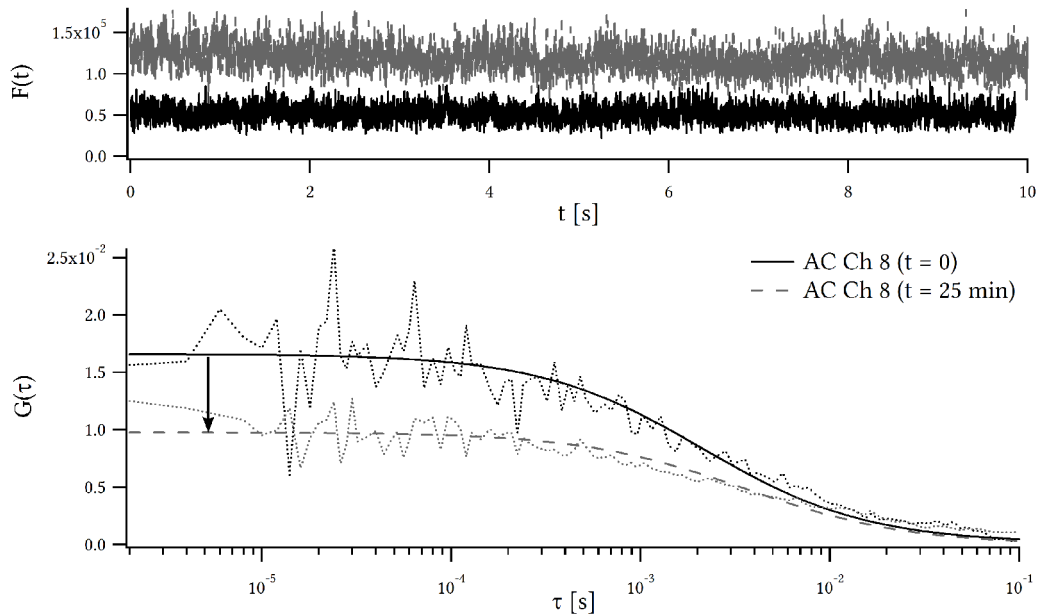
Phosphorylated Mek leads to the activation and dimerization of Erk2 (Ser/Thr kinase, MAPKKK) [Casar 2009]. Erk in its activated state is then able to enter the nuclear envelope [Chen 1992] [Costa 2006] and induces activation of the transcription machinery.

In order to observe the dimerization behavior of Erk2, HeLa cells were co-transfected with Mek-mCherry and Erk2-mCitrine. The simultaneous overexpression forces the system to respond to EGF. Therefore, cells owing high Mek and low Erk2 densities, were chosen for the measurement. The measurement volumes were partially placed in the nucleus and the cytosol, respectively.

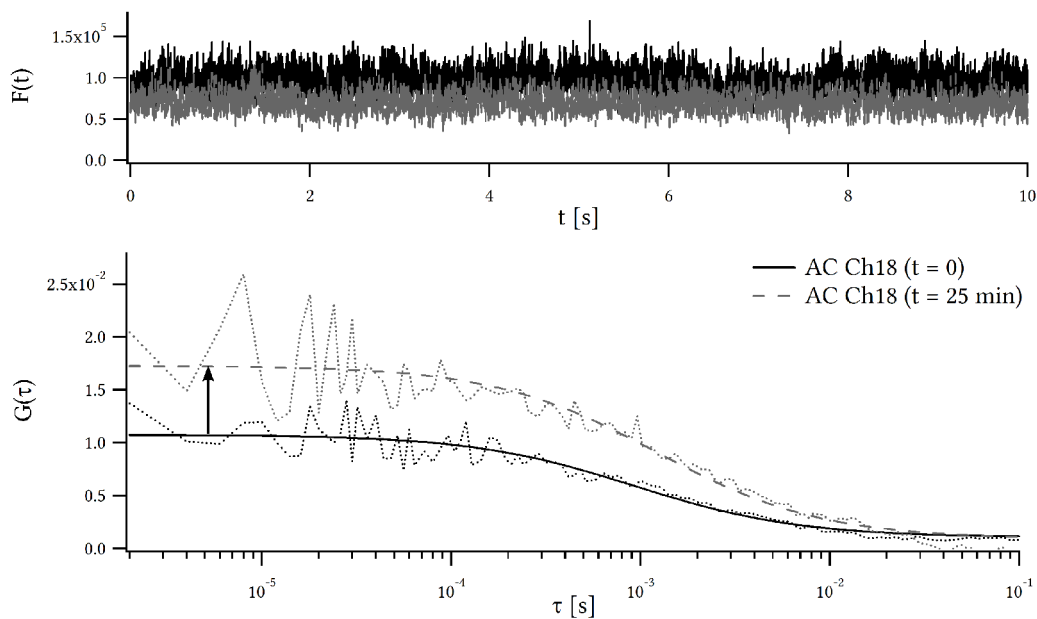


f 4.xxiii: Example of positioning of six confocal volumes in a single cell (mCherry imaged).

The positions of the confocal volumes are fixed to the fiber positions. Therefore the cells have to be positioned to the confocal volumes (*f 4.xxiii*). For any changes of the distribution, a separate calibration measurement has to be done. Several cells were observed with the same illumination distribution but with varying positions inside the cell. At each time point, three subsequent measurements of 10 s were performed with a constant laser intensity (2 mW or 6.3 mW in front of the LCoS). Between the measurements, a shutter was closed. The measurements were normalized to a calibration measurement performed with Oregon Green 488 (example: *f 4.viii*). EGF was added at time point 0:00. Examples of autocorrelation curves shown in (*f 4.xxiv*) for the nucleus and (*f 4.xxv*) for the cytosol. The analysis of a sample sequence is shown.

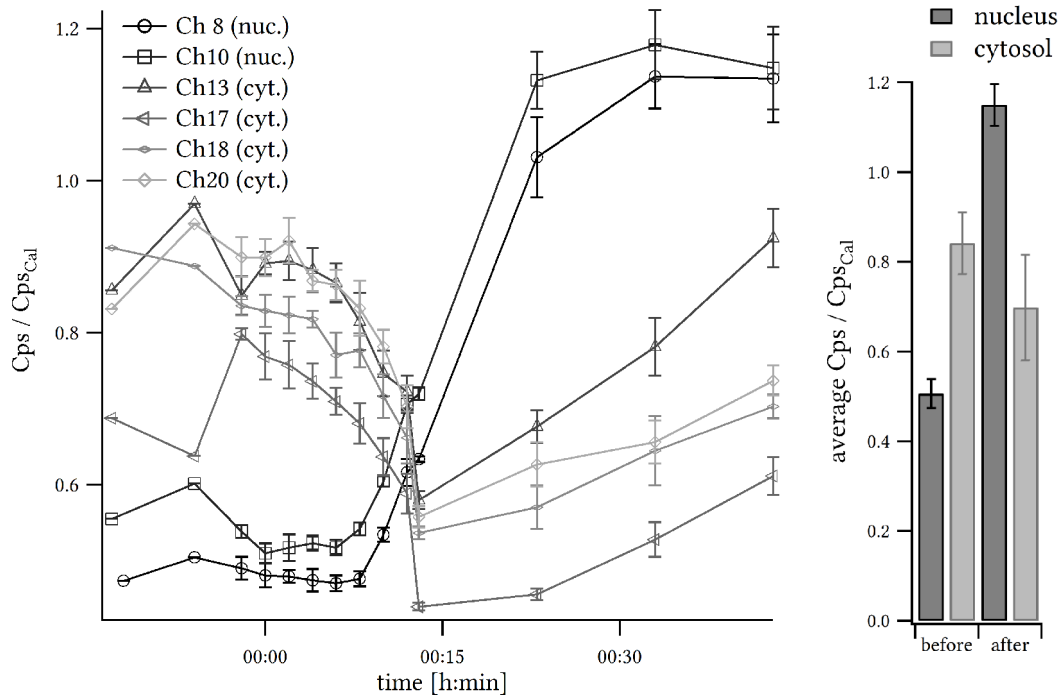


f 4.xxiv: Autocorrelation and intensity trace in one of 6 channels measured in the nucleus of a cell before ($t = 0$) and after ($t = 25$ min) EGF-induced dimerization of Erk2-mCitrine. The number of particles (amplitude of $G(\tau)$ decreases) and the counts increase. Measurement duration: 10 s.



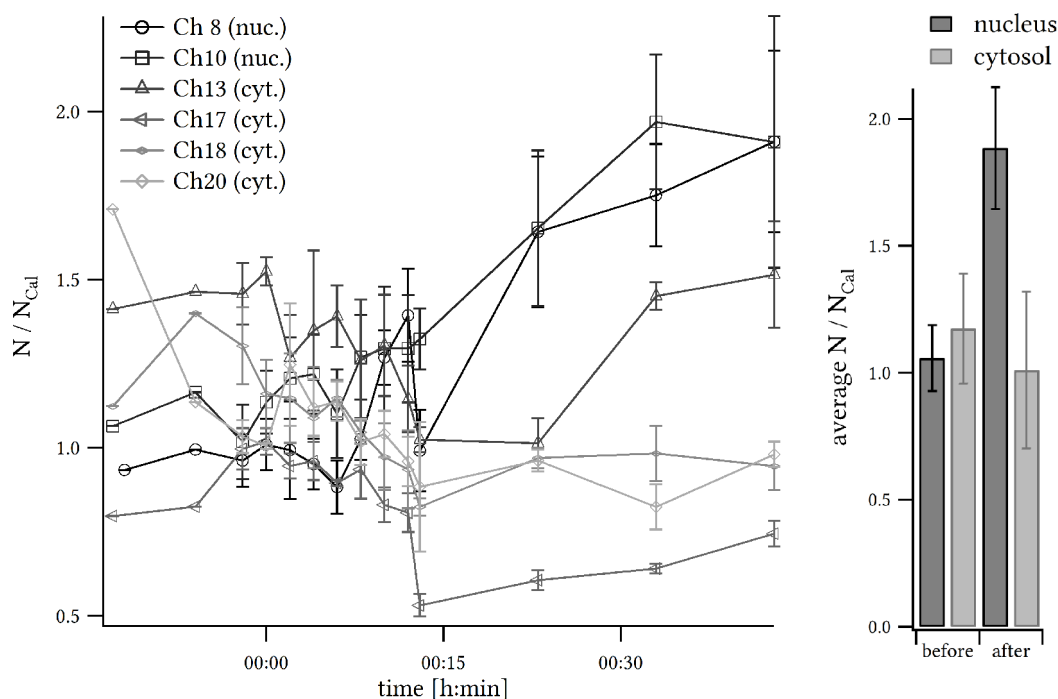
f 4.xxv: Autocorrelation and intensity trace in one of 6 channels measured in the cytosol of a cell before ($t = 0$) and after ($t = 25$ min) EGF-induced dimerization of Erk2-mCitrine. The number of particles (amplitude of $G(\tau)$ increases) and the counts decrease. Measurement duration: 10 s.

4.6.1. Applications



f 4.xxvi: Left graph: Counts per second, normalized to the counts of Oregon Green 488 calibration for six channels, measured in a cell during EGF-induced dimerization of Erk2-mCitrine. Channel 8 and 10 inside the nucleus. EGF addition at 0:00. First two measurement points are single measurements. Right graph: average Cps before and after EGF addition.

About 10 min after EGF addition, the counts inside the nucleus increase while the counts inside the cytosol decrease (*f 4.xxvi*). The counts inside the cytosol recover later on. The intensity histogram reveals a diffusion of particles from the cytosol to the nucleus. The recovery could be explained because of equalization inside the cytosol, depending on the distance from the nucleus. The concentration in the nucleus after stimulus rises above the maximum concentration inside the cytosol.



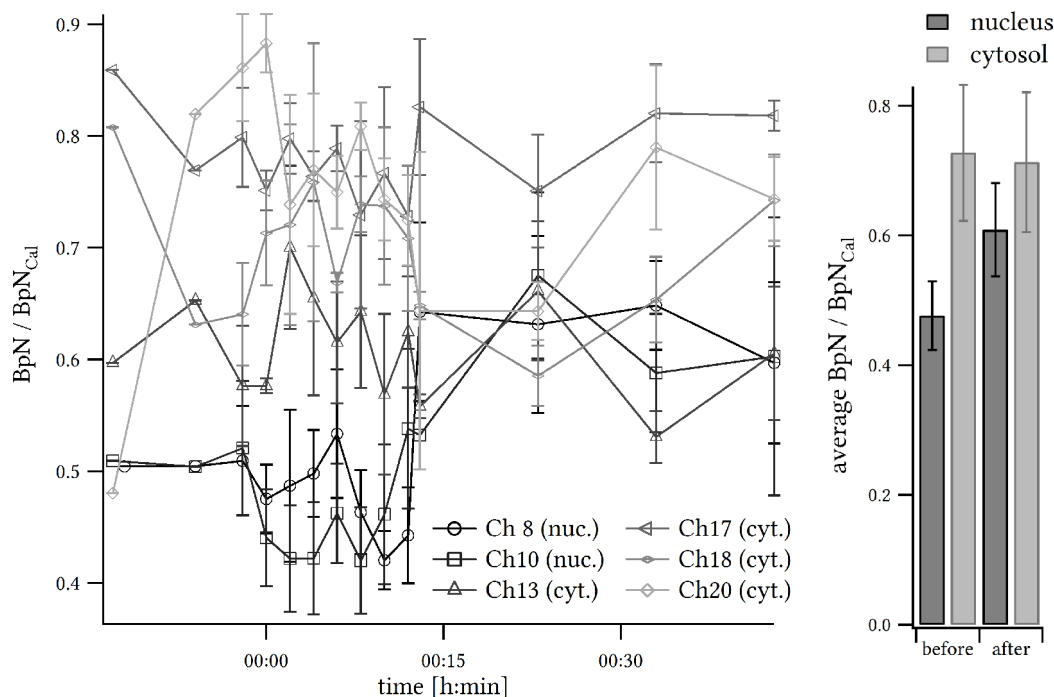
f 4.xxvii: Left graph: Numbers of particles, normalized to the numbers of particles of Oregon Green 488 calibration for six channels, measured in a cell during EGF-induced dimerization of Erk2-mCitrine. Channel 8 and 10 inside the nucleus. EGF addition at 0:00. First two measurement points are single measurements. Right graph: average N before and after EGF addition.

As the counts inside the nucleus increase to about $227 \pm 7.5 \%$, the number of particles increases to $178 \pm 18 \%$. The number of particles inside the confocal volumes outside the nucleus decreases to varying degree (*f 4.xxvii*). Channels 18 and 20 are in close proximity to the nucleus and decrease stronger than channel 13. Channel 17 is located next to the membrane and also decreases stronger than channel 13. Channel 13 shows a significant rise after 23 min, back to the initial concentration.

The total sum of particles inside all observed volumes varies about 8 %. After decreasing first, it increases after the 13 min time point, matching the increase of the total counts.

To receive the absolute concentration of molecules, the normalized number of particles has to be multiplied by the concentration of the calibration dilution (about 65 Molecules/ fl).

4.6.1. Applications

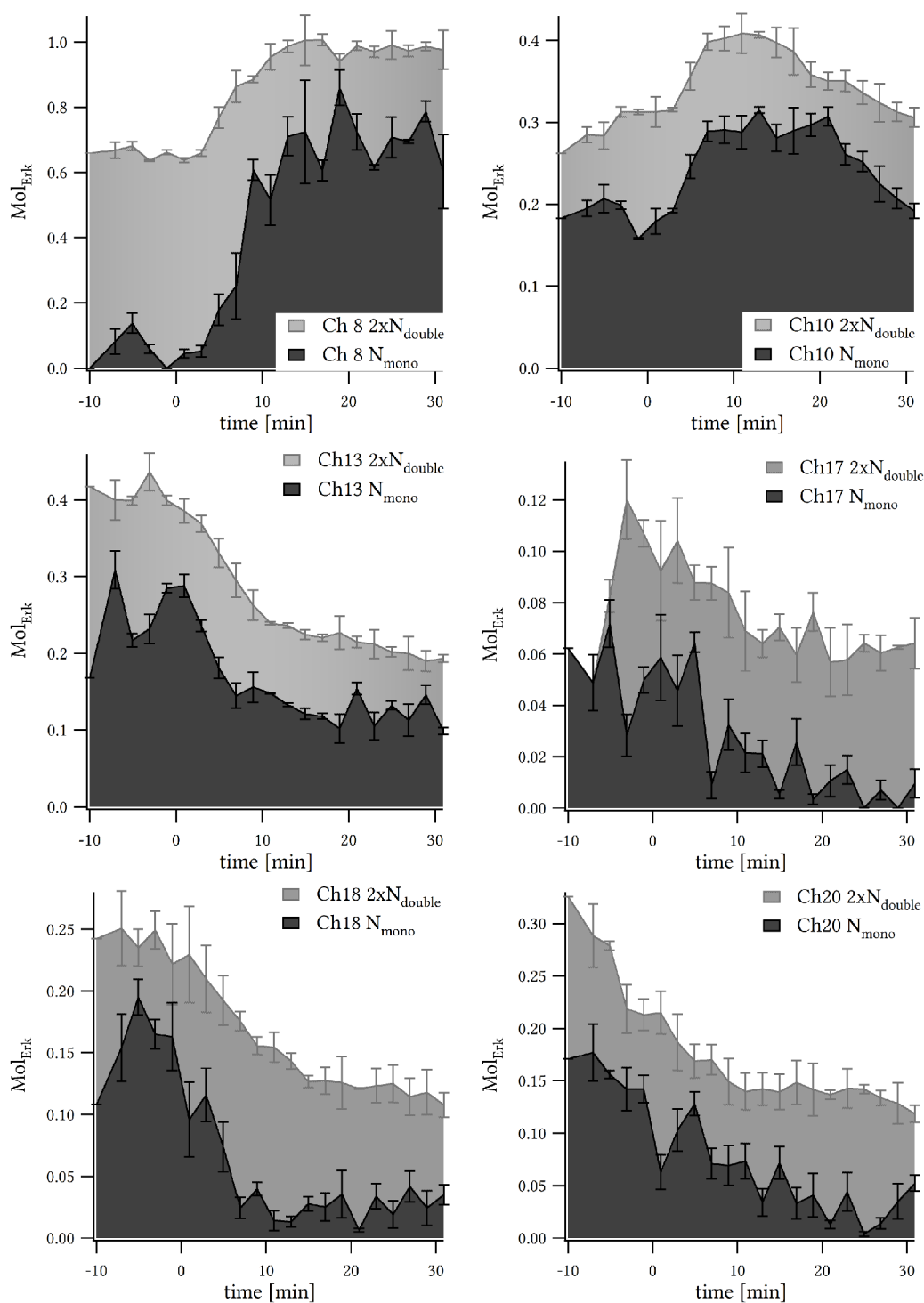


f 4.xxviii: Left graph: Counts per particle per second, normalized to the counts per particle per second of Oregon Green 488 calibration for six channels, measured in a cell during EGF-induced dimerization of Erk2-mCitrine. Channel 8 and 10 inside the nucleus. EGF addition at 0:00. First two measurement points are single measurements. Right graph: average BpN before and after EGF addition.

The counts per particle plot shows a significant increase to 128 ± 16 % of counts per particle inside the nucleus after EGF addition (*f 4.xxviii*). The normalization implies a constantly high count rate per particle in the cytosol.

Although the shown example illustrates the expected behavior of accumulation of dimers in the nucleus, it can not separate the fractions of monomers and dimers in the cytosol and the nucleus. Therefore FCA was applied.

f 4.xxix shows an increasing number of particles in the nucleus and a decrease in the cytosol, as expected. The allocation of the fractions suggests an increase in monomers in the nucleus and a decrease of monomers in the cytosol, while the number of dimers is stable or even decreasing in the nucleus.

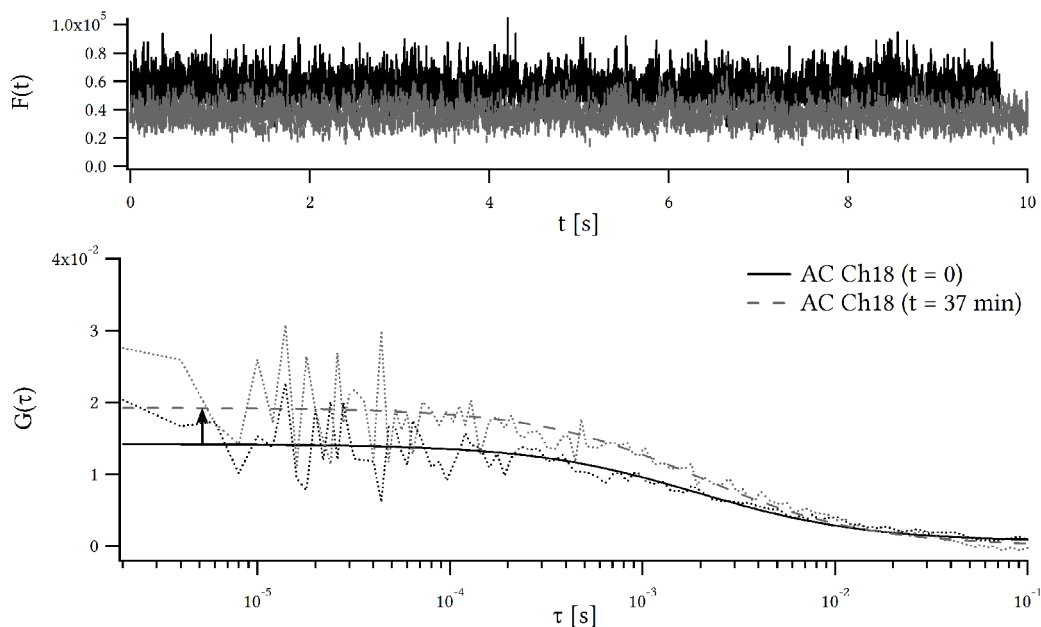


f 4.xxix: Total number of Erk2-mCitrine molecules, monomers and dimers (with two Erk2-mCitrine molecules) determined by FCA in a cell while EGF-induced dimerization of Erk2-mCitrine. Channel 8 and 10 inside the nucleus. EGF addition at 0:00.

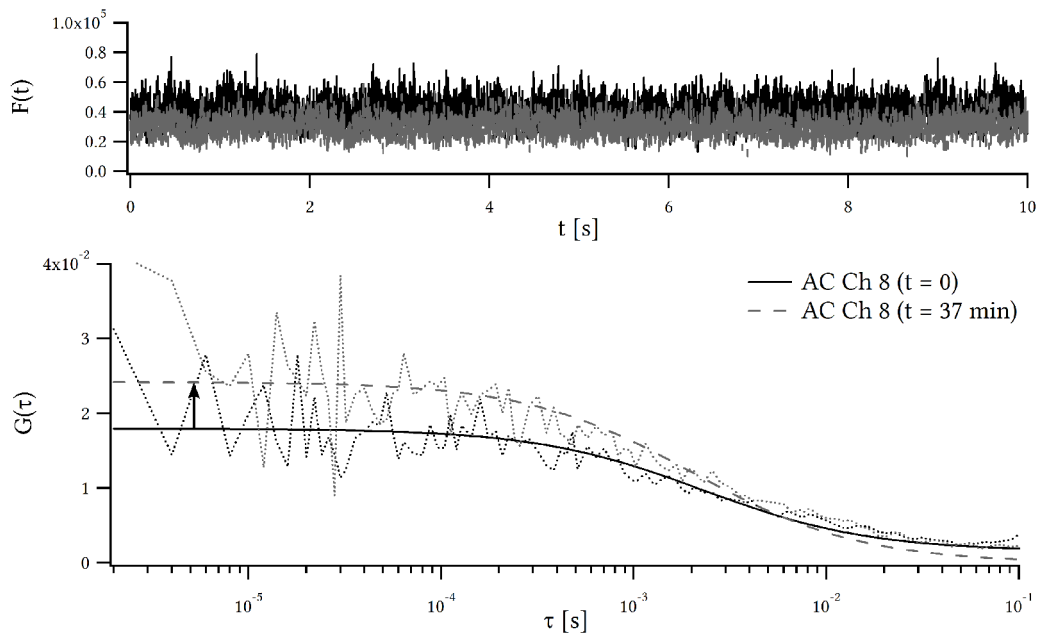
4.6.2. Applications

4.6.2. Inhibition of the Mek-Erk2 interaction

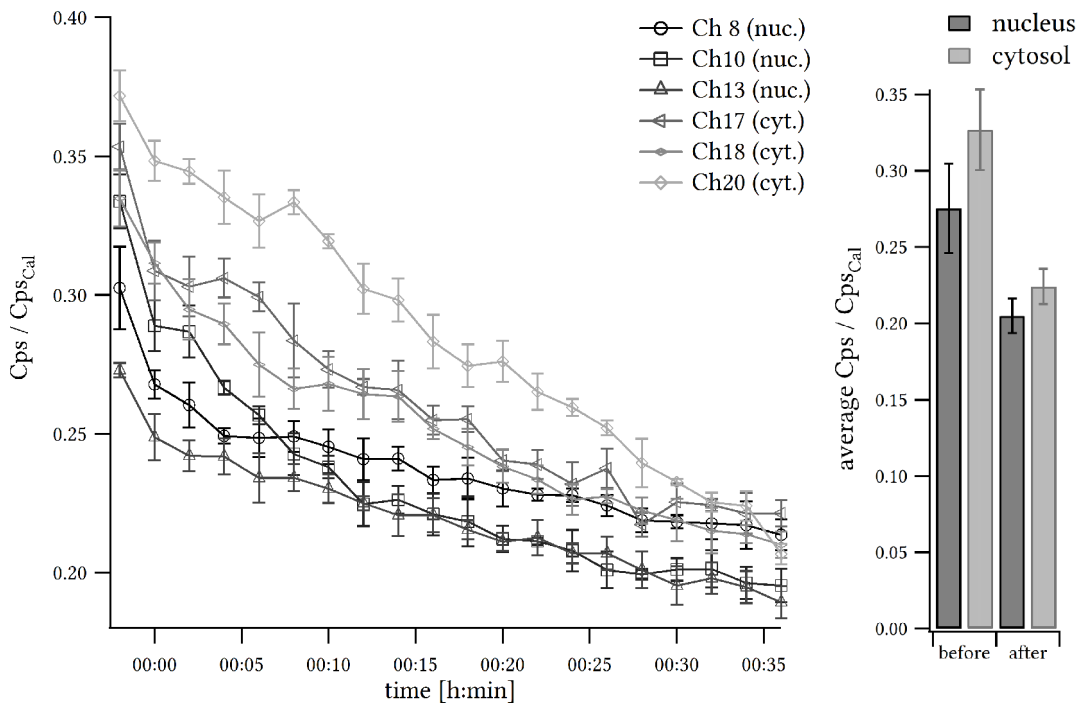
The phosphorylation of Erk2 can be reduced by inhibiting Mek using small molecule inhibitors. Such an inhibitor is UO126 [Favata 1998], a specific Mek inhibitor which prevents the binding of Erk2 to Mek and therefore disrupts the formation of Erk2 dimers. Cells co-transfected with Mek-mCherry and Erk2-mCitrine, inhibited with UO126, were used as a negative control. 10 μ M UO126 were incubated 30 min prior to EGF-stimulation in order to prevent activation of the MAPK pathway. Examples of autocorrelation curves shown in (*f 4.xxx*) for the nucleus and (*f 4.xxxi*) for the cytosol. A sample sequence is shown afterwards.



f 4.xxx: Autocorrelation and intensity trace in one of 6 channels measured in the nucleus of a cell before ($t = 0$) and after ($t = 37$ min) EGF-induced dimerization of Erk2-mCitrine after inhibition. The number of particles (amplitude of $G(\tau)$ increases) and the counts decrease because of bleaching. Measurement duration: 10 s.



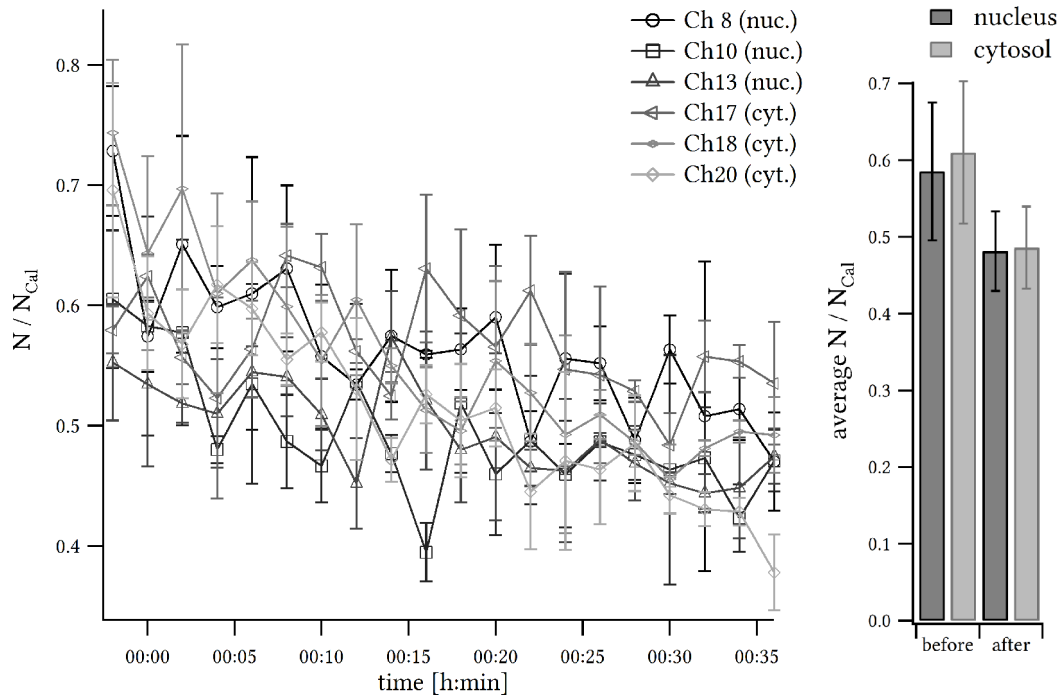
f 4.xxxi: Autocorrelation and intensity trace in one of 6 channels measured in the cytosol of a cell before ($t = 0$) and after ($t = 37$ min) EGF-induced dimerization of Erk2-mCitrine after inhibition. The number of particles (amplitude of $G(\tau)$ increases) and the counts decrease because of bleaching. Measurement duration: 10 s.



f 4.xxxii: Left graph: Counts per second, normalized to the counts of Oregon Green 488 calibration for six channels, measured in a cell during EGF-induced dimerization of Erk2-mCitrine after inhibition. Channel 8, 10 and 13 inside the nucleus. EGF addition at 0:00. Right graph: average Cps before and after EGF addition.

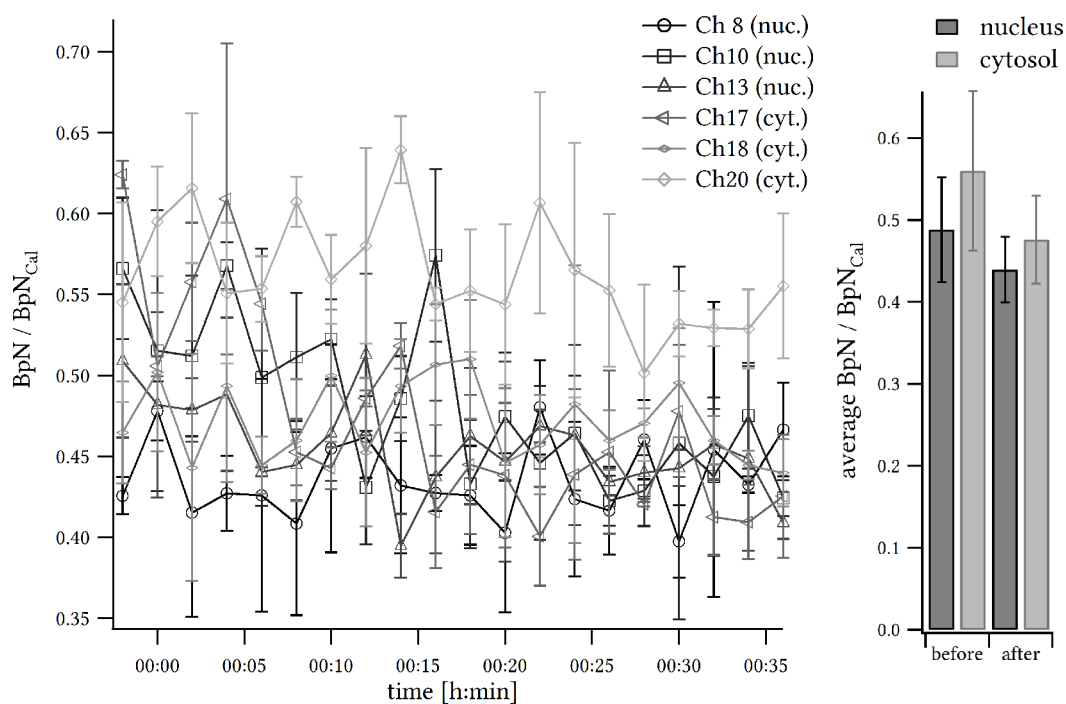
4.6.2. Applications

The fluorophores inside the confocal volumes of all channels bleach about the same rate. No influence of the EGF addition is observable (*f 4.xxxi*).



f 4.xxxiii: Left graph: Numbers of particles, normalized to the numbers of particles of Oregon Green 488 calibration for six channels, measured in a cell during EGF-induced dimerization of Erk2-mCitrine after inhibition. Channel 8, 10 and 13 inside the nucleus. EGF addition at 0:00. Right graph: average N/N_{Cal} before and after EGF addition.

The trace of the number of particles behaves proportional to the measured counting histograms. The number of particles reduces slowly due to bleaching (*f 4.xxxii*). There are no visible differences between the channels inside the nucleus and the cytosol.

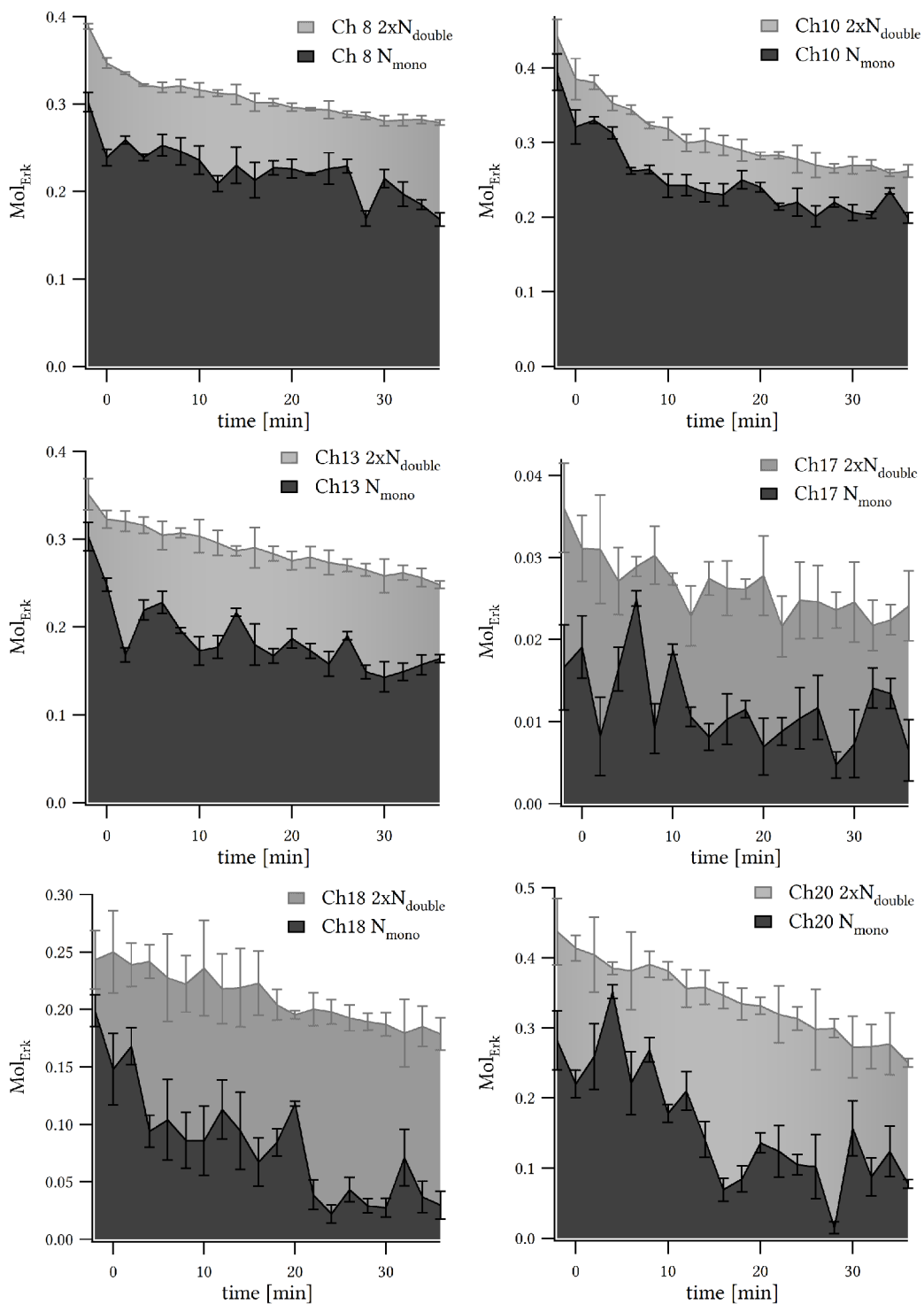


f 4.xxxiv: Left graph: Counts per particle per second, normalized to the counts per particle per second of Oregon Green 488 calibration for six channels, measured in a cell during EGF-induced dimerization of Erk2-*mCitrine* after inhibition. Channel 8, 10 and 13 inside the nucleus. EGF addition at 0:00. Right graph: average BpN before and after EGF addition.

The counts per particle are constant in the range of error (*f 4.xxxiv*).

FCA confirm the slow decrease of the number of molecules, equally of monomers and dimers in all channels (next page: *f 4.xxxv*).

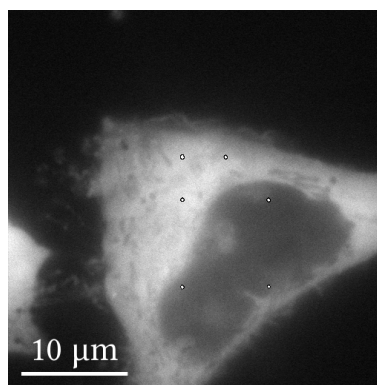
4.6.2. Applications



f 4.xxxv: Total number of Erk2-mCitrine molecules, monomers and dimers (with two Erk2-mCitrine molecules) determined by FCA in a cell while EGF-induced dimerization of Erk2-mCitrine after inhibition. Channel 8, 10 and 13 inside the nucleus. EGF addition at 0:00.

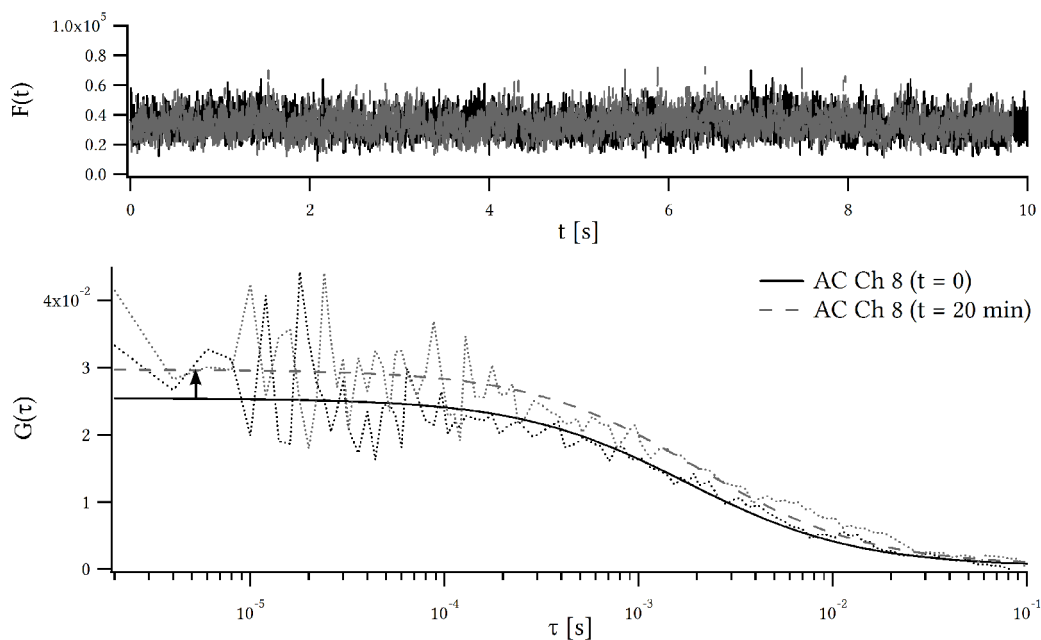
4.6.3. Erk2(K52R) kinase-deficient mutant

Erk2(K52R)-mCitrine is a mutant of Erk2(wt) and was used as an additional control. Erk2(K52R) has been described to be kinase-dead, creating a nonproductive binding mode with ATP (Adenosin-5'-tri-phosphate) and is therefore unable to phosphorylate downstream substrates [Robinson 1996]. The mutation is not sufficient to suppress the dimerization nor the enrichment in the nucleus. This might be caused by the phosphorylation state of Erk2, which was shown to be responsible for its nuclear translocation instead of its kinase activity [Khokhlachev 1998]. Examples of autocorrelation curves shown in (*f 4.xxxvii*) for the nucleus and (*f 4.xxxviii*) for the cytosol. Positions in the cell shown in (*f 4.xxxvi*). The entire example sequence is shown afterwards.

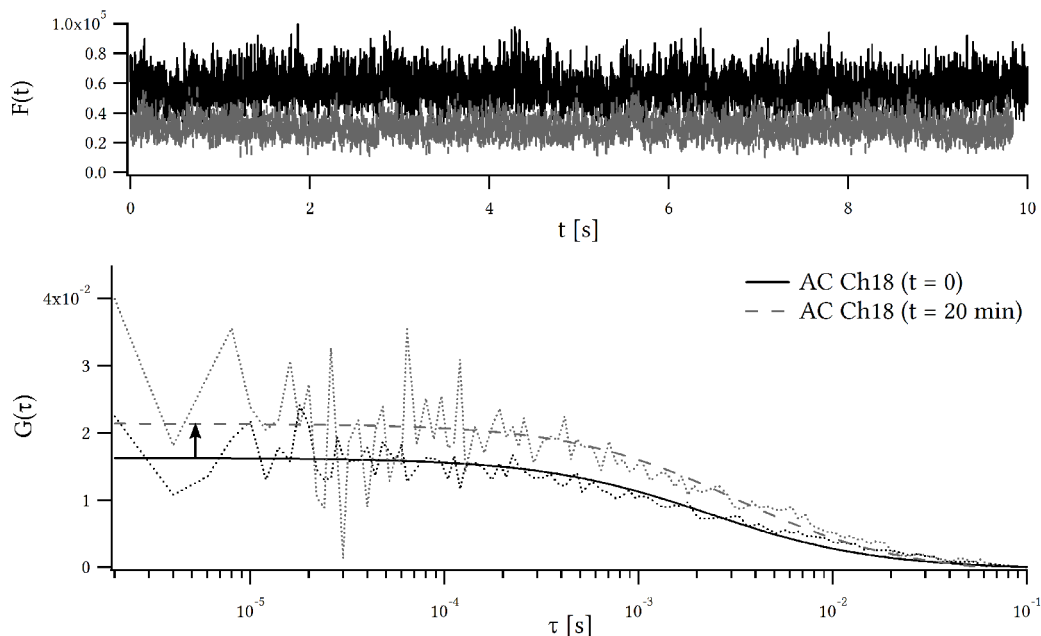


f 4.xxxvi: Position of the six confocal volumes (mCherry imaged).

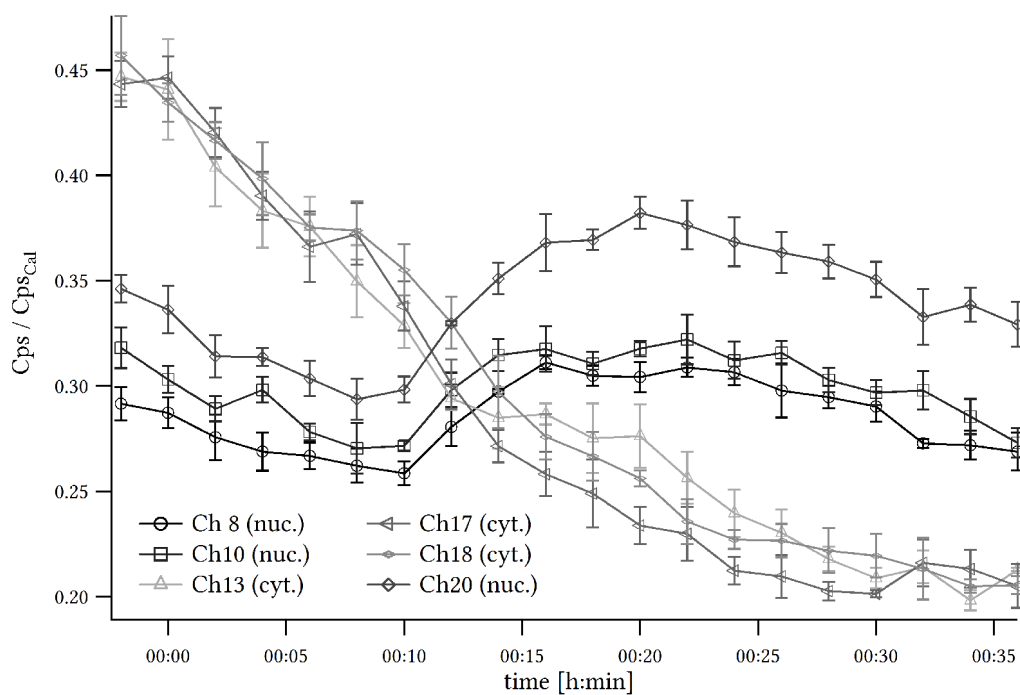
4.6.3. Applications



f 4.xxxvii: Autocorrelation and intensity trace in one of 6 channels measured in the nucleus of a cell before ($t = 0$) and after ($t = 20$ min) EGF-induced dimerization of Erk2(K52R)-mCitrine. The number of particles decreases (amplitude of $G(\tau)$ increases) while the counts are equal. Therefore the counts per molecule increase. Measurement duration: 10 s.



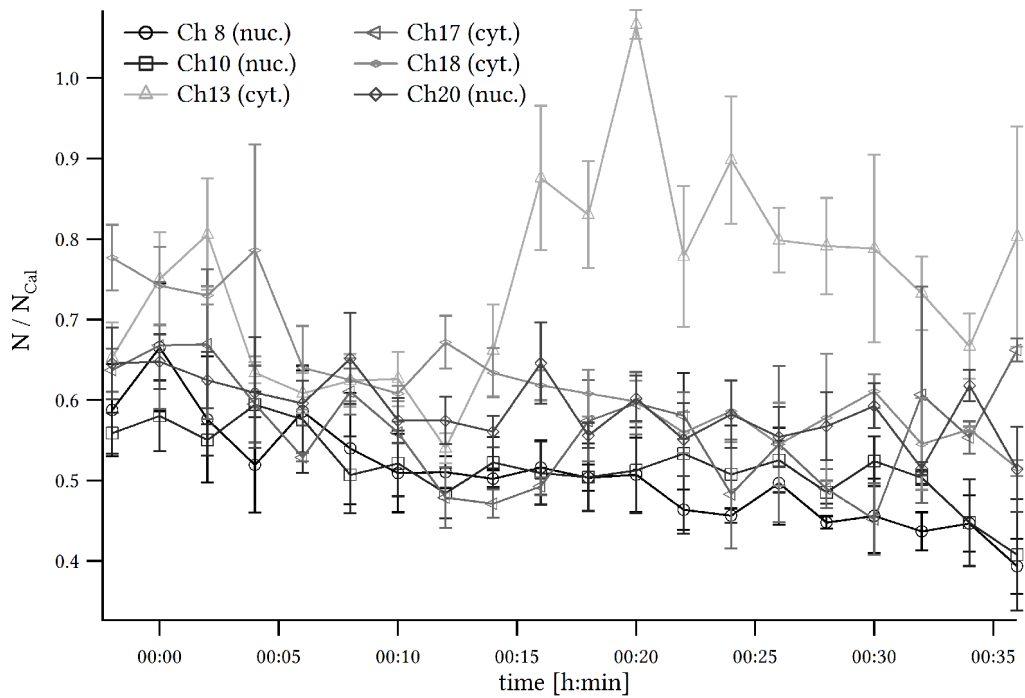
a 4.xxxviii: Autocorrelation and intensity trace in one of 6 channels measured in the cytosol of a cell before ($t = 0$) and after ($t = 20$ min) EGF-induced dimerization of Erk2(K52R)-mCitrine. The number of particles (amplitude of $G(\tau)$ increases) and the counts decrease. Measurement duration: 10 s.



f 4.xxxix: Counts per second, normalized to the counts of Oregon Green 488 calibration for six channels, measured in a cell during EGF-induced dimerization of Erk2(K52R)-mCitrine. Channel 8, 10 and 20 inside the nucleus. EGF addition at 0:00.

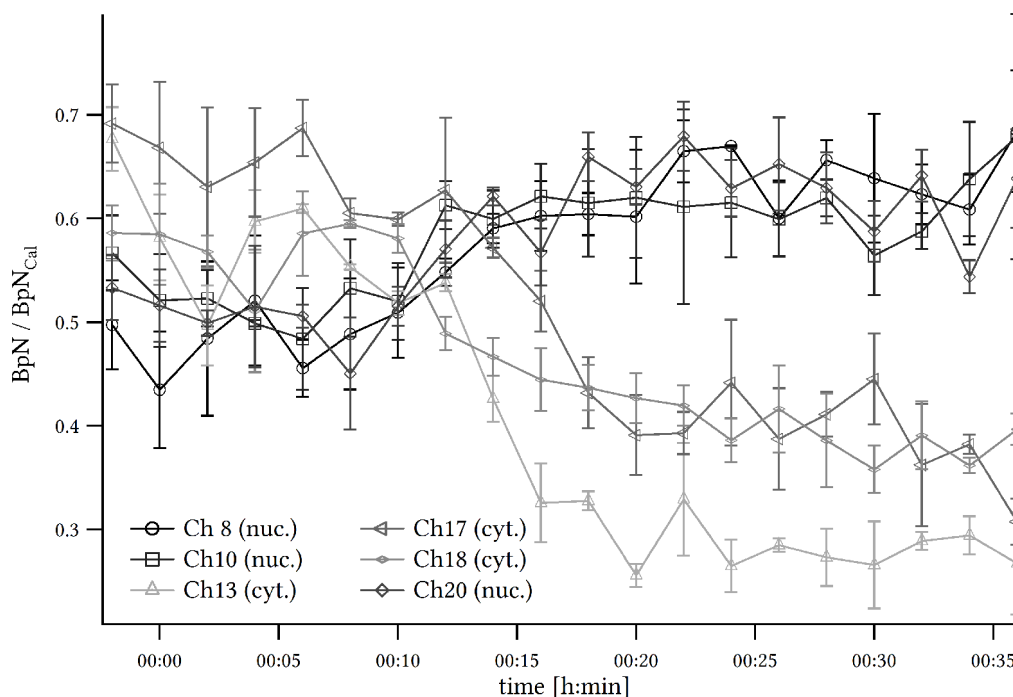
The intensity histogram shows an increase of the counts inside the nucleus relative to the counts in the cytosol 10 min after stimulation (*f 4.xxxix*), comparable to the wild type (*f 4.xxvi*). Bleaching reduces the slope of the absolute increase of counts in the nucleus.

4.6.3. Applications



f 4.xl: Numbers of particles, normalized to the numbers of particles of Oregon Green 488 calibration for six channels, measured in a cell during EGF-induced dimerization of Erk2(K52R)-mCitrine. Channel 8, 10 and 20 inside the nucleus. EGF addition at 0:00.

The number of particles histogram decreases slowly (*f 4.xl*). Channel 13 increases rapidly at about 15 min after stimulation and stabilize at a higher number of particles.



f 4.xli: Counts per particle per second, normalized to the counts per particle per second of Oregon Green 488 calibration for six channels, measured in a cell during EGF-induced dimerization of Erk2(K52R)-mCitrine. Channel 8, 10 and 20 inside the nucleus. EGF addition at 0:00.

The graphs of the counts per particle show an increase in the nucleus and a decrease in the cytosol (*f 4.xli*). This could probably happen because of ab initio oligomerized and later on diffusion into the nucleus, partially bleached fluorophores, fluorophores in the triplet state or another photochemical degeneration, reducing the quantum efficiency or increasing the duration in the excited state.

Although the particles inside the cytosol show decreasing counts per molecule, the particles inside the nucleus clearly show an increase of counts per particles, indicating a dimerization.

5. Discussion

Fluorescence Correlation Spectroscopy (FCS) enables the quantification of the absolute concentrations and the diffusion coefficient of low concentrations of fluorescent molecules in cells, with low impact on the observed sample. Fluorescence Cumulant Analysis (FCA) determines the absolute concentration and brightness per particle. Both methods evaluate the fluctuations produced by excited and emitting molecules crossing a small illuminated volume inside the sample and can therefore be applied to the same time binned photon data. The highest sensitivity are achievable with small confocal volumes and fast and highly quantum efficient single photon detectors, e.g. avalanche photon diodes (APD). The absence of the spatial resolution by a single confocal volume can be solved by scanning over the sample, reducing the lateral time resolution. Reducing the scanning to a few spots, the lateral time resolution can be preserved by switching faster than the fluctuations observed. However, the fluctuations would be sampled coarse grained yielding lower statistical significance. In this work, we have developed a parallel FCS system, that allows measuring up to 16 confocal volumes simultaneously, increasing the spatial and temporal resolution of the FCS technique. It can observe multiple cellular compartments without any loss of information compared to a non scanning, single confocal FCS. To achieve the parallel illumination, the laser beam is split by a phase modulating Liquid Crystal on Silicon device (LCoS) into the appropriate number of

beams with the full width of an equivalent single confocal illumination beam. The illumination is automatically aligned to a solid array of 16 fibers, which serve as pinholes.

The design required an extensive implementation of hardware (*chapter 5.1.1*) and software (*chapter 5.1.2*). It provides a robust and automated system for parallelized measuring of FCS. Measurements performed with this system are reproducible and the conditions are suitable for cellular measurements as shown in *chapter 4*.

The sensitivity of FCS strongly depends on the size of the observed confocal volume. To achieve a small volume, the optical system has to be aligned precisely and a collimated and expanded beam should fit the back aperture of the focusing objective. The pinholes have to be positioned precisely in the image plane of the excitation path. The volumes achieved in this system were about 1 fl. The size is not diffraction limited but suitable for FCS measurements. The size is strongly influenced by the size of the pinholes [Rigler 1993], as will be further discussed in *chapter 5.1.1*.

Additionally to the normal alignment of a confocal microscope, the position of the LCoS has to fit and its image plane has to be in the back focal plane of the objective. Otherwise the illumination volume is not optimal. These steps are to be aligned manually and the result can vary. The fiber array position is fixed to the image plane of the excitation path within the limits of production variance. Although this produces robustness and simplification, commercial systems like the Zeiss 510 scan the pinhole position to correct for aberrations.

The LCoS as an adaptive optical device is not only used to split the illumination in up to 16 confocal spots, but for automated calibration of the illumination system relative to a camera or a point detector array. At the same time, it corrects for some aberrations and misalignment. For this, it utilizes scanning sequences with single spot or with line illumination. These methods are fast and universal for varying detector dimensions, e.g. varying fiber arrays with different geometries, aperture or transmission wavelength ranges.

All corrections yielded by the LCoS are done under the aim to fit best the excitation path. In case of an optimally aligned excitation path, the illumination will be optimized. As soon as the fiber array is not parallel to the image plane, the optimization will still fit the excitation volume to the detection volume, as demanded by FCS. But the illumination beam will not reach the diffraction limit.

The system was successfully tested in various samples composed of living cells, measuring diffusion inside the cytosol and the nucleus, respectively. Typically up to 6 confocal volumes were used. A compromise for the brightness of the cells is essential. In case of long measurement series, the bleaching of the whole cell could hinder the analysis and demand a reduction of the number of intervals or of the confocal volumes. Bright cells with a high number of particles reduce the slope of bleaching, but can quickly overflow the photon correlator card capacities. A lower number of volumes increase the dynamic range of the system, e.g. allows observation of brighter cells in the range of FCS. A higher number of volumes was only used in low concentrations of fluorophores in dilutions. Cells would probably either bleach too much or the counts would overflow the photon correlator card.

The possibility to observe multiple confocal volumes in a single cell allows observations of the flow and dimerization over parts of a cell without time shift and reducing the time resolution between intervals. It could facilitate resolving the dynamics of spatio-temporal proteins (e.g. recycling, degradation), observing active and passive transport (e.g. proteins, cargo) or receptor distribution in living cells after stimulation/inhibition. But it also points out influences which could be misinterpreted while scanning a cell, e.g. fluctuation of laser intensity or vibrations that would simultaneously influence all measured volumes temporarily. In spite of the difference between varying confocal volumes, it is still possible to compare the results because of calibration measurements. These are needed, not only to compensate the illumination distribution created by the LCoS, but aberrations common for objectives crossed with varying angles of incidence, occurring in any scanning microscope. However, for FCA this procedure still needs to be improved with more testing samples to correct for effects not accounted in the theory. In the application shown here, the calibrations were performed with a dilution of known fluorophores in water. The actual focusing of multiple spots in a nonuniform compartment as a cell could require a compromise and induce a source of error for any comparison. To overcome this limitation, a calibration inside each cell, e.g. with a known diffusion rate of a free diffusing fluorophore, could be used. The absorption spectrum of this fluorophore would have to be the same as the observed fluorophore, to exclude aberrations caused by varying wavelengths, and have a different emission spectrum, introducing aberrations in the excitation path, or a distinguishable diffusion rate.

The intensity of the ghost traps observed decreases with the number of aligned spots (compare *f 3.ix* and *f 4.xiii*). During measurements, they are usually outside the observed cell.

5.1. Implementation

The implementation of the system fulfills the design requirements. To achieve this, it exhausts the existing hardware (*chapter 5.1.1*). The software implemented optimize the illumination and improves the rate of photons processable up to exhausting the possibilities of 32-bit computer systems (*chapter 5.1.2*).

5.1.1. Hardware

The optics and hardware is chosen to be suitable for the visible range of light. The Olympus IX 81 assured the accessibility needed and 40x water (NA 1.2) and oil (NA 1.3) and the 60x oil (NA 1.35) objectives produce suitable confocal illumination volumes. The measurement volume is given by the convolution of illumination volume and the detection volume. The detection volume is produced by the pinhole size and the optics of the emission path. The fiber core diameter of the implemented fiber array is fixed at 105 μm . For best results, it should typically have a size of 1 AU (Airy disk Unit) [Conchello 2005]. The Airy disk is the center region of the diffraction pattern behind a collimated illuminated pinhole. The diameter depends on the wavelength λ , the numerical aperture NA of the focusing objective and the total magnification M of the emission path (objective and optical system):

$$d_{AU} = \frac{1.22\lambda}{NA} M \quad (\text{e 5.i})$$

For 488 nm, a 60x oil objective with NA 1.35 and with further internal magnifications set to 1 (switchable between 1 and 1.6), this results in a optimal pinhole size of about 27.5 μm . In most systems, the pinhole can be adapted to the wavelength. In this system, the fiber array would have to be replaced. The larger size of the pinholes (3.82 times of optimum) cause a strong dependency of the measurement volume on the size of the illumination volume. It increases the collected scattered light and reduces the signal to noise ratio. As a benefit, the high fiber core diameter operate for different wavelengths and objectives without cutting of illuminated and exciting volume. Although the size of the pinholes could be adapted by additional lenses, this would destabilize the emission path and the alignment.

The quality of FCS measurements is strongly dependent on the signal to noise ratio, while the output is the fluctuation of the signal. Apart from limitations due to the fluorophores inside the cell, the measurable intensities are limited by the photon counts processable per second by the counting card. The photon counting and correlator card DPC-230 of Becker & Hickl GmbH has a comparable small memory for 16 detection channels (buffer for 4×10^6 counts) and a slower PCI connection instead of a PCI express connection. As a result, high count rates processable by the detectors can overflow the card memory in a few seconds. The signal, composed from the intensity and number of fluctuations measured, is limited. The noise of the signal is produced by many varying factors, e.g. stray light or photochemical reactions of the fluorophores. A high impact to noise is produced by the background noise of the detector. The APDs implemented have a noise signal of 250 to 400 counts/ s for the six best APDs usually used for the measurements and 1300 to 3000 counts/ s for the remaining APDs.

5.1.2. Software

Most parts of the software is written in layers and modules, easy to change in parts or used for further developments. As it is, the most upper layer improves the usability for specific usages, calling and handling the main software parts. These main layer are standalone working scripts, using the a basic bunch of modules to handle the camera, the photon correlator card, the LCoS and the filter wheel. The LCoS module has two layers. The lower layer creates the pattern per spot and the layer above sums up those patterns and the background correction. This layer could be expand to use more sophisticated methods to reduce the number of ghost dots and perhaps the quality of the focus of each spot.

Increasing the number of spots increases the complexity of the phase modulation and the produced stray light. Most stray light is blocked with the centered light. But the intensity distribution to the single confocal volumes varies, even while changing pattern with the same number of spots, changing the sizes of the confocal volumes. Therefore the calibration of the confocal volumes have to be determined for any chosen illumination setting separately. The ghost dots could produce additional photo bleaching. But most visible ghost dots are far outside of the observed cell.

The main software issue limiting the capabilities of the system or future updates is given by the 32-bit operating Windows system of the computer. Because of the limitations of 32-bit

5.1.2. Discussion

systems, only 4 GB of working memory (RAM) can be addressed directly. Moreover only 2 GB are accessible per process. These limits can be overcome partly, allowing a single process to access up to 3 GB. Still, the software is written in LabVIEW which needs continuous memory for working tables of data. As it is, using RAM with other software can fragment it into small discontinuous parts, forcing the user to restart the computer. To overcome this issue a 64-bit system would be preferable, running a 64-bit LabVIEW Version and corresponding hardware drivers. In the current state, the RAM of the photon correlator card is used at the edge of capabilities, saving the data in fragments in maximal possible speed to the RAM of the computer, which process the data to save them in a binary raw file on the disk. Although the processing is already minimized by combining the data fragments of a single measurement interval (~ 10 s of measurement), this step could be further reduced to an additional saving in between and combining the data later on at the expense of additional hard disk communication and complex data management. Even if a gain in RAM capacities of the computer could be achieved, the RAM of the photon correlator card and the read out speed can not be improved (*chapter 5.1.1*).

5.1.3. Applications

After calibration, the SRFCs was first tested on well known systems. First, a series of monomeric and dimeric transfected cells were observed (*chapter 4.4*). Single measurements, in contrast to measurement sequences, suffer less from bleaching effects. In addition, with shorter and not continuous measurement durations, higher photon count rates are processable. A series of 981 measurements in monomeric and 1129 in dimeric transfected cells yielded a brightness ratio of 1.48 ± 0.41 (based on standard deviations).

To test a dimerization process, Rapamycin-induced dimerization of FRB and FKBP (*chapter 4.5*) was measured. The measurements typically showed a dimerization process during about 15 min after Rapamycin addition. The autocorrelations of the shown example before and after the process are clearly separated, while the detected intensity is almost steady (*f 4.xvii*). The increase in counts per particles per second (BnP) by a factor of 1.41 ± 0.31 exclude a misinterpretation due to bleaching effects (*f 4.xx*). FCA confirm the observations and showed an increase of dimers at the expense of monomers. However, it was not possible to separate the brightness for the different channels (*chapter 7.3*). Of all experiments, these showed the highest

impact of photon counting capacity limitations. Because of the small size of the molecules, the transfected cells tended to have high concentrations of fluorophores. Only relatively dark cells or a reduced number of confocal volumes (e.g. four worked well) did not overflow the memory of the photon correlator card. During the long measurement sequences with 6 confocal volumes, many cells bleached too much and the intervals between the measurement repetitions had to be increased.

To test the SRFCs on a complex biological problem, EGF-induced dimerization of Erk2 (*chapter 4.6.1*) was observed. The results show clear evidence of translocation to the nucleus and an increase of brightness per particle indicates an increase of dimers in the nucleus. In contrast, the FCA results indicate an accumulating of monomers in the nucleus. An analysis of the distance dependency from the confocal volume to the nucleus would be the continuation of the experiment. Because of the time consuming measurement sequences, four to six cells can be measured on one day. The inhibition of the Mek-Erk2 interaction suppressed the localization and dimerization (*chapter 4.6.2*).

Erk2(K52R) kinase-deficient mutant was chosen as an additional test (*chapter 4.6.3*). The cells showed comparable translocation and dimerization effects as the wild type experiment (*chapter 4.6.1*). The selected example shows problems repeatedly occurred during long-term measurement sequences. The intensity graphs (*f 4.xxxix*) show high bleaching, which complicate the analysis. This problem occurred repeatedly and is caused by the high total light intensity the cell is exposed to. The bleaching can be reduced by reducing the number of measurements (reducing time resolution or length of sequence), the illumination intensity (reducing signal to noise ratio) or the number of measured volumes (while adjusting the illumination correspondingly). In (*f 4.xl*), Channel 13 increases rapidly at the same time point, the intensities in (*f 4.xxxix*) inside the nucleus and in the cytosol are in balance. FCS measurements can be affected by many sources, e.g. the cell can move, the optics drift or a neighboring cell can die, spreading free diffusing fluorophores as a second diffusing species (not covered by the applied diffusion fit). To exclude such influences from the interpretation of the analysis, multiple cells were measured. Drift or free diffusing fluorophores in the sample plane would probably influence all confocal volumes. The usage of multiple parallel measured volumes inside a single cell can help excluding some sources of errors. Still, other influences, e.g. an air bubble in the oil between objective and glass slide, remain.

5.2. Outlook

There are several updates to the system for further development. It might be beneficial to improve the counting capacities to be able to measure brighter cells (*chapter 5.2.1*) or to bypass the limitation at the expense of time resolution and implement sequential measurements (*chapter 5.2.2*). The usefulness for the observation of biological systems would strongly improve by the implementation of Fluorescence Cross-Correlation Spectroscopy (*chapter 5.2.3*) and by automation of the multi point FCS analysis (*chapter 5.2.5*). Furthermore an improvement of the size of the confocal volumes should be aimed (*chapter 5.2.4*).

5.2.1. Increasing maximal number of processed photon counts per second

For any attempt to increase the limit of processable photon counts considerably, an update of hardware and software are inevitable. The communication to the photon correlator card has not much potential for improvement. A replacement of the photon correlator card would need profound changes or replacement of the photon correlator card software modules. To improve the computer software, an update to 64-bit would be required, including updates to 64-bit LabVIEW and associated drivers. Another possibility to overcome capacity limitations of commercial counting systems is to use separate counting cards and processing on multiple computer in parallel.

Duration of implementation about 3-4 months after delivery.

5.2.2. Sequently measurement of different groups of confocal volumes

The number of confocal volumes illuminated and detected in parallel is limited because of bleaching and the counting capacity of the hardware. Although it is possible to use all 16 confocal volumes in parallel, the total illumination intensity bleaches too much weak transfected cells with a small pool of fluorophores. Higher concentrations of fluorophores, in the range of cells used for fewer confocal volumes and capable of reducing the bleaching effects, transmit too many photons to count. The illumination intensity can not be reduced without reducing the signal to noise ratio, while a high concentration already reduces the fluctuation signal.

It is possible to bypass these limitations by sequently measuring different groups of the confocal volumes. While measuring one group, the rest should neither be illuminated, nor the signals of the corresponding APDs counted. This would reduce the achievable time resolution between two measurement intervals and only the measurements part of a fraction would be measured parallel. The refreshing rate of the LCoS (60 Hz) is not fast enough to switch the illumination to multiple fractions in a rate above the observed fluorophore diffusion induced fluctuations. The total bleaching of the cells would increase in comparison with a measurement using less volumes and breaks without illumination, but stronger transfected cells, within the FCS measuring range, could be measured.

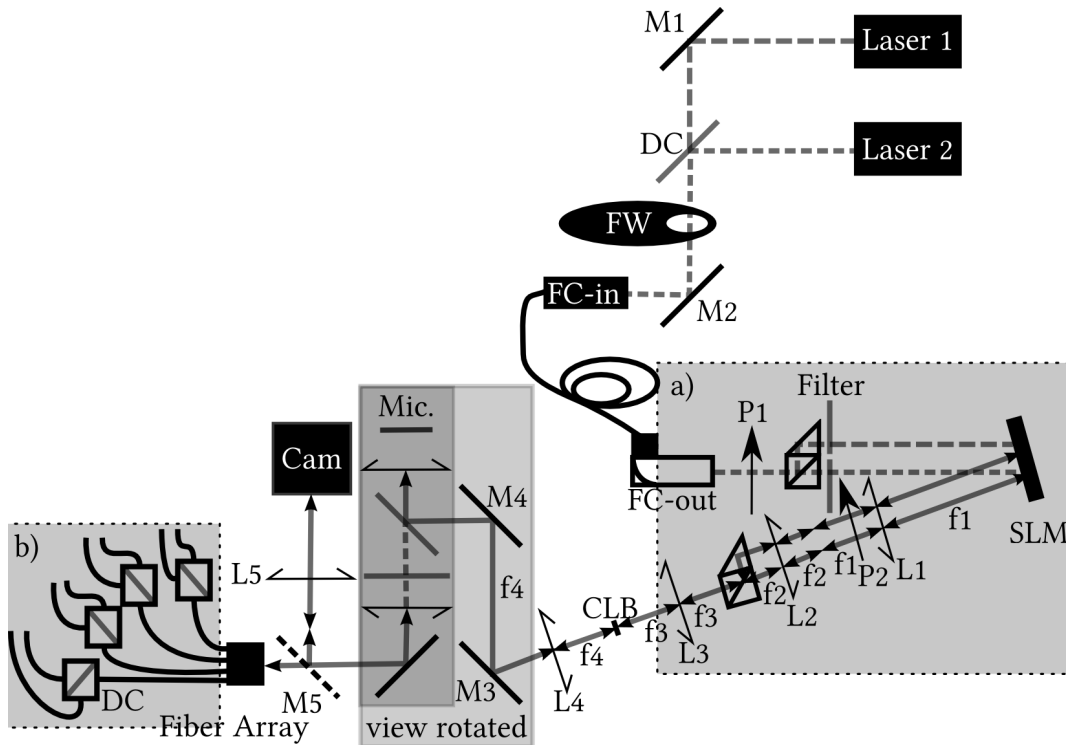
To implement subsequent measurements, no hardware alterations are required. The software modules have to start in a sequence to align the light to a fraction of the fibers, activate the corresponding photon correlator card connections and start a measurement. Then, the software should stop the measurement, align the light to the next fraction, deactivate the previous and activate the new photon correlator card connections and start the next measurements. The implementation would only need an additional control module, reusing existing modules.

Duration of implementation about two weeks.

5.2.3. Discussion

5.2.3. Fluorescence Cross-Correlation Spectroscopy (FCCS)

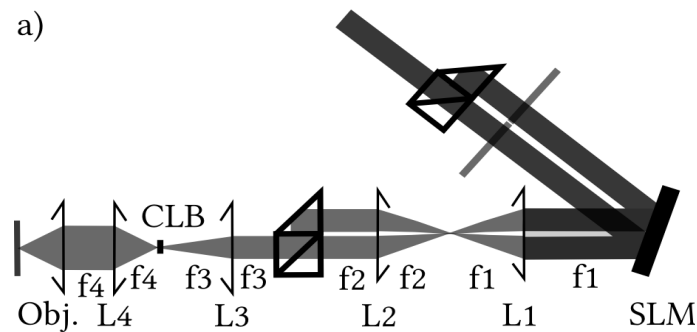
For many biological questions, an update of the system to FCCS would be needed. Although it is not implemented, the design of the system supports the update. Some preparations and tests are done.



f 5.i: Optical system for FCCS, with changes in the illumination system a) (f 5.ii) and the detection b) (option).

<i>M1 and M2</i>	<i>mirrors for coupling into fiber.</i>
<i>FW</i>	<i>filter wheel with a selection of neutral density filters and a light blocker.</i>
<i>FC-in</i>	<i>fiber coupler input.</i>
<i>FC-out</i>	<i>achromatic fiber coupler output.</i>
<i>P1 and P2</i>	<i>polarizer.</i>
<i>Filter</i>	<i>band pass filter.</i>
<i>SLM</i>	<i>spatial light modulator, a LCoS.</i>
<i>L1, L2, L3, L4</i>	<i>lenses – telescopes with focal lengths f_1, f_2, f_3, f_4.</i>
<i>CLB</i>	<i>center light blocker.</i>
<i>M3 and M4</i>	<i>mirrors for coupling into microscope.</i>
<i>Obj.</i>	<i>Objective.</i>
<i>M5</i>	<i>switchable mirror in dual-port C-mount adaptor.</i>
<i>L5</i>	<i>focus lens for camera.</i>
<i>DC</i>	<i>dichroic mirror.</i>

On the illumination path, two lasers would be coupled into the fiber, using a dichroid filter (DC). Behind the fiber out coupler, a beam splitting cube and a prism could be attached to each other and shifted to create two parallel beam paths (*f 5.i*). Filters will select one wavelength per beam path and both beams would hit the SLM on different parts of the device. Each part would have different maximum gray color (c_{max}), as it is needed for different wavelength. This was tested positively using one wavelength, but changing parts of the pattern outside of the beam path with higher and lower maximum gray level than suitable for the selected wavelength. The center of the pattern can be changed in the software, passing the new position on to the lowest layer of the software. Behind the SLM, four instead of two lenses would be necessary.



f 5.ii: Two color illumination system with 4 lenses and two combined beam splitting cubes and prisms.

After the first two lenses, in the image plane, a second set of beam splitting cube and prism would combine both beams again (*f 5.ii*). The lenses and the image plane are required for the same reasons, it is needed at the back focal plane: the position should not shift while the SLM introduce a deflection of the beam. If corrections for the beam path length are needed, they could be included to the SLM patterns. Both halves of the SLM could be calibrated separately, but one calibration used with different maximum gray color, probably would fit both. Adapting the number of total elements (c_{total}) for both pattern, the number and size of the phase steps of the SLM, and therefore the influence, would be the same for both beams. It is to be tested, if the aberrations of the lenses, the beam combiner and the objective allows using one calibration.

Another theoretical solution for the illumination is using the system with a pair of wavelengths, whose corresponding phase shifts induced by the Hamamatsu LCoS are multiple of 2π . As an advantage, only a single beam path would be sufficient. For the specific attached

5.2.3. Discussion

device, such couples could be found from 400/620 to 430/700 for 2π and 4π slope respectively. Any other pattern for two varying wavelengths aligning both wavelength would create intense ghost dots and probably create an additional cone of diffusive aligned light around the confocal volume due to the false fraction of the pattern.

For the detection, two options are given. Behind the microscope, the fiber array act as pinholes for both wavelengths. The excitation light can be split using fiber coupled beam splitting benches available, e.g. from Thorlabs. The fiber ports are too big to use one dichroic for all fibers.

Aside from the wavelength separation, a time separation can be achieved if pulsed lasers are used for interleaved excitation. Both laser emit sequently laser pulses with pauses in length above the live time of the fluorophores in the excited state. Because the LCoS cannot switch fast enough, separated illumination pattern would still be needed. The time separation reduces the data obtained per color by a factor of 2.

The fibers would be connected to the photon correlator card and from the measured photon counts, the cross correlation could be calculated. For pulsed interleaved excitation, the separation of the counts have to be brought forward to the correlation calculations.

Duration of implementation about 6 month.

5.2.4. Improvement of the shape of the confocal volumes

The size and the shape of the confocal volume do not only influence the signal to noise ratio of the measurement, but directly the measured parameters. The separated calibration measurements per volume with a known dilution adjust these parameters for aberrations, but they do not correct them.

Some aberrations of the illumination path, e.g. aberrations resulting in a lateral shift of the volumes, are automatically corrected by the position calibration. Most other aberrations in the illumination path could probably be corrected by the direct search and stimulated annealing approach to a certain degree, but would be time consuming. Further development in the pattern generation would improve the confocal volumes by reducing the aberrations introduced by the SLM. A more sophisticated pattern generation, as investigated for optical tweezers [Leonardo 2007], could improve shape, size, illumination intensity distribution and would reduce ghost dots based on software modification. These changes only require changes

in a single module, as long as the combination and superposition of the patterns is linear.

Though the position calibration corrects the illumination path to solve the illumination positions and sophisticated pattern generation can reduce aberrations introduced by the SLM, it can not reduce the impact of imprecisely positioned optical elements on the phase front of the laser and the achievable minimum volume size. Further protocols for alignment, which is mostly comparable to a standard FCS system, could improve the system performance.

An extensive aberration correction for the objective and the sample is described in [Leroux 2011], including both, illumination and detection path into the spatial light modulation. To include the excitation paths, a deformable mirror-surface device (DMD) is used because of the low loss of light. For the presented SRFCS approach, a DMD would not be suitable for beam splitting. But the aberration correction approach, including a Shack-Hartmann wavefront sensor, could also be used to characterize and then correct the illumination path, excluding the excitation path for the sample measurements.

The detection path is designed for robustness and stable measurements. The easiest and most robust way to reduce the detection volumes would be a replacement of the fiber array, which would take less than half an hour for implementation and no software modifications. To correct the pinhole sizes, apart from replacing the fiber array, additional lens optics could be included, but destabilize the emission path and complicate an optimal alignment.

To facilitate the alignment of the whole optical path and introduce the possibility to align the system manually to a fiber and absolute photon counts without LCoS introduced deflections, a single, in x and y positionable fiber replacement for the fiber array can be implemented. If this would be combined with a preferable motorized correction of the fiber array position in z , the z correction introduced by the LCoS could scan for the optimal illumination path.

5.2.5. Discussion

5.2.5. Analysis software

Multiple parallel measurements produce a multiple number of data. The analysis of high numbers of autocorrelation curves and the calibration to a known fluorophore dilution should be further automated. The analysis of a single cell down to time sequence graphs takes too long to achieve good statistics in a reasonable time. A graphical user interface providing a preview of the autocorrelation curves and the option to exclude bad measurements before proceeding would be an option to overcome the problems of an automated verification.

In addition to the possibility to join sequently, continuous measurements, an average should be provided. The verification of fitted data, the identification of parameters for a new fit and the variable number of accepted fits per time point complicate an automation.

Furthermore, a software could visualize the two dimensional diffusion and concentration history in three dimensional graphs (two dimensions plus color code).

6. References

- Abbe 1873 E. Abbe, Abbe Beiträge zur Theorie des Mikroskops und der mikroskopischen Wahrnehmung, Archiv für Mikroskopische Anatomie 9 (1), 1873, 413-468
- Ambrose 1956 E. J. Ambrose, A surface contact microscope for the study of cell movements, Nature 178, 1956, 1194
- Axelrod 1976 D. Axelrod, D. Koppel, J. Schlessinger, E. Elson, W. Webb, Mobility measurement by analysis of fluorescence photobleaching recovery kinetics, Biophysical Journal, 16 (9), 1976, 1055-69
- Bacia 2003 K. Bacia, P. Schuille, A dynamic view of cellular processes by in vivo fluorescence auto- and cross-correlation spectroscopy, Methods, 29, 2003, 74-85
- Belisle 2008 J. M. Bélisle, J. P. C., P. W. Wiseman, T. E. Kennedy, S. Costantino, Patterning protein concentration using laser-assisted adsorption by photobleaching, LAPAP, Lab Chip, 8, 12, Dec. 2008, 2164-2167
- Belisle 2009 J. M. Belisle, D. Kunik, S. Costantino, Rapid multicomponent optical protein patterning, Lab Chip, 9, 2009, 3580-3585
- Betzig 2006 E. Betzig, G. H. Patterson, R. Sougrat, O. W. Lindwasser, S. Olenych, J. S. Bonifacino, M. W. Davidson, J. Lippincott-Schwartz, H. F. Hess , Imaging Intracellular Fluorescent Proteins at Nanometer Resolution, Science, Vol. 313, Sep. 2006

6. References

- Blancquaert 2008 Y. Blancquaert, J. Gao, J. Derouard, A. Delon, Spatial fluorescence cross-correlation spectroscopy by means of a spatial light modulator, *J. Biophotonics*, Vol. 1, No.5, 2008, 408-418
- Capoulade 2011 J. Capoulade, M. Wachsmuth, L. Hufnagel, M. Knop, Quantitative fluorescence imaging of protein diffusion and interaction in living cells, *Nature Biotechnology*, Aug. 2011
- Casar 2009 B. Casar, A. Pinto, P. Crespo, ERK dimers and scaffold proteins: unexpected partners for a forgotten (cytoplasmic) task, *Cell Cycle*, 8, 7, Apr. 2009, 1007-1013
- Chen 1992 R. H. Chen, C. Sarnecki, J. Blenis, Nuclear localization and regulation of ERK- and RSK-encoded protein kinases. *Mol Cell Biol*, 12, 3, 1992, 915-27
- Chen 1995 J. Chen, X.-F. Zheng, E. J. Brown, S. L. Schreiber, Identification of an 11-kDa FKBP12-rapamycin-binding domain within the 289-kDa FKBP12-rapamycin-associated protein and characterization of a critical serine residue, *Proc. Natl. Acad. Sci. USA*, Vol. 92, May 1995, 4947-4951
- Chen 1999 Y. Chen, J. D. Müller, P. T. C. So, E. Gratton, The photon counting histogram in fluorescence fluctuation spectroscopy, *Biophysical Journal*, Vol. 77, Jul. 1999, 553-567
- Chen 2001 Z. Chen Z., T. B. Gibson, F. Robinson, L. Silvestro, G. Pearson, B. Xu., A. Wright, C. Vanderbilt, M. H. Cobb, MAP kinases, *Chem. Rev.*, 101, 8, 2001, 2449-2476
- Colyer 2010 R. A. Colyer, G. Scalia, I. Rech, A. Gulinatti, M. Ghioni, S. Cova, S. Weiss, X. Michalet, High-throughput FCS using an LCOS spatial light modulator and an 8×1 SPAD array, *Biomedical Optics Express*, Vol. 1, Issue 5, 2010, 1408-1431

- Colyer 2011 R. A. Colyer, G. Scalia, F. A. Villa, F. Guerrieri, S. Tisa, F. Zappa, S. Cova, S. Weiss, X. Michalet, Ultra high-throughput single molecule spectroscopy with a 1024 pixel SPAD, *Proc. Of SPIE*, Vol. 7905, 2011, 790503
- Conchello 2005 J.-A. Conchello, J. W. Lichtman, Optical sectioning microscopy, *Nature Methods*, Vol. 2, No. 12, Dec. 2005
- Costa 2006 M. Costa, M. Marchi, F. Cardarelli, A. Roy, F. Beltram, L. Maffei, G. M. Ratto, Dynamic regulation of ERK2 nuclear translocation and mobility in living cells, *J Cell Sci*, 119, 23, 2006, 4952-4963
- Denk 1990 W. Denk, J. Strickler, W. Webb, Two-photon laser scanning fluorescence microscopy, *Science*, 248 (4951), 1990, 73-76
- Digman 2008 M. A. Digman, R. Dalal, A. F. Horwitz, E. Gratton, Mapping the Number of Molecules and Brightness in the Laser Scanning Microscope, *Biophysical Journal*, Vol. 94, Issue 6, 15 Mar. 2008, 2320-2332
- Elson 1974 E. Elson, D. Magde, Fluorescence correlation spectroscopy, I. conceptual basis and theory, *Biopolymers*, 13 (1), 1974, 1-27
- Eriksen 2002 R. L. Eriksen, V. R. Daria, J. Glückstad, Fully dynamic multiple-beam optical tweezers, *Optical Express*, 15 July 2002, Vol. 10, No. 14, 597
- Favata 1998 M. F. Favata, K. Y. Horiuchi, E. J. Manos, A. J. Daulerio, D. A. Stradley, W. S. Feeser, D. E. Van Dyk, W. J. Pitts, R. A. Earl, F. Hobbs, R. A. Copeland, R. L. Magolda, P. A. Scherle, J. M. Trzaskos, Identification of a Novel Inhibitor of Mitogen-activated Protein Kinase Kinase, *J. Biol. Chem.*, Vol. 273, 1998, 18623-18632
- Fick 1855 A. Fick, V. on liquid diffusion, *Philosophical Magazine Series 4*, 10 (63), 1855, 30-39

6. References

- Förster 1984 T. Förster, Zwischenmolekulare Energiewanderung und Fluoreszenz, *Ann. Physik*, 437, 1948, 55
- Gey 1952 G. O. Gey, W. D. Coffman, M. T. Kubicek, Tissue Culture Studies of the Proliferative Capacity of Cervical Carcinoma and Normal Epithelium. *Cancer Research*, 12, 1952, 264-265
- Gustafsson 2000 M. G. L. Gustafsson, Surpassing the lateral resolution limit by a factor of two using structured illumination microscopy, *Journal of Microscopy*, Vol. 198, Pt 2, May 2000, 82-87
- Hess 2002 S. T. Hess, W. W. Webb, Focal Volume Optics and Experimental Artifacts in Confocal Fluorescence Correlation Spectroscopy, *Biophysical Journal*, Vol. 83, No. 4, Oct. 2002, 2300-2317
- Heuvelman 2009 G. Heuvelman, F. Erdel, M. Wachsmuth, K. Rippe, Analysis of protein mobilities and interactions in living cells by multifocal fluorescence fluctuation microscopy, *Eur. Biophys. J.*, 38, 2009, 813-828
- Hirvonen 2009 L. M. Hirvonen, K. Wicker, O. Mandula, R. Heintzmann, Structured illumination microscopy of a living cell, *Eur. Biophys. J.*, 38, 2009, 807-812
- Huang 2009 B. Huang, M. Bates, X. Zhuang, Super-Resolution Fluorescence Microscopy, *Annu. Rev. Biochem.*, 78, 2009, 993-1016
- Huisken 2004 J. Huisken, J. Swoger, F. Del Bene, J. Wittbrodt, E. H. K. Stelzer, Optical sectioning deep inside live embryos by selective plane illumination microscopy, *Science*, 305, 2004, 1007-1009
- Jares-Erijman 2003 E. A. Jares-Erijman, T. M. Jovin, FRET imaging , *Nature Biotechnology*, Vol. 21, No. 11, Nov. 2003, 1387-1395

- Jepsen 2005 M. L. Jepsen, 39.1: Invited Paper: Why Analog Silicon May Be Best For LCOS Digital TV. SID Symposium Digest of Technical Papers, 36, 2005, 1358-1361
- Kannan 2007 B. Kannan, L. Guo, T. Sudhaharan, S. Ahmed, I. Maruyama, T. Wohland, Spatially resolved total internal reflection fluorescence correlation microscopy using an electron multiplying charge-coupled device camera, Anal. Chem., 79, 2007, 4463-4470
- Kautsky 1939 H. Kautsky, Quenching of luminescence by oxygen, Trans Faraday Soc., 35, 1939, 216-219
- Khokhlachev 1998 A. V. Khokhlachev, B. Canagarajah, J. Wilsbacher, M. Robinson, M. Atkinson, E. Goldsmith, M. H. Cobb, Phosphorylation of the MAP Kinase ERK2 Promotes Its Homodimerization and Nuclear Translocation, Cell, Vol. 93, 15. May 1998, 605-615
- Kim 2007 S. A. Kim, K. G. Heinze, P. Schwille, Fluorescence correlation spectroscopy in living cells, Nature Methods, Vol. 4, No. 11, Nov. 2007, 963-973
- Klar 2001 T. A. Klar, E. Engel, S. W. Hell, Breaking Abbe's diffraction resolution limit in fluorescence microscopy with stimulated emission depletion beams of various shapes, Physical Review E, Vol. 64, 2001, 066613
- Kogelnik 1966 H. Kogelnik, T. Li, Laser Beams and Resonators, Applied Optics, Vol. 5, No. 10, Oct. 1966
- Lakowicz 2006 Joseph R. Lakowicz, Principles of Fluorescence Spectroscopy 3rd, Springer 2006

6. References

- Lam 1988 J. Lam, J.-M. Delosme, An Efficient Simulated Annealing Schedule: Derivation, Report 8816, Sep. 1988, Department of Computer Science, Yale University and Department of Electrical Engineering, Yale University
- Leonardo 2007 R. Di Leonardo, F. Ianni, G. Ruocco, Computer generation of optimal holograms for optical trap arrays, *Optical Express*, Vol. 15, No. 4, Feb. 2007, 1913
- Leroux 2011 C.-E. Leroux, I. Wang, J. Derouard, A. Delon, Adaptive optics for fluorescence correlation spectroscopy, *Optics Express*, Vol. 19, No. 27, Dec. 2011, 26839
- Lizana 2009 A. Lizana, I. Moreno, A. Márquez, Influence of the temporal fluctuations phenomena on the ECB LCoS performance, *Optics and Photonics for Information Processing III*, Proc. of SPIE, Vol. 7442, 2009, 74420
- Madge 1972 D. Madge, E. Elson, W. W. Webb, Thermodynamic fluctuations in a reacting system – Measurement by fluorescence correlation spectroscopy, *Phys. Rev. Lett.*, 29, 1972, 705-708
- Maurer 2010 L. C. Maurer, A. Jesacher, S. Bernet, M. Ritsch-Marte, What spatial light modulators can do for optical microscopy, *Laser Photonics Rev.*, 2010, 1-21
- Meister 2002 M. Meister, R. J. Winfield, Novel approaches to direct search algorithms for the design of diffractive optical elements, *Optics Communications*, 203, 2002, 39-49
- Minsky 1957 Marvin Minsky, Microscopy Apparatus, US Patent: 3013467, 1957
- Müller 2004 J. D. Müller, Cumulant analysis in fluorescence fluctuation spectroscopy, *Biophysical Journal*, June 2004, Vol. 86, 3981-3992

- Müller 2008 C. B. Müller, A. Loman, V. Pacheco, F. Koberling, D. Willbold, W. Richtering, J. Enderlein, Precise measurement of diffusion by multi-color dual-focus fluorescence correlation spectroscopy. *EPL* 2008, 83, 46001
- Needleman 2009 D. J. Needleman, Y. Xu, T. J. Mitchison, Pin-hole array correlation imaging: highly parallel fluorescence correlation spectroscopy, *Biophysical Journal*, Vol. 96, June 2009, 5050-5059
- Neuman 2004 K. C. Neuman, S. M. Block, Optical trapping, *Review of Scientific Instruments*, Sep. 2004, Vol. 75, No. 9
- Petersen 1986 Petersen, Scanning fluorescence correlation spectroscopy, I. Theory and simulation of aggregation measurements, *Biophys. J.*, Vol. 49, No. 4, Apr. 1986, 809-815
- Petersen 1993 N. O. Petersen, P. L. Höddelius, P. W. Wiseman, O. Seger, K. E. Magnusson, Quantitation of membrane receptor distributions by image correlation spectroscopy: concept and application, *Biophys. J.*, Vol. 65, Issue 3, Sep. 1993, 1135-1146
- Petrášek 2010 Z. Petrášek, K. Suhling, Photon arrival timing with sub-camera exposure time resolution in wide-field time-resolved photon counting imaging, *Optics Express*, Vol. 18, Issue 24, 2010, 24888-24901
- Polin 2005 M. Polin, K. Ladavac, S.-H. Lee, Y. Roichman, D. G. Grier, Optimized holographic optical traps, *Optics Express*, 25 Jul. 2005, Vol. 13, No. 15, 5831
- Rigler 1993 R. Rigler, Ü. Mets, J. Widengren, P. Kask, Fluorescence correlation spectroscopy with high count rate and low background - Analysis of translational diffusion, *Eur. Biophysics J.* 1993, Vol. 22, No. 3, 169-175

6. References

- Robinson 1996 M. J. Robinson, P. C. Harkins, J. Zhang, R. Baer, J. W. Haycock, M. H. Cobb, E. J. Goldsmith, Mutation of position 52 in ERK2 creates a nonproductive binding mode for adenosine 5'-triphosphate, *Biochemistry*, 7, 35(18), May 1996, 5641-5646
- Rust 2006 M. J. Rust, M. Bates, X. Zhuang, Sub-diffraction-limit imaging by stochastic optical reconstruction microscopy (STORM), *Nature Methods*, Vol. 3, No. 10, Oct. 2006
- Seger 1995 R. Seger, E. G. Krebs, The MAPK signaling cascade, *FASEB J.*, 9, 9, 1995, 726-735
- Sergent 2010 N. Sergent, J. A. Levitt, M. Green, K. Suhling, Rapid wide-field photon counting imaging with microsecond time resolution, *Optics Express*, Vol. 18, No. 24, Nov. 2010, 25292-25298
- Sisan 2006 D. R. Sisan, R. Arevalo, C. Graves, R. McAllister, J. S. Urbach, *Biophysical Journal*, Vol. 91, Dec. 2006, 4241-4252
- Šlekys 1994 G. Šlekys, C. O. Weiss, D. Y. Tang, M. F. H. Tarroja, Helical-wave emission of lasers, *J. Opt. Am. B*, Vol. 11, No. 10, Oct. 1994, 2089-2094
- Wiseman 2004 P. W. Wiseman, C. M. Brown, D. J. Webb, B. Hebert, N. L. Johnson, J. A. Squier, M. H. Ellisman, A. F. Horwitz, *Journal of Cell Science*, Nov. 1 2004, 117, 5521-5534
- Wohland 2010 T. Wohland, X. Shi, J. Sankaran, E. H. K. Stelzer, Single plane illumination fluorescence correlation spectroscopy (SPIM-FCS) probes inhomogeneous three-dimensional environments, *Optics Express*, Vol. 18, No. 10, May 2010, 10627
- Wouters 2001 F. S. Wouters, P. J. Verveer, P. I. H. Bastiaens, Imaging biochemistry inside cells, *Trends in Cell Biology*, Vol. 11, No. 5, May 2001, 203-211

7. Appendix

7.1. Additional devices

Alignment-rod

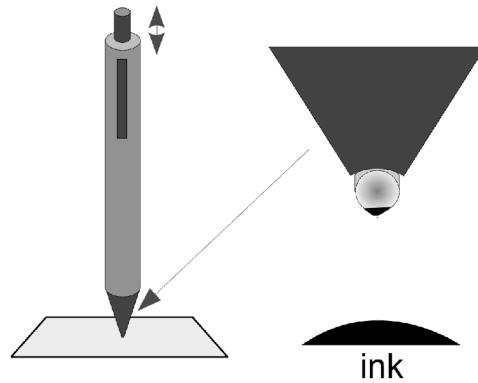
The alignment-rod can be used to align position and angle of the beam path at the back focal plane of the objective. It is a tube, containing two pinholes and four windows and is RMS-mounted to fit the Olympus objective revolver. On this system, the rod has $d = 2$ mm and $l = 0.4$ m. It is contrary to a check mark on the ceiling at a higher distance and using both, non objective and an air objective with a high focal length, which allows an even more precise positioning, but can not determine the angle.



7.1. Appendix

Creation of light-blocker via steel point printing device

The quite perfect round ball of a spring mounted ballpoint pen is dipped into viscous stamping ink and the tip returned into the pen. Pointing the pen on a glass slide, the button of the tip has to be hit shortly. Depending of the amount of ink, the range and duration of hitting the button, the size of the spot changes.



7.2. Equations

Intermediate steps of the equations in derivation of the diffusion model in *chapter 2.1*.

(a 2.i)

$$\frac{\partial}{\partial t} \delta C(\vec{r}, t) = D \nabla_{\vec{r}}^2 \delta C(\vec{r}, t) \quad (\text{e 7.xii})$$

$$\frac{\partial}{\partial t} \int_{\mathbb{R}^3} e^{i\vec{p}\vec{r}} \delta \hat{C}(\vec{p}, \tau) d\vec{p} = D \nabla_{\vec{r}}^2 \int_{\mathbb{R}^3} e^{i\vec{p}\vec{r}} \delta \hat{C}(\vec{p}, \tau) d\vec{p}$$

$$\int_{\mathbb{R}^3} e^{i\vec{p}\vec{r}} \frac{\partial}{\partial t} \delta \hat{C}(\vec{p}, \tau) d\vec{p} = \int_{\mathbb{R}^3} \nabla_{\vec{r}}^2 e^{i\vec{p}\vec{r}} D \delta \hat{C}(\vec{p}, \tau) d\vec{p} \quad | \quad \nabla_{\vec{r}}^2 \delta \hat{C}(\vec{p}, \tau) = 0$$

$$\int_{\mathbb{R}^3} e^{i\vec{p}\vec{r}} \frac{\partial}{\partial t} \delta \hat{C}(\vec{p}, \tau) d\vec{p} = \int_{\mathbb{R}^3} i^2 \vec{p}^2 e^{i\vec{p}\vec{r}} D \delta \hat{C}(\vec{p}, \tau) d\vec{p} \quad | \quad \text{Fourier transform is a bijection in } \mathbb{R}^3$$

$$\frac{\partial}{\partial t} \delta \hat{C}(\vec{p}, \tau) = -\vec{p}^2 D \delta \hat{C}(\vec{p}, \tau)$$

$$\delta \hat{C}(\vec{p}, \tau) = \delta \hat{C}(\vec{p}, 0) e^{-\vec{p}^2 D \tau}$$

$$\int_{\mathbb{R}^3} e^{i\vec{p}\vec{r}} \delta \hat{C}(\vec{p}, \tau) d\vec{p} = \int_{\mathbb{R}^3} e^{i\vec{p}\vec{r}} \delta \hat{C}(\vec{p}, 0) e^{-\vec{p}^2 D \tau} d\vec{p}$$

$$\delta C(\vec{r}, \tau) = \int_{\mathbb{R}^3} e^{i\vec{p}\vec{r}} \frac{1}{(2\pi)^3} \int_{\mathbb{R}^3} e^{-i\vec{p}\vec{r}''} \delta C(\vec{r}'', 0) d\vec{r}'' e^{-\vec{p}^2 D \tau} d\vec{p} \quad (\text{e 7.xiii})$$

(a 2.ii)

$$\begin{aligned}
\langle \delta C(\vec{r}', 0) \delta C(\vec{r}, \tau) \rangle &= \frac{1}{(2\pi)^3} \int_{\mathbb{R}^3} e^{i\vec{\rho}\vec{r}} \int_{\mathbb{R}^3} e^{-i\vec{\rho}\vec{r}''} \langle C \rangle \delta(\vec{r}' - \vec{r}'') d\vec{r}'' e^{-\vec{\rho}^2 D\tau} d\vec{\rho} \\
&= \frac{\langle C \rangle}{(2\pi)^3} \int_{\mathbb{R}^3} e^{i\vec{\rho}\vec{r}} e^{-i\vec{\rho}\vec{r}'} e^{-\vec{\rho}^2 D\tau} d\vec{\rho} \\
&= \frac{\langle C \rangle}{(2\pi)^3} \int_{\mathbb{R}^3} e^{i\vec{\rho}(\vec{r} - \vec{r}') - \vec{\rho}^2 D\tau} d\vec{\rho} \\
&= \frac{\langle C \rangle}{(4\pi D\tau)^{3/2}} e^{-\frac{(\vec{r} - \vec{r}')^2}{4D\tau}}
\end{aligned} \tag{e 7.xvi}$$

(a 2.iii)

$$\begin{aligned}
G(\tau) &= \frac{\int_{\mathbb{R}^3} \int_{\mathbb{R}^3} I_0 e^{\left(\frac{2(x^2+y^2)}{s^2} - \frac{2z^2}{u^2}\right)} I_0 e^{\left(\frac{2(x'^2+y'^2)}{s^2} - \frac{2z'^2}{u^2}\right)} \frac{\langle C \rangle}{(4\pi D\tau)^{3/2}} e^{-\frac{(\vec{r} - \vec{r}')^2}{4D\tau}} d\vec{r} d\vec{r}'}{\langle C \rangle^2 \left(\int_{\mathbb{R}^3} I(\vec{r}) d\vec{r} \right)^2} \\
&= \frac{1}{\langle C \rangle s^2 u \pi^{3/2}} \left(\frac{1}{1 + \frac{4D\tau}{s^2}} \right) \sqrt{\frac{1}{1 + \frac{4D\tau}{u^2}}} \quad \left| \begin{array}{l} \pi^{3/2} s^2 u = V_0 \\ \frac{s^2}{4D} = \tau_D \end{array} \right. \\
&= \frac{1}{\langle C \rangle V_0} \left(\frac{1}{1 + \frac{\tau}{\tau_D}} \right) \sqrt{\frac{1}{1 + \left(\frac{s}{u}\right)^2 \frac{\tau}{\tau_D}}} \quad \left| \begin{array}{l} \langle C \rangle V_0 = \bar{N} \\ \frac{u}{s} = \sigma_S \end{array} \right. \\
&= \frac{1}{\bar{N}} \left(\frac{1}{1 + \frac{\tau}{\tau_D}} \right) \sqrt{\frac{1}{1 + \frac{1}{\sigma_S^2} \frac{\tau}{\tau_D}}}
\end{aligned} \tag{e 7.xvii}$$

$\underbrace{\hspace{1.5cm}}_{G(0)} \quad \underbrace{\hspace{3.5cm}}_{D(\tau)}$

7.3. Fluorescence Cumulant Analysis (FCA)

The cumulants of the counts emitted by diffusing particles in a defined volume are given by equation *e 2.xx*. To combine data obtained by different confocal volumes, the contributions from the detection and the illumination system have to be separated from the observed values ε_i and N_i .

To normalize N_i , the fractional concentration α_i of the total number of particles N is introduced. N is the sum of N_i over all species and equal to an effective concentration C in the observed volume V :

$$N = \sum_{i=1}^s N_i = C V$$

The fractional concentration α_i is given by:

$$\alpha_i = \frac{N_i}{N} = \frac{C_i}{C} \quad \text{with} \quad \sum_{i=1}^s \alpha_i = 1$$

The brightness ε_i is separated into the molecules b_i the system factor S :

$$\varepsilon_i = b_i S$$

With these expansions, *e 2.xx* yields to:

$$\kappa_{[r]} = \gamma_r V S^r C \sum_{i=1}^s b_i^r \alpha_i$$

The coefficients α_i and b_i are only depending on the sample, while the coefficients γ , V and S , disregarding optical density differences in the sample, only depend on the imaging system.

For a homogeneous sample of molecules, used for the calibration of the imaging system, with an effective brightness b_{Cal} and a concentration of C_{Cal} , κ_r yields to:

$$\kappa_{Cal,[r]} = \gamma_r V S^r C_{Cal} b_{Cal}^r$$

Each factorial cumulant can now be normalized by the corresponding term of the calibration sample:

$$\kappa_{[r]}^- = \frac{\kappa_{[r]}}{\kappa_{Cal,[r]}} = \frac{C}{C_{Cal}} \sum_{i=1}^s \left(\frac{b_i}{b_{Cal}} \right)^r \alpha_i$$

The obtained expression is independent of the imaging system coefficients γ , V and S .

For two species, defining $f = b_2/b_1$, $b = b_1/b_{Cal}$, $\alpha = \alpha_2$, and $c = C/C_{Cal}$, the cumulants can be written as:

$$\kappa_{[r]}^- = c b^r [(1-\alpha) + f^r \alpha]$$

For n measurements, the equations have $2n + 2$ unknown, c and α for each measurement and b and f global. Note, that the cumulants are no longer dependent on γ . If for each measurement k cumulants are calculated, they create $k \cdot n$ equations. Therefore three cumulants per measurement should be sufficient.

7.4. Protocols

(a 4.i)

Mammalian cell culture (HeLa)

Human cervical adenocarcinoma HeLa cells (ATCC, American Type Culture Collection, Manassas, VA, USA) [Gey 1952] were maintained in Dulbecco's Modified Eagle's Medium (DMEM, PAN-Biotech GmbH) supplemented with 10% fetal calf serum (FCS, PAN-Biotech GmbH) 1% L-Glutamine (GIBCO/Invitrogen Life Technologies) and 1% non-essential amino acids (NEAA, GIBCO/Invitrogen Life Technologies).

Cells were grown at 37°C in a 90% humidified incubator with 5% CO₂.

Growth Medium was changed every two days to maintain appropriate growth conditions.

For HeLa subculture 80-90 % confluent cells were washed once with 10 mL DPBS (PAN-Biotech GmbH) followed by the addition of 2 ml Trypsin/EDTA (PAN-Biotech GmbH) which was subsequently aspirated. Cells were trypsinised for approximately 5 min at 37°C. Detached cells were harvested with 5 mL fresh growth medium to inactivate trypsin and gently

7.4. Appendix

resuspended, achieving a homogenous cell suspension. Cells were usually split three times a week into new culture flasks with an amount of 10^6 cells, depending on the needs of the experiment. In order to seed the desired amount of cells, the cell number per ml cell suspension was determined using the Vi-Cell XR cell viability analyzer (Beckman Coulter GmbH).

For the SRFCS experiments cells with an amount of 10^4 cells per well were seeded on 8-well Lab-Tek chambers (Nalge Nunc International, Rochester, NY, USA), the cell number per ml cell suspension was determined as described before. Cells were usually transfected one day after passaging.

Transfection of mammalian cells

Transfection is defined as the artificial introduction of nucleic acids into higher eukaryotic cells using non-viral methods. These days, various methods and protocols, as well as transfection reagents, are established and available.

HeLa cells were transfected with endotoxin-free plasmid DNA via lipid-mediated endocytosis of the transfection reagent-DNA complexes.

The transfection reagent used was Fugene 6 (Roche Applied Science), a non-liposomal reagent that allows the formation of stable complexes (micelles) with DNA. Fugene 6 shows virtually no cytotoxicity and leads to high transfection efficiencies in HeLa cells. Fugene 6 reagent-DNA ratios of 3:1 have been used for all experiments. 3 μ L Fugene were diluted in 100 μ L serum-free DMEM and incubated at room temperature (RT) for 5 min. 500 ng of total plasmid-DNA (co-transfection: 250 ng for each construct) was added, mixed and incubated for 15 min at RT. Fugene 6 reagent-DNA complexes (~25 μ l) were added to the cells in a drop-wise manner and the chambers were subsequently swirled to ensure a homogenous distribution of the complex over the entire surface. Cells were incubated at 37°C with 5 % CO₂ until further treatment. In general, cells were transfected one day prior to the SRFCS measurement. Usually, only the inner 4 wells out of a 8-well LabTek chamber were used for each experiment.

(a 4.ii)**LAPAP**

In order to achieve laser-assisted adsorption of Biotin-4-Fluorescein (B4F) on glass, a 8-well LabTek chamber (Nunc) was incubated with 400 μ l of 3% bovine serum albumin (BSA) in phosphate buffered saline (PBS) for 20 min at room temperature (RT) to passivate the glass surface. Afterwards, BSA/PBS was discarded and the chamber was subsequently incubated with 200 μ l B4F in 3% BSA/PBS with a final concentration of 50 μ g/ml. The sample was protected from light prior to photobleaching.

Photobleaching was performed for different illumination durations as well as with different patterns. After photobleaching, the chambers were rinsed with 3% BSA/PBS three times and then incubated with 5 μ g/ml streptavidin labeled with Cy5 in 3% BSA/PBS for 30 min at RT, following three PBS washing steps. The biotinylated fluorophore ATTO565-biotin, diluted in Dimethylformamide (DMF) to a final concentration of 1 mg/ml was further diluted in 200 μ l 3% BSA/PBS to achieve a final concentration of 5 μ g/ml and incubated for 25 min at RT, protected from light. Prior to acquisition, the remaining fluorophores were removed by three PBS washing steps.

(a 4.iii)**Mono and double Citrine**

Cells were either transfected with 500 ng mono Citrine or double Citrine, using Fugene 6 as described in (a 4.i). SRFCS measurements were performed in imaging medium on the following day.

(a 4.iv)**Rapamycin-induced dimerization of FRB and FKBP**

For rapamycin-induced fusion of FKBP and FRB, cells were co-transfected with 250 ng FKBP-mCitrine and 250 ng FRB-mCitrine using Fugene 6, as described in (a 4.i). SRFCS measurements were performed in imaging medium. 5 μ M of rapamycin (BioAustralis Fine Chemicals, Australia) were diluted in imaging medium and added to each well in order to induce the dimer formation.

7.4. Appendix

(a 4.v)

Erk2 wild-type and Erk(K52R)

For Erk2 translocation experiments, cells were co-transfected in the morning with 250 ng Erk2-mCitrine (wt or K52R) and Mek1-mCherry using Fugene 6 and starved in serum-free DMEM overnight on the same day.

For SRFCS experiments on the next day, starvation medium was changed to imaging medium (PAN-Biotech GmbH) and stimulation in imaging medium with 100 ng/ml human recombinant EGF (Cell Signaling Technology Inc., Danvers, MA, USA), a small (6 KDa) polypeptide hormone which has mitogenic properties and is able to enhance growth in many cell types, was performed for Erk2 activation.

Mek UO126 inhibitor

HeLa cells were co-transfected with Erk2-mCitrine (wt) and Mek1-mCherry as previously described and starved overnight. Measurements were performed in imaging medium (PAN-Biotech GmbH). 10 μ M UO126 (Cell Signaling Technology Inc., Danvers, MA, USA), diluted in imaging medium, were incubated 20-30 min prior to EGF-stimulation. UO126 (1,4-diamino-2,3-dicyano-1,4-bis[2-aminophenylthio] butadiene) is a highly selective inhibitor of MEK 1 and MEK 2 and prevents phosphorylation of Erk2.

7.5. Software manual with explanations

This system control software is written for LabVIEW 2010 with Vision Addon and Python 2.7.2. Additional software is required, which can be found inside the subfolder "manuals and software".

1. Simple Controls

Small programs for controlling the microscope to run in parallel with the main software.

1.1 OD Filter Wheel (filterwheelReceiver.vi)



1.1a.: filterwheelReceiver.vi, running, on start position.

This VI is required to control the OD filter wheel. The position can also be changed directly on the filter wheel, as long as this software is not running. It is also used by the software described in chapter 3.

The buttons named +1 and -1 increase or decrease the position of the filter wheel. It is not possible to switch between 1 and 6 directly for safety reasons. The button "reread Position" reads the current position of the filter wheel. Otherwise the dial shows the position expected from commands sent to the wheel. The number in the right lower corner is another possibility to set the filter wheel position.

The wheel always starts at position 4, which blocks the light completely. For emergency blocking use the X-button in the upper right corner. It will position the wheel to 4 and stop the software afterwards.

Position 5 (OD __) is appropriate for calibrations done with a fluorescent plate, minimal laser power and APDs.

Position 6 (OD __) should be used for calibrations done with a fluorescent plate, minimal laser power and the CCD camera.

Position 1 (empty), 2 (OD __) and 3 (OD __) are thought to be used while measuring solutions and cells.

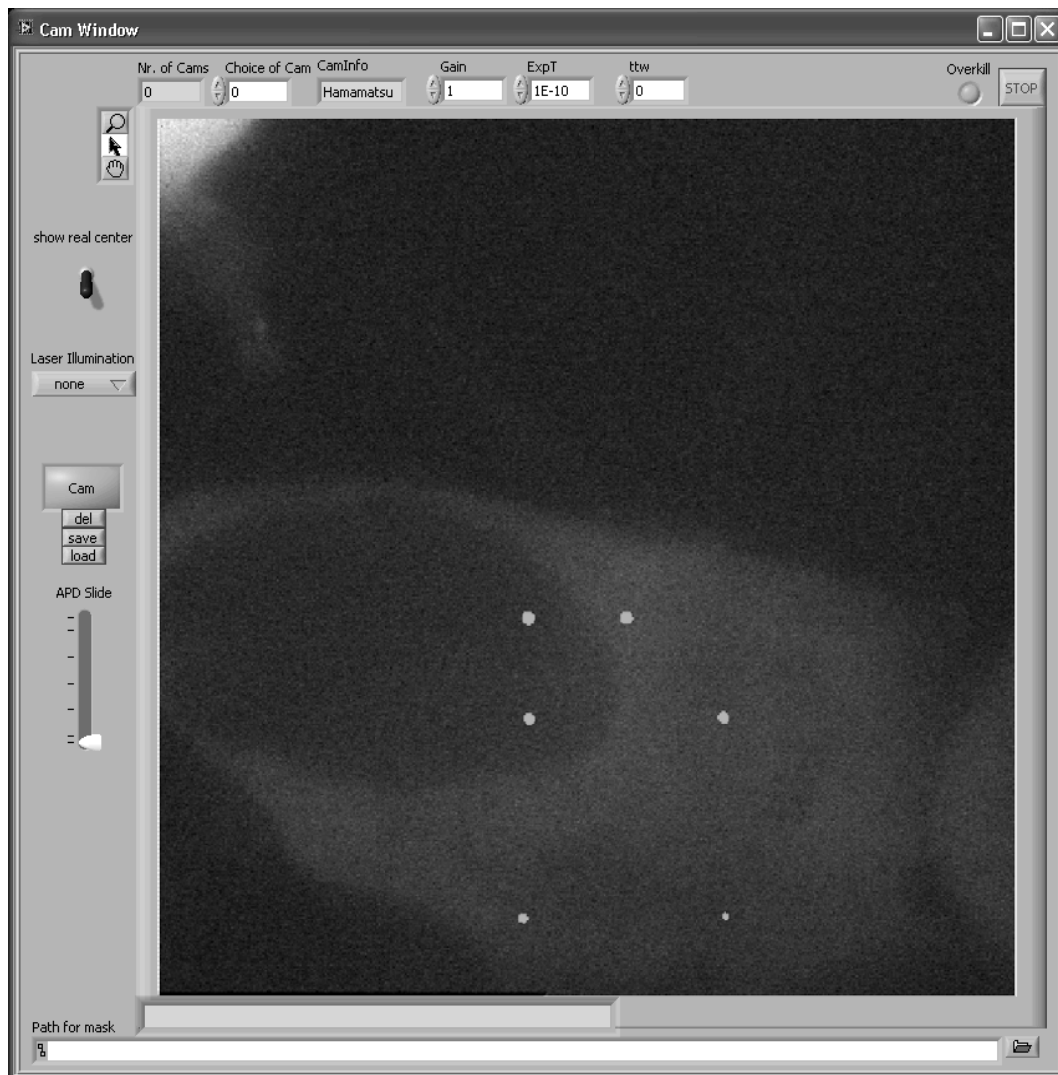
7.5. Appendix

Troubleshooting: No communication.

Perhaps the Com port changed. The Com port input can be found by double clicking on the top bar.

Additionally an offset for the position (modS) could be set. Do not change baud rate for this filter wheel.

1.2 Cam Window (CamWindow.vi)



1.2.a: Cam.vi, with "show real center" (cross hairs) switched on.

Do not start this VI if another program needs to access the camera. E.g. do not run it while starting any software described in chapter 2. or while starting "Cam Master" or "APD Master". After starting, a pop-up asks for the wavelength of the laser to select the correct pattern for "Laser Illumination" distributions.

The camera image is displayed in a grey scale with overexposed pixels shown in red and underexposed pixels in blue. If overexposed regions seem to smear downwards (blooming), the camera is critically overexposed and the exposure time should be reduced immediately!

Atop of the camera image, the following controls are located (left to right):

Nr. of Cams	How many (running) cameras are connected to the PC.
Choice of Cam	Chosen camera. (Labview counts from zero, so zero is the first camera found)
CamInfo	Name of chosen camera.
Gain	Sets the gain of an EMCCD-camera.
ExpT	Exposure time (in seconds).
ttw	Time to wait (in seconds). - How long to wait between measurements.
Overkill	This button turns red, if you overexpose the camera. If this occurs after changing the Gain or ExpT, the software automatically reverts to the previous settings.
STOP	Use this button to stop the Camera Windows.

“Show real center” enables cross hairs showing the center of the camera.

The switch below allows to choose between some laser light distributions:

focus	Background correction of SLM, resulting in focused beam.
Wide	A fake widefield illumination, resulting in a structured but broad illumination (real widefield would be possible, but would result in high light losses).
haircross	An illumination of crossing hairs, nice to focus.
none	No pattern.

Green Cam/ red APD button (with del button and APD Slide):

This helps to remember the positions of aligned light while using widefield alignment. E.g. use this while using a wanted light alignment for fibers and position a cell in widefield, knowing where the fiber illuminations would be.

Change to APD while a light distribution should be marked and saved. Slide the “APD Slide” to set threshold. Change back to Cam to hold markings and press “del” to delete markings.

“Save” saves the mask (picture with values of 0 for background and 1 for green) to a *.tiff-file defined in “Path for mask”, and “load” will open an old mask file.

On the left side of the camera image, some picture interaction options are given (top to bottom):

magnifying glass	Zoom in. To zoom out, right-click on the image and chose "Zoom to Fit".
Arrow	Standard. No interaction.
Hand	In case of a partial image (zoomed in) this hand can move the visible part.

Of the right click menu on the camera image only two options are interesting, "Zoom to Fit" to resize the image to fit the window, and "Save Image ..." to save it.

2. “Self calibrating, free positioning software”

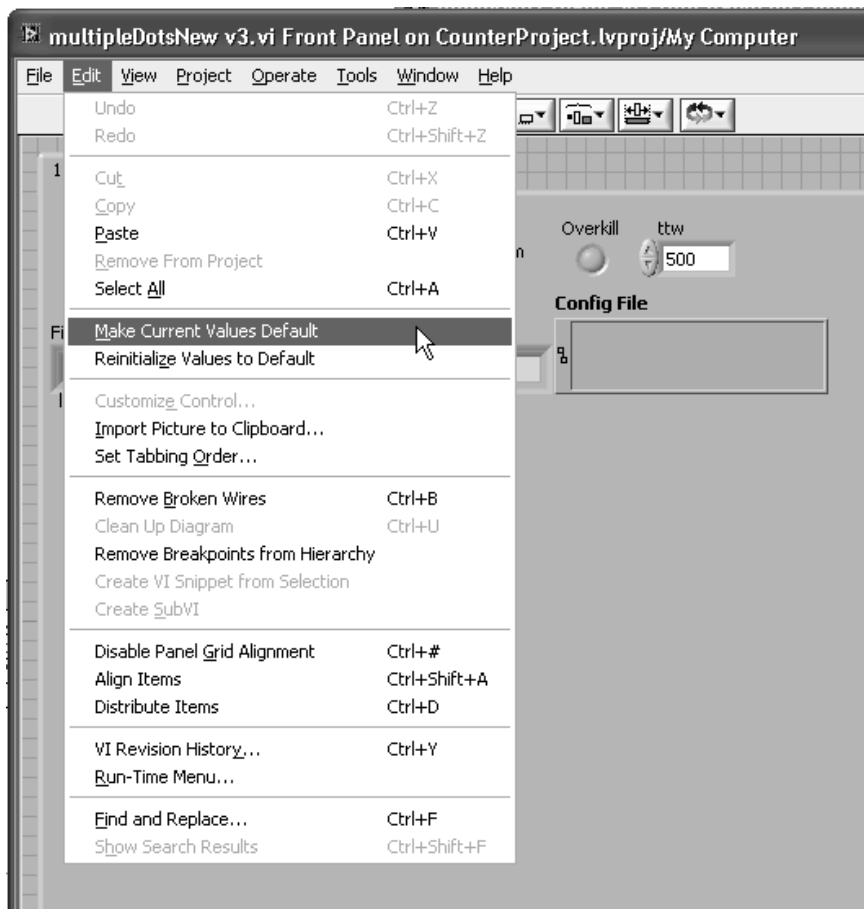
This system enables the user to use a spatial light modulator (SLM, e.g. an LCoS) to illuminate the sample with multiple, freely positioned spots. In order to achieve this, it calibrates the patterns sent to the SLM depending on the resulting light distribution arriving at a camera.

The Master.vi is a top level VI, which starts several sub-VIs minimizing the input required of a standard user. While for single uses all changes can be done while running the Master.vi, for permanent changes some sub-VIs have to be opened separately. These are "Calibration v2.vi" and "multipleDotsNew v3.vi", and in rare cases the small "trySizes.vi". Other sub-VIs have to be changed if using unsupported camera (in general non Hamamatsu cameras).

There are some additional changes to be done inside the "configfiles" subfolder in case of changing the SLM.

The first part of each chapter explains the course of actions for the standard-user, simply using the software. In the grey box each major part of the software is explained in more detail.

While in standard-protocol the big VIs “Calibration v2.vi” and “multipleDotsNew v3.vi” run automatically, all settings can be changed in expert mode. To change the default settings permanently open these vis directly, change the settings and click on the task bar on “Edit” → “Make Current Values Default” and save the changes (“File” → “Save”).



2.a: Change default values in vi.

2.0. Speed run

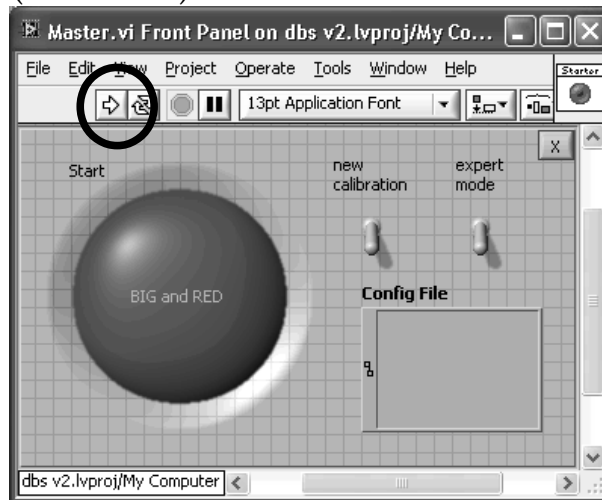
Shortest version of the manual for using this software.

- (1) Turn on laser, camera, SLM and microscope. Set laser power to minimum and beam path to camera. Use fluorescent plate.
- (2) Start "Master.vi" by using the small arrow in the top bar.
- (3) On the first pop-up click "Yes" if a preview camera image as is desired. Stop and close the "Camera" by using the stop button to continue.
- (4) Select "new calibration" if a new calibration is required. Otherwise a calibration file will be requested.
- (5) Push the red button.
- (6) If a new calibration is required, a second pop-up asks for "changed external settings". Click yes if not sure, which settings are default.
 - (a) In this case, a small pop-up named "Wavelength" will ask for the laser wavelength.
 - (b) A bigger panel opens, the "Calibration with camera". In case of "changed settings", a second pop-up named "Test size parameters" starts immediately.
 - (c) In "Test size parameters" increase "StepNr" until all 4 dots are near the borders. Click on "ok". Set "Nr of Steps" to 400 and press enter. Click on "run".
 - (d) If "Find center" pops up, click on "run".
 - (e) Wait until calibration is finished (ca. 30Min.) and save calibration-file.
- (7) "Light distribution settings" starts. Wait until the third slide named "Dots" is shown.
 - (a) If "Find center" pops up, click on "run".
 - (b) Position dots by double clicking on camera image (crosshair icon selected).
 - (c) Position dots by using the table. The table rows are: x, y, focal length of additional lens, L for donuts, a button to activate dots and the intensity of the camera image on dot position.

2.1. Standard-protocol

Turn on laser, camera, SLM and microscope. Set laser to lowest power and beam path to camera. Use fluorescent plate.

2.1.1 Cam Master (Master.vi)



2.1.1.a: Master.vi, not running.

Open the Master.vi and start it by using the small arrow in the top-bar. After starting, only the grey area is being used.

new calibration switch	Activate it if you do not want to use an existing calibration.
expert mode switch	This enables you to change all settings inside the major sub-vis.
red button	This button runs the system.
The "X"	Stops the software.

After starting the VI, a pop-up will occur.

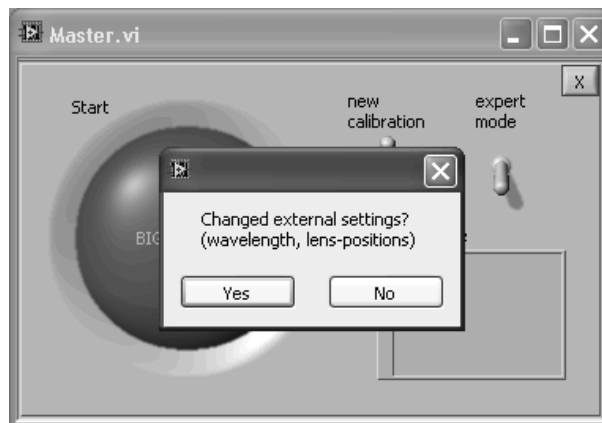


2.1.1.b: Master.vi, camera pop-up.

Choose “Yes” to open a window showing the camera. This could be useful for manual pre-calibrations, testing the pre-calibrations or simply to look at a sample. See chapter 2.1.2.

Use the red button to continue.

If “new calibration” is chosen, a second pop-up will appear.



2.1.1.c: Master.vi, calibration pop-up.

The system is configured for one wavelength and one objective as standard. If the laser wavelength changes, a different objective is used, or the system is otherwise altered, choose “Yes”. In fact, this only starts a small sub-vi (see chapter 2.1.3) and a second small vi later on, during the “calibration v2.vi” (see chapter 2.1.5). Both do not take much time. Next, the “calibration v2.vi” is started. See chapter 2.1.4.

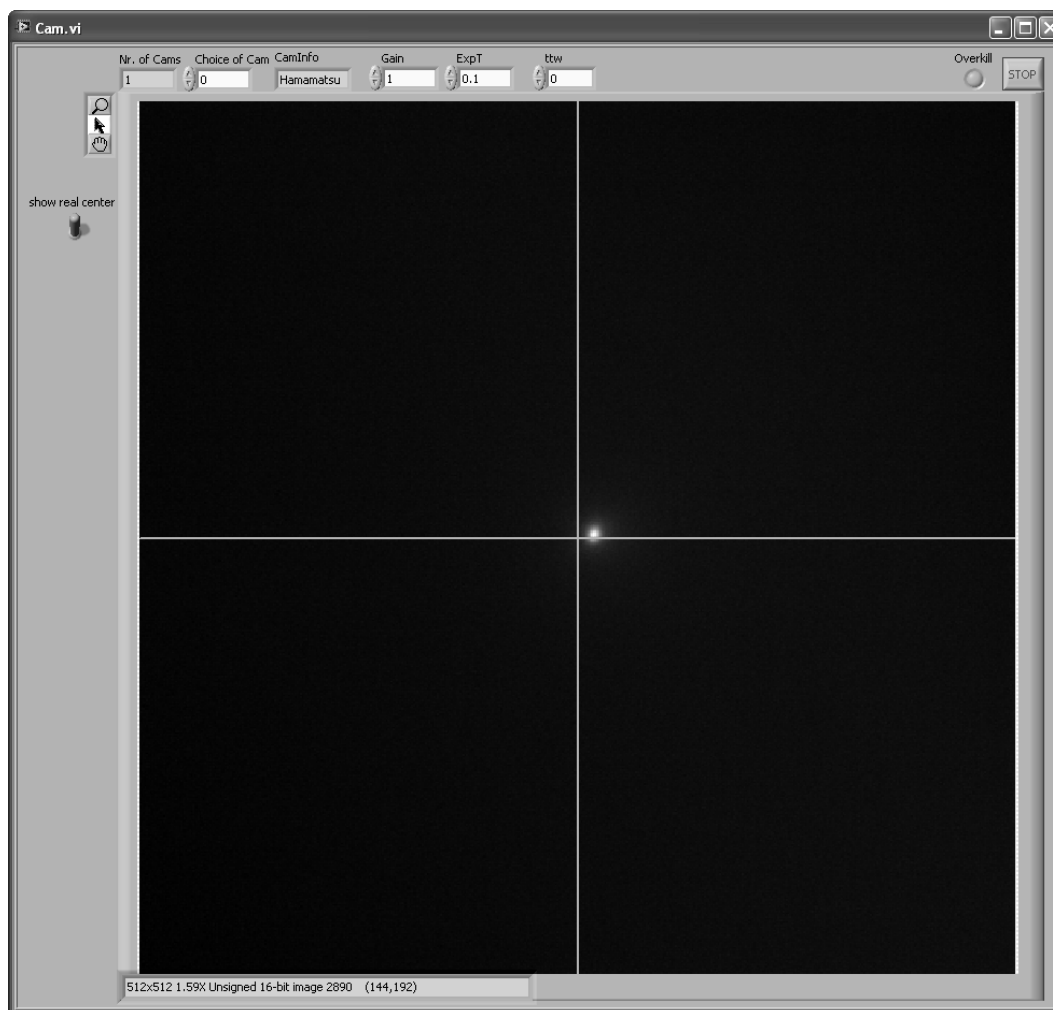
If “new calibration” is not chosen, another pop-up will ask for an existing calibration file and the software starts the “multipleDotsNew v3.vi”. See chapter 2.1.7.

Expert Mode and additional information:

Switch “expert mode” on to use the expert mode.

7.5. Appendix

2.1.2 Camera (Cam.vi)



2.1.2.a: *Cam.vi*, with "show real center" (cross hairs) switched on.

This VI only shows up, if you clicked "Yes" on the previous pop-up (see Image 2.1.1.b). It can also be started separately, as long as no other software needs the camera. Besides of showing the output of the camera, cross hairs can be overlaid, using the "show real center" switch. For pre-calibrations, or checking the existing one, use a fluorescent plate. In an ideal pre-calibration, a single dot should be sharp and centered. Focus the microscope, if necessary. Use the "STOP" button on the right top side, to stop this camera-window and continue with the Master.vi.

Overexposed pixels are shown in red, and unexposed in blue. If parts of the image seem to smear downwards, the camera is critically overexposed!

Atop of the camera image, following panels are given (left to right):

Nr. of Cams	How many (running) cameras are connected to the PC.
Choice of Cam	Chose camera. Labview counts from zero, so zero is the first camera found.
CamInfo	Name of chosen camera.
Gain	Changes the gain of an EMCCD-camera.
ExpT	Exposure time. How long each image should be measured.
ttw	Time to wait. How long to wait between measurement.
Overkill	This button turns red, if you overexpose the camera. If this occurs after changing the Gain or ExpT, the software automatically jumps back to the old settings.
STOP	Use this button to stop the Cam.vi.

On the left side of the camera image, some picture interaction options are given (top to bottom):

magnifying glass	Zoom in. To zoom out, right click on the image and chose "Zoom to Fit".
Arrow	Standard. No interaction.
Hand	In case of a partial image (zoomed in) this hand can move the visible part.

Of the right-click-menu on the camera-image only two options are interesting, "Zoom to Fit" to resize the image to fit the window, and "Save Image ..." to save it.

2.1.3 Wavelength (wavelengthTOgreylvlnumber_v2.vi)



2.1.3.a: *wavelengthTOgreylvlnumber_v2.vi*

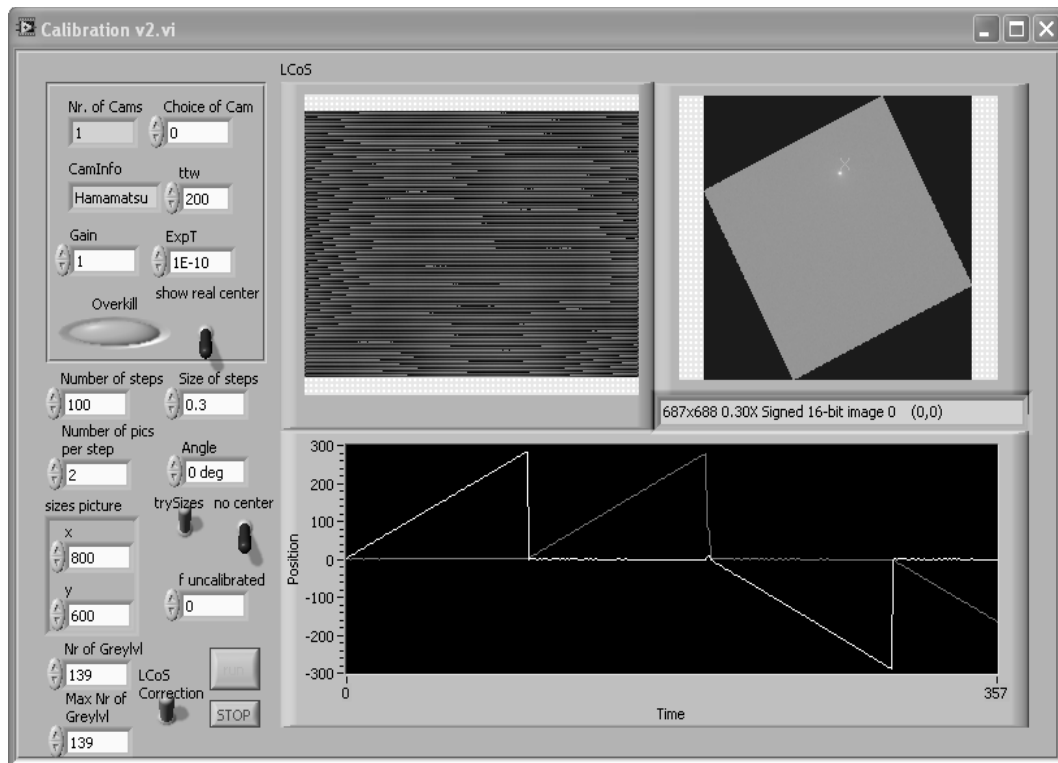
Choose a wavelength and click "GO". The wavelength is needed for some internal settings of the Hamamatsu LCoS and is used to load the correct correction-image for the specific LCoS.

Expert Mode and additional information:

Only differentiated settings for wavelength set to given correction-images. To change possible settings for wavelength, right-click on the wavelength panel → "Edit Items...". A correction-image in the "configfiles" (see Appendix) for each given wavelength is needed.

7.5. Appendix

2.1.4 Calibration with camera (Calibration v2.vi)



2.1.4.a: Calibration v2.vi, while running in last quarter of calibration.

Without switching to “expert mode”, there are no settings to change in this VI. There are three images on the right side. Top left is the image used to control the SLM. Top right is the resulting camera image. On the bottom the measurement data are plotted. Two lines represent the deflection of the light in x in y. Two sawtooth-graphs should be the result, only one line leaving zero at each time. If single measurement-points are too far off, they will be cut out. After finishing the calibration, a pop-up will ask you to save the calibration-file. Although the ending of the file is irrelevant, chose “*.txt” for clarity. The files can be opened with a text editor. Explanations of the calibration files can be found in the appendix.

Expert Mode and additional information:

The calibration runs in multiple steps. First, the center-position is determined. Then multiple patterns resulting in a deflection in one single direction are created and the resulting deflection measured. These values are used to determine the angle between the single axis of the LCoS and the axis of the camera-image. The camera-image will be rotated to overlay both axes and the center-position is determined in the rotated image.

Patterns to deflect the light in a single axis direction are created, the deflection increases steadily and the deflection is measured and shown as a graph. These steps are repeated for all four directions.

Using a linear fit onto the series of measurements, single measurements beyond a threshold are deleted.

The finished calibration including all settings are saved to a calibration-file (see Appendix).

Depending on chosen options before, some settings are already selected depending on configuration files.

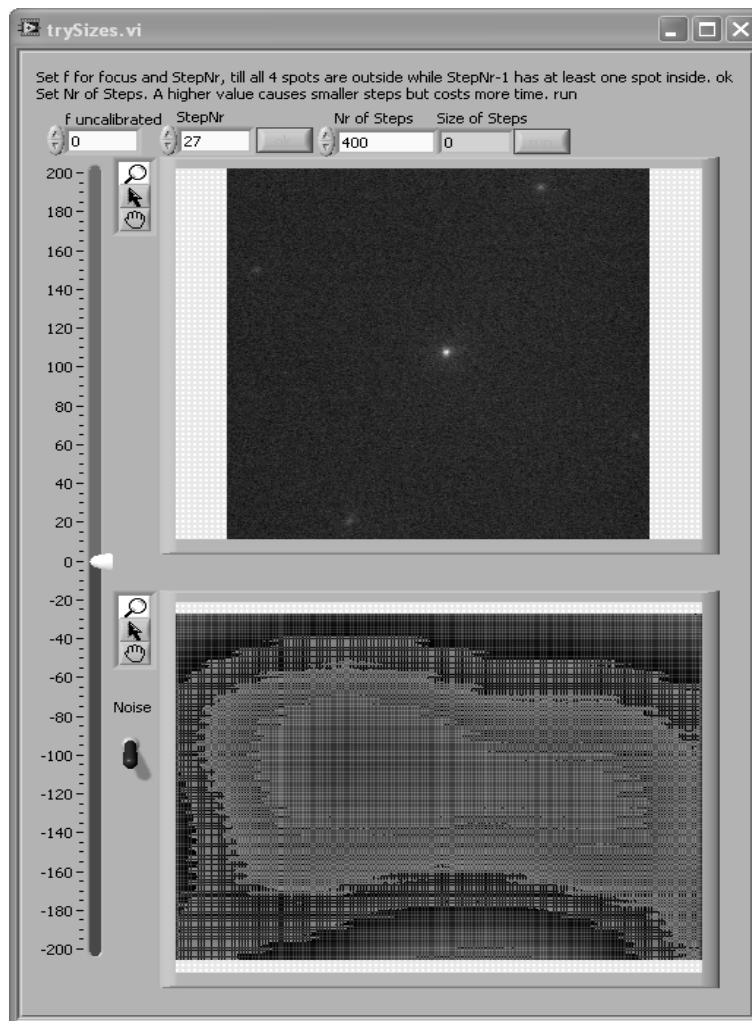
The upper square on the left side only contains camera controls, identical to “Cam.vi”(see 2.2.2). Below this:

Number of Steps	How many measurement steps per direction (+x, -x, +y, -y) should be done.
Size of Steps	Show size per intermediate step (total steps done = Number of Steps x Size of Steps).
Number of pics per step	How many single measurements should be done per step. The average of the position is used.
Angle	Before calibrating the steps, a single direction is used to determine the angle in the beam path between SLM and camera. In case of a not centered starting point, the direction of this measurement can be chosen to achieve a maximal length of measurement.
trySizes	Switch on to use “trySizes.vi” (see 2.2.5) to determine the total steps required to create deflections ranging the whole camera image. “trySizes” will set “Number of steps” and “Size of steps”.
no center	Switch on to use “noCenter v2.vi” (see 2.2.6) to determine the center-position.
sizes picture, x and y	Number of pixels of the controlling image for the SLM in x and y.
f uncalibrated	Creates an additional lens to focus the light, if needed. 0 = no lens.
Nr of Greylvl	Number of different grey levels, evenly distributed between 0 and “Max Nr of Greylvl” (max. value 255). The number has to have at least as many digits as “Max Nr of Greylvl” -1 digit.
Max Nr of Greylvl	Highest (brightest) color used for the patterns of the controlling image for the SLM (0 = black; 255 = white).
LCoS Correction	Switch on to use a correction pattern to correct for imperfectness of the SLM.
Run	Click run to start calibration.
STOP	Click stop to stop calibration before finishing.

This VI can be started as a single scrip. In this case, a correction image for the LCoS can be chosen manually. The “Calibration v2.vi can run without using “Master.vi”.

7.5. Appendix

2.1.5 Test size parameters (trySizes.vi)



2.1.5a: trySizes.vi

In order to determine the maximal needed deflection of the light, this VI creates 4 dots, one in each direction with the same size of deflection. Increase the panel "StepNr" until all four dots disappear to the sides. Due to the symmetry of the alignment, they might vanish in between, too. Additionally to the four dots, the symmetry of the pattern and the grating of the SLM create additional, unwanted ghost dots.

The top image shows the camera image, the bottom image shows the image sent to the SLM.

The slider	On the left side corresponding to "f uncalibrated".
"Noise" switch	Add noise increasing the scattered light but decreasing the intensity of pattern created ghost dots.

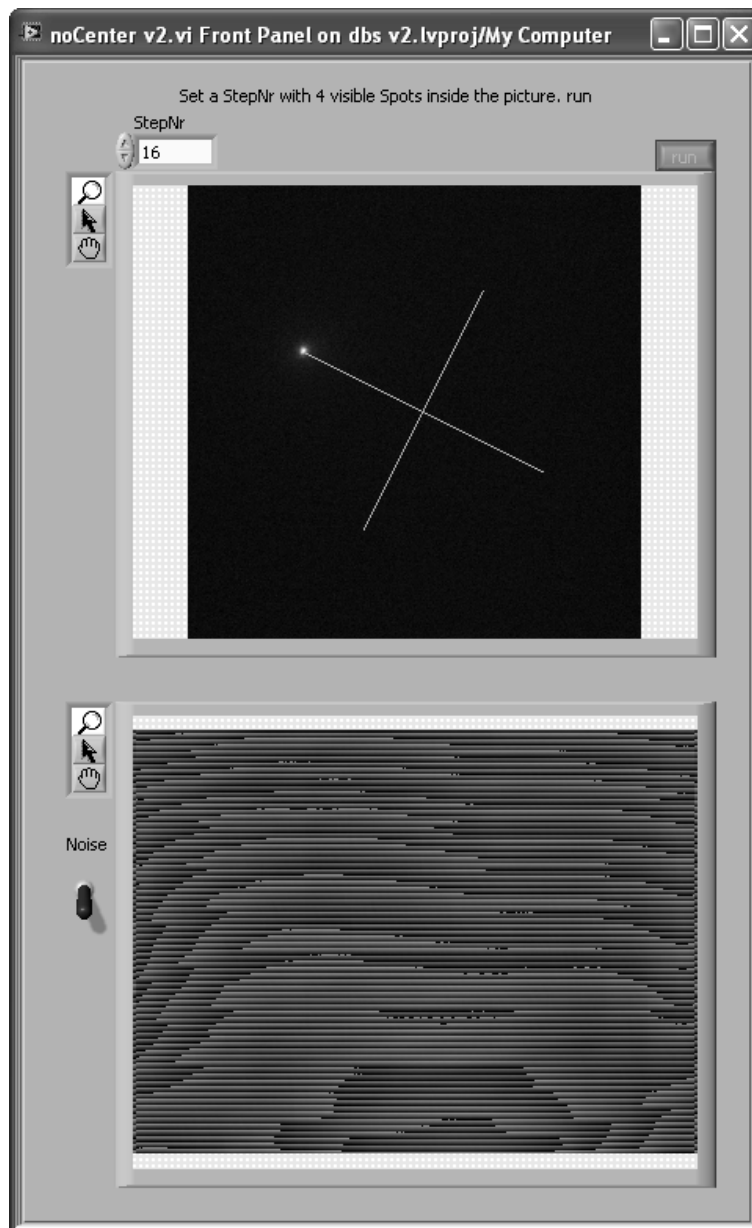
Usage, top line of panels, left to right:

f uncalibrated	Creates an additional lens to focus the light, if needed. 0 = no lens.
StepNr	Chose total deflection, according to visibility of the four dots.
ok	Click this after choosing the right StepNr.
Nr of Steps	Choose, how many intermediate steps per direction (+x, -x, +y, -y) should be measured. Confirm with enter-key.
Size of Steps	Shows the resulting size per intermediate step (= StepNr / Nr of Steps).
run	Click to accept all settings and leave this vi.

Expert Mode and additional information:

Because the patterns for each individual point are identical but rotated, the sum of all four patterns would lead to vanishing of all spots. To avoid this, the patterns get a small offset in position, without changing the deflection. Nevertheless such symmetrical patterns are not very efficient and in some occasions the pattern can still result in vanishing patterns.

2.1.6 Find center (noCenter v2.vi)



2.1.6.a: noCenter v2.vi, image with 4 dots

If the “no center” option is chosen this VI starts while the “calibration v2.vi” is running (twice, once in between the first measured line and the calibration itself) and later on in the “multipleDotsNew v3.vi”.

In general it is useful to block the center beam to reduce light pollution, but since its position is important to know for the calibration, it is obtained by creating 4 dots like in chapter 2.1.5, and finding the intersection of the line between the dots at +x and -x and the line between the dots at +y and -y.

Chose the “StepNr” to see 4 dots, as far to the sides at possible, and click on “run”.

Expert Mode and additional information:

Because patterns in a single direction induce deflections in a single direction, with this VI the center-position can be determined even while the beam path for the center spot is blocked. First the size of deflection can be chosen like in “trySizes” (see 2.1.5). Afterwards only the single direction deflection patterns are used and the single deflections measured.

With

$$\text{Dot}_{+x} = (x_{a1}; y_{a1}), \quad \text{Dot}_{-x} = (x_{a2}; y_{a2}), \quad \text{Dot}_{+y} = (x_{b1}; y_{b1}) \quad \text{and} \quad \text{Dot}_{-y} = (x_{b2}; y_{b2})$$

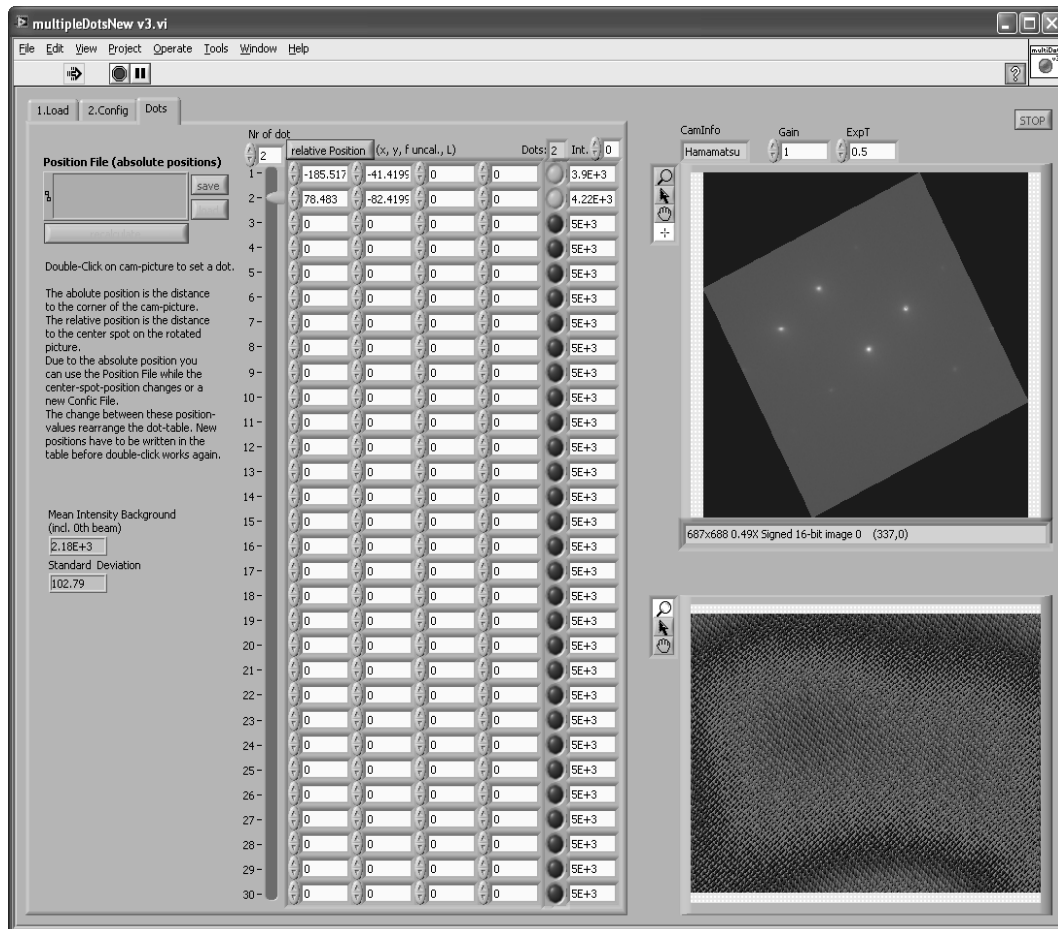
the center-position is given as (x; y):

$$y = x_{a1} - Q \cdot (x_{a2} - x_{a1}) \quad \text{and} \quad x = y_{a1} - Q \cdot (y_{a2} - y_{a1})$$

$$\text{with } Q = \frac{\frac{(x_{a1} - x_{b1})}{(x_{b2} - x_{b1})} - \frac{(y_{a1} - y_{b1})}{(y_{b2} - y_{b1})}}{\frac{(x_{a2} - x_{a1})}{(x_{b2} - x_{b1})} - \frac{(y_{a2} - y_{a1})}{(y_{b2} - y_{b1})}}$$

7.5. Appendix

2.1.7 Light distribution settings (multipleDotsNew v3.vi)



2.1.7.a: *multipleDotsNew v3.vi*, running, with two dots positioned and additional ghost-dots.

Without switching to “expert mode”, the most of the settings should not be changed in this VI. As a standard user wait until the third tab named “Dots” is shown. Do not touch the other tabs (“1.Load” and “2.Config”).

All controls to adjust the desired light distribution are on the left side. Positioned on the right side are the camera image with options and the pattern sent to the SML.

The main control of this VI is the big table in the middle.

Atop of the table, from left to right:

Nr of dot	Which dot is to be changed while using the camera-image to position dots (see below).
Button "relative Position"/ "absolute Position"	Changes the coordinate system. The relative position is given on a coordinate system rotated with the inner-image and with the center (zero deflection) as point of origin. The absolute position use a coordinate system with the sides of the whole image as axes and one edge as point of origin.
Dots	Number of active dots.
Int.	Range of area of integration of the intensity of the dots.

The Table (left to right):

Position in x.	
Position in y.	
Focal length	Of an additional lens-pattern for a single dot.
L	A mathematical construct specifying a pattern to create a donut.
Line?	Set to 1 or 2 and $f > 0$ (e.g. 2) to create a line in x or y.
Green buttons	To activate and deactivate single dots.
Intensity value	On the dot position (or center position of a line/ donut).

On the left side, it is possible to save and load positions to/ from a simple text file (see Appendix). Click “recalculate” after loading a file.

Below this panel, the mean intensity of the background and the standard deviation are given.

The images on the right part are comparable with those VIs used before. In addition to the standard camera controls is a small cross-hairs symbol. Selecting this and then double-clicking somewhere in the image reads the x-y position and adds it to the appropriate fields of the with “Nr of dot” selected dot.

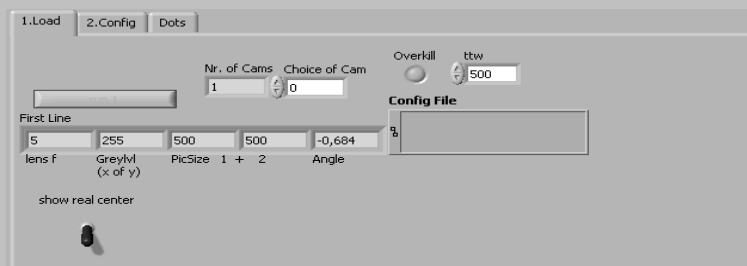
The “Gain” and “ExpT” are saved depending on the number of active dots.

Expert Mode and additional information:

This VI can run without using “Master.vi”. Started separately, a pop-up will ask for a calibration file created by “Calibration v2.vi”(see 2.1.4).

Depending on previously selected options, some settings are already chosen depending on the configuration files.

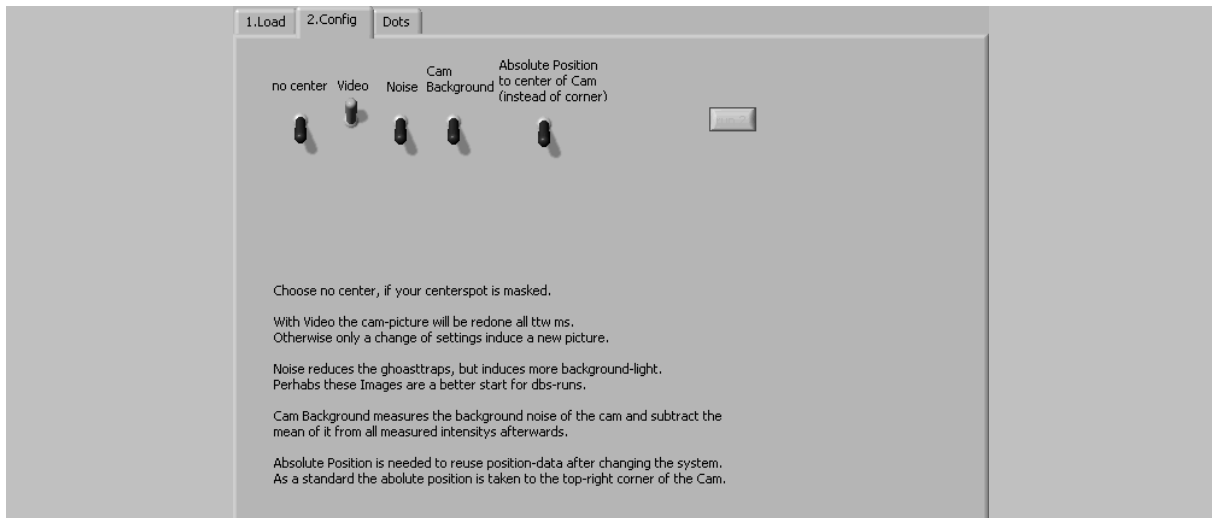
Different to the standard protocol, the VI starts with the tab “1.Load”.



2.1.7.b: *multipleDotsNew v3.vi, tab "1.Load"*.

Before clicking on “run”, the settings given by the configuration file can be controlled (“First Line”). Also the camera can be selected and the position of the dot tested. “ttw” sets a time in seconds to wait between single camera images.

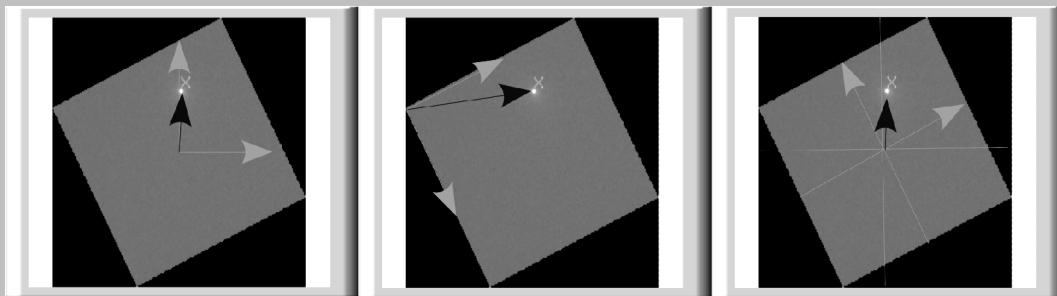
7.5. Appendix



2.1.7.c: *multipleDotsNew v3.vi*, tab "2.Config".

no center	Switch on to use "noCenter v2.vi" (see 2.1.6) to determine the center-position.
Video	Switch on to update the camera image every "ttw" seconds. Otherwise it is only updated when the SLM settings are modified.
Noise	This switch produce some random noise, which increase the scattered light but decreases the intensity of ghost dots.
Cam Background	Switch on to measure the background noise of the camera and subtract the mean from intensity values given on the third slide. Opens the "camBackground.vi" (see 2.1.8).

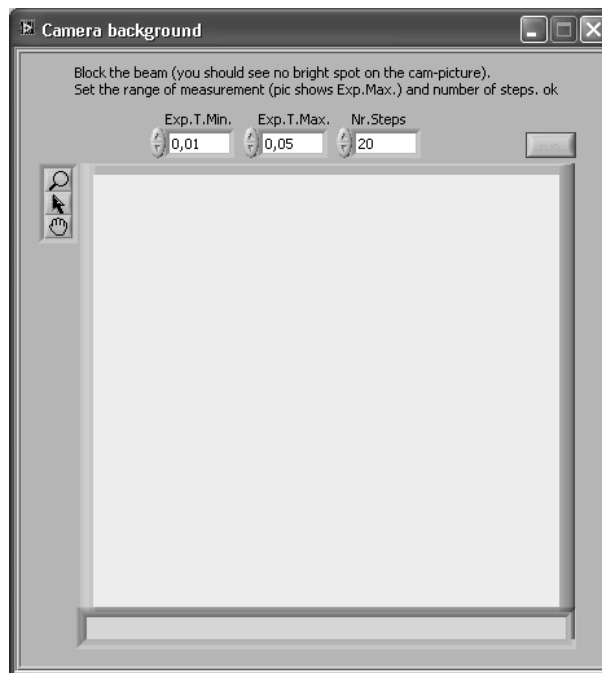
Absolute Position to center of Cam (instead of corner):



2.1.7.d: *relative and absolute position*. Left: *relative position to dot without deflection pattern*. Center: *absolute position to corner of camera-image*. Right: *absolute position to center of image*.

While the relative position is the position needed by the software to calculate the pattern, the absolute position enables to save positions independent of the position of not deflected light, but dependent of the rotation between ALM and camera.

2.1.8 camBackground.vi



2.1.8.a: *camBackground.vi*.

If “Cam Background” in “multipleDotsNew v3.vi” is activated, this VI measures the background of the camera while using different exposure times. The results are subtracted from the intensities shown on “multipleDotsNew v3.vi” slide “Dots”.

First, block the beam! This measurement should measure the background without the laser involved. Then, choose “Exp.T.Min.” (minimal used exposure time), “Exp.T.Max.” (maximal used exposure time) and “Nr.Steps” (how many measurements should be done). Click “run”. On the image, the resulting images are shown.

3. “Self calibrating fiber coupling software”

This system enables the user to use a spatial light modulator (SLM, e.g. an LCoS) to deposit light to fit an array of fibers. The alignment could be done indirectly, e.g. aligning the light emission of an illuminated sample. In order to achieve this, it calibrates the patterns sent to the SLM depending on the resulting photon counts of photon detectors behind the fibers.

The Master2.vi is a top level VI, which guides the user through several sub-VIs. Doing so, it handles the communication with the hardware. Most changes can be done while running the Master2.vi. However for some unusual parameters and for permanent changes some sub-VIs have to be opened separately. Unusual parameters will be shown by expanding the front windows (double click on windowbar) and can only be effectively changed before running the software. Also, this software widely uses drivers of a specific counting card, the DPC-230 of the Becker & Hickl GmbH.

3.0. Speed-run

Shortest version of the manual for using this software.

- (1) Turn on laser, APDs (counter), SLM and microscope. Set laser power to minimum and beam path to ocular/ eyes. Use fluorescent plate.
- (2) Start "Master2.vi" by using the small arrow in the top bar. The "OD Filter Wheel" starts.
- (3) On the first pop-up click "Yes" if the "Camera Window" is desired. Set wavelength of laser.
- (4) Select "new calibration" if a new calibration is required. Otherwise a calibration-file will be requested. Select "measurement" if the measurement software should be started.
- (5) Push the red button.
- (6) If a "new calibration" is required:
 - (a) Enter the wavelength of illumination light.
 - (b) Use tutorial? It helps a bit, but for regular users it is not necessary.
 - (c) A bigger panel opens, the "Fiber Finder Mainwindow". Use default settings, click on "start". "Save all" enables saving of whole measurements and shows the fitting. "f corr" is trying to correct the focus (z axis) of the illumination path (still in the testing phase).
 - (d) Follow the instructions on screen and wait.
 - (e) If "Save all" was activated, save all-calibration-file and "All Data Window" will open. Toggle between fiber numbers to review the fits. Click "STOP" to continue.
 - (f) Save calibration-file.
- (7) "Chose Fibers to illuminate" opens.
 - (a) If no new calibration is done, choose a calibration file.
 - (b) Chose fibers to illuminate, click "do it" to proceed.
 - (c) If "Camera Window" open, save current light distribution (see 1.2).
- (8) If "measurement" was selected, the "Measurements" window opens in parallel.
 - (a) Choose a name for the measurement (date will be added automatically).
 - (b) Select fibers to measure and choose settings for the measurement. Default works fine! Deactivate data export to save some time. Hint: Make a 10 sec measurement with data export and, if it is good, a 10×10 sec measurement without export afterward.

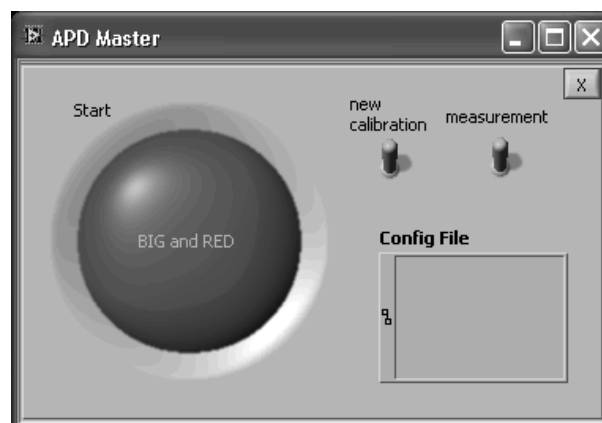
- (c) Change filter wheel position on “OD Filter Wheel” window.
- (d) Click on “run”. A new window opens. Counts up to 10^6 per TDC are ok. Wait until “run” on “Measurements” window is red again. If “data export” was chosen, the workload for the PC even after the measurement is large and requires some time. Use Windows Explorer to look at the results.

Tip: Confocal volume calibration measurements to determine the size are necessary for each illumination setting. It should be done after the cell measurements, because the needed pattern are known afterward.

3.1. Standard-protocol

Turn on laser, APDs (counter), SLM and microscope. Set laser power to minimum and beam path to ocular/ eyes. Use fluorescent plate or a fluorescent fluid. In case of the later one, the laser intensity has to be adapted.

3.1.1 APD Master (master_2.vi)



3.1.1.a: APD Master, running.

Open the APD Master (Master2.vi) and start it by using the small arrow in the top bar. A second window will open, the OD Filter wheel (see 1.1). A pop up will ask to open a camera window (see 1.2). Both windows can be used in parallel and should not be closed. Do not select “reread Position” on OD Filter Wheel window.

Deactivate the “new calibration” switch if you want to use an existing calibration. A calibration takes less than 5 minutes, so repeat a calibration each day before measuring.

Deactivate the “measurement” switch if you do not want to use the implemented measuring software but the proprietary software SPCM from Becker & Hickl GmbH.

The red button runs the system.

The “X” stops all running LabVIEW Software. Due to the communication drivers of the counting card, an abrupt ending of the software, in most cases, has to be followed by a restart of the computer.

3.1.2 Fiber Finder Mainwindow (mastercounter_v3.vi)

If a “new calibration” was chosen, a pop up will ask for the wavelength of the used illumination light and the Fiber Finder Mainwindow will be opened. A pop up asks, if you want to use a tutorial.

In this VI, a line shaped illumination scans the substrate, e.g. the fluorescent plate, and the excitation scans the fiber array. Counting the photons transmitted by the fiber, the position of the fibers relative to the beam path axis can be found.



3.1.2a: Fiber Finder Mainwindow, running.

The tutorial can be switched on and off with the “?” button and the Vi stopped during acquisition with the “X” button.

For most cases the default configuration is suitable.

Max Deflection	This is the maximal deflection of the light from center position. If it is too small, not all fibers are covered and can be found. Additionally, a too small threshold can influence the positioning (the fitting) negatively.
Nr of steps	This is the number of measured steps between center position and maximal deflection in one direction. Could be set as low as 50 to improve speed at the cost of the accuracy. The total number of measurements is equal to (Nr of steps) x 4 + 2
Wavelength	This is, in case of running this Vi by using the APD Master, already set.
Init Card	Only needed in case of running the software without the APD Master.
Save all	Enables saving of whole measurements additionally to the fiber positions found. Also enables an “All Data Window” showing the measurement data and the fit.
F corr	Beta ware, starting a software to align the z position of the illumination.
CollTime [s]	Collection time per measurement. Can be reduced by increasing the illumination light.
f total	Creates an additional lens in the illumination path for all measurements (it is saved in calibration file).

Click “start” to run the calibration.

Follow the instructions on the screen:

Switch excitation path to ocular/ eyes and focus the illumination. Switch excitation to camera port and the camera port adapter to the fiber array. Follow the instructions on the screen, because the software will control the filter wheel/ illumination intensity accordingly.

Acq: shows how much of the acquisition is finished.

Calc: shows how much of the measurements were handled.

Troubleshooting:

If the Acq is much too fast, the communication to the counting card is lost (restart the computer).

If the Calc is much slower (less than half in speed) the counts are probably too high. Stop calibration, reduce the illumination and restart.

If “Save all” was selected, you can save the whole measurements after the calculation ended and the “All Data Window” will open.

Afterwards a pop up asks to save the calibration file.

Additional settings and information:

Double click on the top bar shows some additional settings and information.

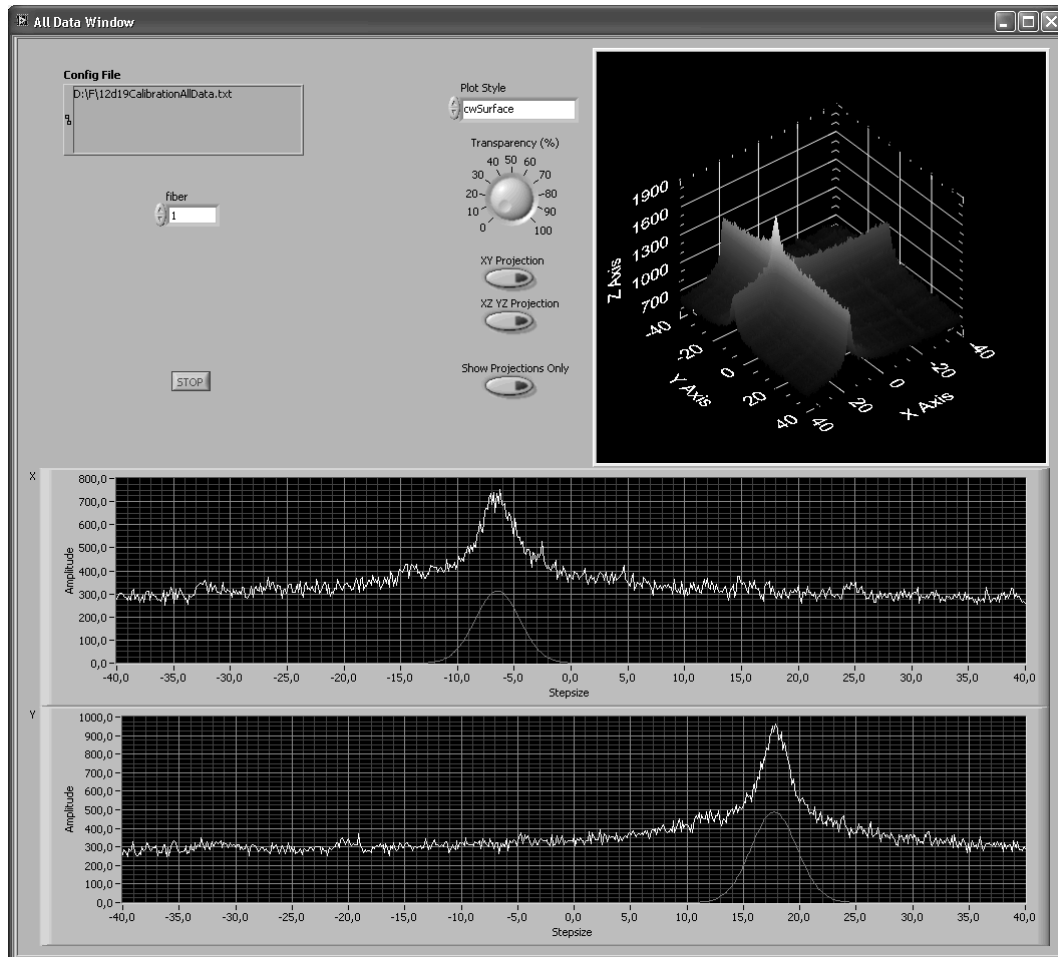
A bar below the main part shows the counts per channel and measurement.

On the left is a second setting panel. Changes on this panel only have an effect before starting. “Sizes picture” sets the number of pixels of the SLM. All other settings of the SLM are dependent of the wavelength and will be adjusted automatically by the software. “Max Counts per Second” and Channel sets a threshold to stop illumination automatically if needed. But since the calculations might be far behind the measurements, especially in case of high counts, this could be too slow. “LCoS Correction” is a switch to disable the use of the background correction of the LCoS (the correction will be chosen accordingly to the wavelength). “Size of steps” is equal to $(\text{MaxDeflection})/(\text{Nr of steps})$ and represents the resolution of the calibration.

7.5. Appendix

3.1.3 All Data Window (countergraph.vi)

If in Fiber Main Window “Save all” was selected, the “All Data Window” will open after the measurement.



3.1.3.a: All Data Window, showing measurement of fiber number 1 with fits after fitted background correction.

Change the shown fiber using the “fiber” setting. LabVIEW counts from 0, so for 16 fibers, you will find fibers 0 to 15.

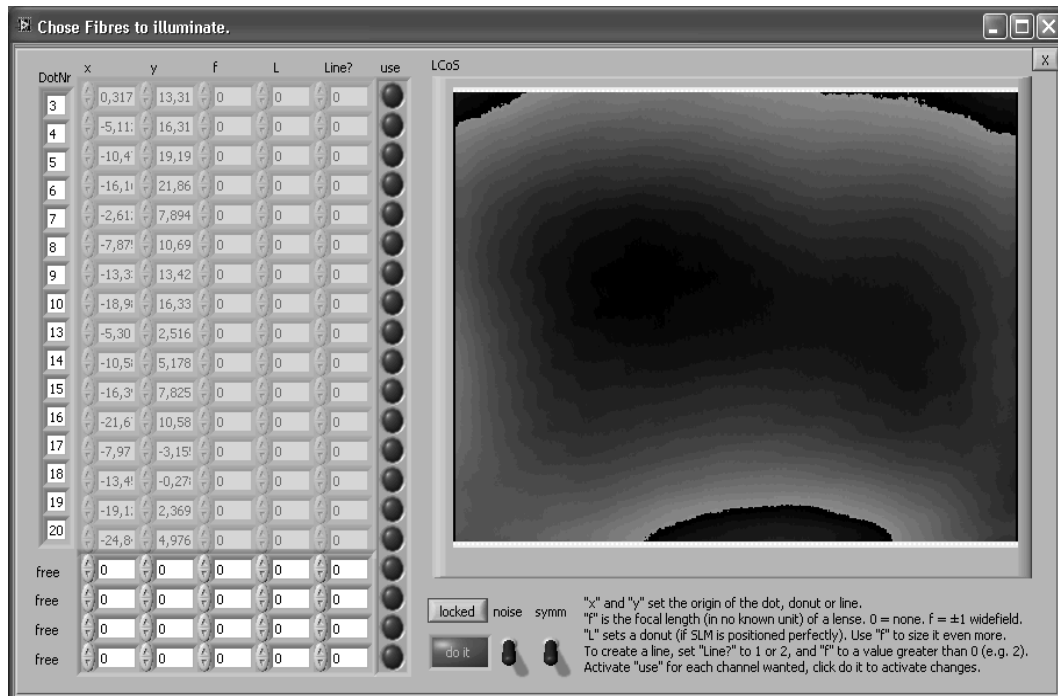
The two graph in the bottom half of the panel show the measurements per fiber: deflection (x axis) against Amplitude/ counts (y axis) and the corresponding Gaussian fits (red line), before which a broad Gaussian is fitted and subtracted to correct for diffusive light distribution around the illumination line.

On the upper right is a 3D representation and settings to change it. Some “Plot Styles” need a lot of time to proceed! The diagram represents the counts detected through a single fiber, dependent of the deflection of the illuminated line. In the crossing of those two lines with the maximal counts, the fiber is found. It does not show the real counts on the whole surface, for only on the single fiber position (where the maximum is found) any photons were counted.

Click “STOP” to close this window and to continue.

3.1.4 Choose Fibers to illuminate (founddotscreator_v2.vi)

If no new calibration was made, you will be asked for a calibration file here.



3.1.4.a: Choose Fibers to illuminate, no fiber selected.

Controls are on the left, an image of the used LCoS pattern is on the right.

The upper 16 lines of the table represent the found 16 fiber positions. The “DotNr” represents the numbers used inside the counter card drivers and the SPCM software from Becker & Hickl GmbH.

It is always good to take a look with the fluorescence slide, if they are positioned symmetrically.

To activate fiber illuminations, click on the green “use” buttons of your choice and click on “do it”.

The lower 4 lines enable additional, free positioned illumination positions. - Dots, lines and donuts.

Below the image, you can unlock the calibration data of the fibers with the “locked” button. This will not change the actual calibration file! Additionally, using this button will put the LCoS pattern back.

“Noise” is a small change in pattern, not changing the positions of the illumination, but reducing the ghost trap illuminations.

“Symm” adds a small shift in each pattern for a single fiber illumination apart from the first. Using this, even totally symmetrically patterns $(x; y) = -(x; y)$ are possible. However lenses and donut pattern will be shifted slightly.

7.5. Appendix

Additional settings and information:

Double click on the top bar shows some additional settings and information.

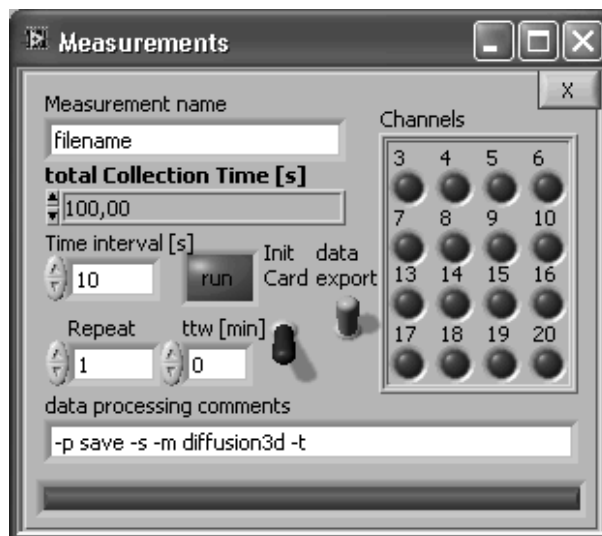
Below the original panel is a second setting panel. Changes only take effect before start.

“Wavelength input” allows using a calibration done for one wavelength for another wavelength. In theory, a calibration using a range of 2π with one wavelength is compatible with another wavelength, using its own settings to create a range of 2π . Of course, this only corrects for the influence and settings of the LCoS. To correct for aberrations of the remaining software, an independent calibration is needed. “-1” is default, using the wavelength set inside the calibration file.

In “center position patterns” the center position of LCoS patterns can be changed. This is generally only required if you want to create perfect donuts but the illumination is not hitting the center of the LCoS. “Center position lens over all” enables the same setting for a lens pattern created on top of all patterns (value of lens given by calibration file). In both cases, the default “-1” positions the center into the center of the LCoS.

3.1.5 Measurements (Counter_Reader.vi)

If in Fiber Main Window “measurement” was selected, the “All Data Window” will open parallel to 3.1.4.



3.1.5.a: Measurements.

This Vi can be used to start a photon counting measurement and save the photon arrival times for all channels. It creates binary *.spc files(Becker & Hickl GmbH), saving the relative times between each single photon and the number of the detecting APD.

All data were saved in a internally given directory named *year.month.day_hour.minutes.seconds_filename_rX* with X the number of the repeat, starting with 0.

Measurement name	Give the measurement a name. Additionally date and time will be added.
Total Collection Time [s]	Total measurement time in seconds.
Time interval [s]	The total measurement is spit into intervals of this time length. Intervals above 25-50 seconds will in most cases result in a memory overflow of the counting card. Since all intervals are part of a single measurement (without break), they can be combined afterwards. (Due to LabVIEW internals, the interval time is not met perfectly, but the total time is kept.)
Repeat	Automatically repeats the measurement for a number of cycles. The laser will be stopped in between and the filter wheel position is saved.
Ttw [min]	Time to wait between cycles of measurements.
Init Card	Initiate counting card, only needed if this VI is started separately.
Data export	Exports the binary *.spc files into usable FCS data. Needs a lot of computational power and time and can also be done afterwards (via an external "FCS analysis package" written in Python).
Channels	Select APD channels of measurement.
Data processing commands	Options for the "FCS analysis package", script fcs-progress.

The red bar shows procedurally how many cycles of measurements are done.

The red "run" button starts the measurements. A new measurement can be started as soon as the button turns red again. However in case of data export, the computer might be busy for a longer period of time.

A second measurement window named "Measurements Running" will start and show the progress of each measurement cycle.

The "X" stops between measurement cycles. An immediate stop is not possible inside this Vi (but e.g. using the APD Masters "X") and would surely result in a communication loss to the counting card.

Additional settings and information:

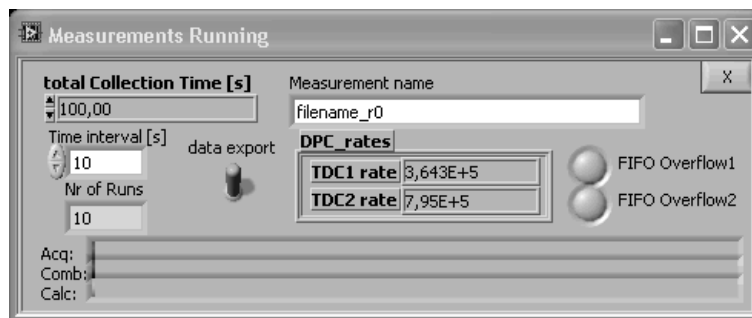
Troubleshooting: in case of problems, almost always the communication to the counting card is lost. In some cases, restarting the software and re-initializing the card helps, but in most cases a reboot is needed. A high overflow of the counting card memory often result in a communication loss. The same problem occurs using the software from Becker & Hickl GmbH.

It is a good routine to measure a "total Collection time" of 10 sec with "data export", looking at the FCS curves inside the folder of the measurement. If the curves are nice, repeat the measurement with e.g. 10×10 sec without data export. If you want to be save, do another 10 sec measurement with export afterwards and compare the short time measurements. Extracting a measurement of 10×10 sec can take half an hour! It is possible and stable to start a new measurement before the data export is finished, although the number of parallel data exports should be kept low.

7.5. Appendix

It is suggested to measure a confocal volume calibration to determine the size of the volumes after the measurements, because the needed illumination settings are known afterwards and should to be done for each setting separately.

3.1.6 Measurements Running (DPC_measurement_my_v2.vi)



3.1.6.a: Measurements Running.

This window opens while a measurement is running.

No data can be changed while running. But the data export can be switched off.

“DPC_rates” are the photon count rates for the first 8 APDs and the second 8 APDs separated into “TDC1” rate and “TDC2 rate”. Since overflows can result in a loss of communication to the counting card and the need of a reboot of the computer, you should observe the counts!

- Each single rate should not be much higher than 1.0×10^6 .
- Both single rates together should be smaller than 2×10^6 .

FIFO Overflow will turn red if one of the memory bars of the counting card overflows. The single measurement interval will be stopped, so there are no 'breaks' inside the measurement data and they can still be used! But such a measurement interval can not be combined with later intervals of the same measurement.

Three bars below show the progress of the measurement (“Acq”), the combining of the data of both memory bars to empty the internal computer memory (“Comb”), and starting the data export – if activated (“Calc”).

The “X” will stop a measurement after the step which is running at that time. With some luck, this should not result in loosing the communication to the counting card.

Each interval is saved separately in the folder representing the repeat, named: *filename_rX_iY.spc* with X the number of the repeat and Y the number of the interval, each starting with 0.

Appendix

Folder structure

```

Application folder
  → configfiles
    |   → Corr_Patterns
    |   |   → original
    |   |   → improved
    |   |   → improved_sized
    |   |   → improved_lvl
    |   |   → improved_sized_lvl
    |   |   → 488nm.png; 500nm.png; 510nm.png; ...
    |   |   → *488nm.png; *500nm.png; ...
    |   → CountingCard
    |   |   → dpc230.ini
    |   |   → spcm32.dll
    |   → Filterwheel
    |   |   → FW102x.dll
    |   → NumberOfGreylvl.txt
  → manuals_and_software
    |   → BH_CountingCard
    |   → Hamamatsu_Camera
    |   → Hamamatsu_LCoS
    |   → not_needed
    |   → Python
    |   → VirtualSecondDesktop
  → temp

```

Application folder: All scripts, independent of language.

configfiles: All configuration files, including corrections for the SLM

NumberOfGreylvl.txt: Table with 2 columns: wavelength and Nr. of grey-level. Separated by tab.

Corr_Patterns: Correction-images for the SLM.

Name convention: *nm.png, while * is the related wavelength.

Same as in improved_sized.

Pattern images for the SLM (improved_sized_lvl for direct use).

Name convention: *nm.png, while * is the pattern name and related wavelength.

original: Correction-images delivered by company

improved: Use "addCorr.vi" to add single colored images till jerky leaps are out of center.

improved_sized: sized to screen resolution. Used by software.

7.5. Appendix

improved_lvl: squeeze color spectra depending on wavelength (see NumberOfGreylvl.txt).

improved_sized_lvl: see improved_lvl and improved_sized. For use outside this software.

CountingCard: Files for the counting card.

dpc230.ini: Configuration of the counting card. Can be edit with text editor.

Spcm32.dll: Library of scripts to use the card, delivered by manufacturer.

Filterwheel: Driver for the filterwheel, delivered by manufacturer.

FW102x.dll: Library of scripts to use the filterwheel, delivered by manufacturer.

manuals_and_software: Additionally needed or useful software and manuals delivered by companies.

BH_CountingCard: Software and manuals from Becker & Hickl to use the counting card.

Install "tcspec_setup_32 2011.exe" to use their measurement software.

Keys.html contains license keys.

Hamamatsu_Camera: Drivers needed to run a Hamamatsu camera with LabVIEW.

Hamamatsu_LCoS: Software from Hamamatsu. Not needed.

not_needed: Additional software for installed hardware, but not needed.

Python: Python 2.7.2, needed for scripts addressing counting card measurements.

epd-7.0-2-win-x86, incl. Python 2.7, for additional packages.

VirtualSecondDesktop: for the second monitor-out is connected to the SLM, sometimes windows can be opened on the SLM instead on the monitor. Connect VNC to "localhost" to see the content send to both monitor-out.

temp: All temporary files. Not self-emptying, but overwriting themselves.

Calibration-file of Master.vi

Editable with text editor. Contains configuration and calibration of the SLM.

Created by "Calibration v2.vi".

Called by "multipleDotsNew v3.vi".

Table with 5 columns, separated by tab.

First row:

- Setting of focal length of a lens-pattern on the SLM. 0 = no lens.
- Number of used grey-level A in a spectrum of grey-level B, written as AB.
- Resolution in x.
- Resolution in y.
- Angle: while calibrating, the camera-image is rotated to achieve deflections in single directions (x or y). Corrects rotations of the beam path between SLM and camera.

Second row:

- Number of measurements in direction of +x.
- Number of measurements in direction of -x.
- Number of measurements in direction of +y.
- Number of measurements in direction of -y.
- 0, 1 or a number: 0/1 if correction-image or number for correction for specified wavelength.

Following rows:

- Direction specifier: 0, 1, 2, 4 for +x, -x, +y, -y.
- Steps used for measurement in x.
- Steps used for measurement in y.
- Deflection of dot in x.
- Deflection of dot in y.

Position-file of "multipleDotsNew v3.vi":

Absolute positions of dots and the used exposure times and gains.

Created by "multipleDotsNew v3.vi".

Called by "multipleDotsNew v3.vi".

Table with 31 columns, separated by tabs, and 32 rows.

First row: Gain, used for 0 to 30 dots.

Second row: Exposure time, used for 0 to 30 dots.

7.5. Appendix

Following rows: Describing dots.

- Dot activated (1) or not (0).
- Steps in x.
- Steps in y.
- Used focal length.
- Used L.
- Used Line?-comment
- Zeros, filling the rows to column-number.

Calibration-file of MasterCounter_v3.vi

Editable with text editor. Contains configuration and calibration of the SLM to match detectors.

Created by "MasterCounter_v3.vi".

Called by "foundDotsCreator.vi".

Table with 5 columns, separated by tab.

First row:

- Setting of focal length of a lens-pattern on the SLM. 0 = no lens.
- Number of used grey-level A in a spectrum of grey-level B, written as AB.
- Resolution in x.
- Resolution in y.
- 0, 1 or a number: 0/1 if correction-image or number for correction for specified wavelength.

Following rows: Describing dots.

- Steps in x needed for detector.
- Steps in y needed for detector.
- Used focal length (always 0).
- Used L (always 0).
- Used line comment (always 0).

All data:

If all data are saved, the file containing those data looks different.

Created by "MasterCounter_v3.vi".

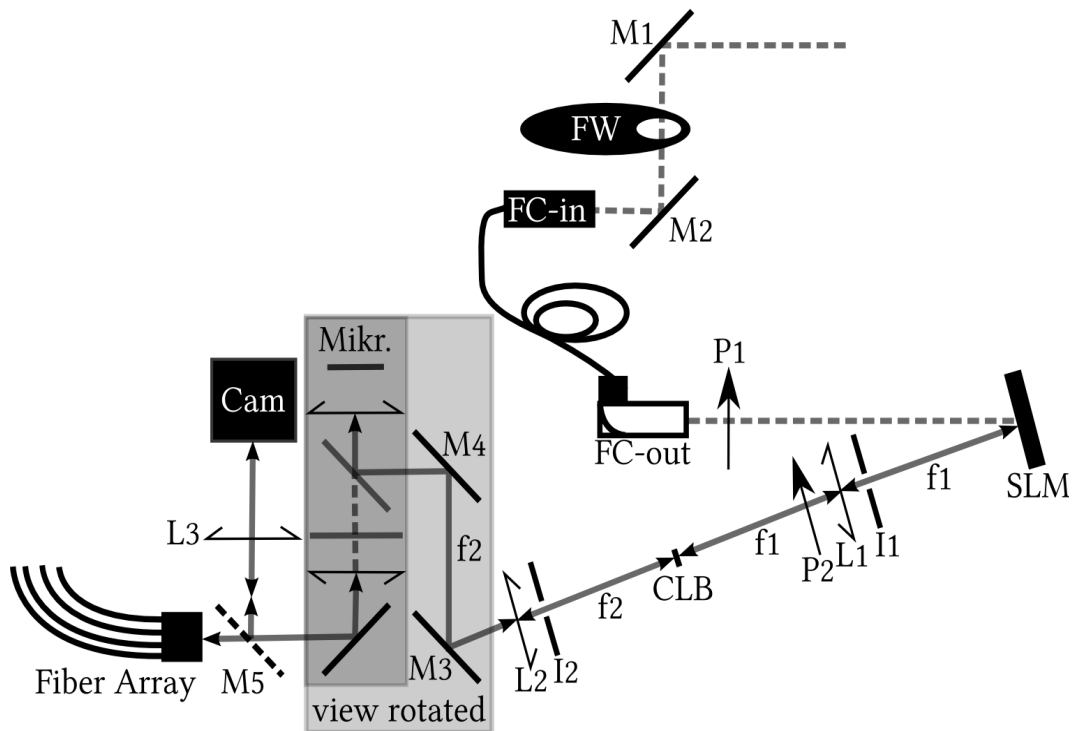
Called by "counterGraph.vi".

Table with 25 columns, separated by tab.

Describing counts for all channels depending of pattern.

- Steps in x needed for detector.
- Steps in y needed for detector.
- Used focal length (always 2; f needed for lines).
- Used L (always 0).
- Used line comment (1 while steps in x, 2 while steps in y).
- Counts on CFDs 1 and 2 (always 0).
- Counts on APDs 1-8 (channels 3-10).
- Counts on CFDs 3 and 4 always 0).
- Counts on APDs 9-16 (channels 13-20).

Manual alignment steps



- M1 = mirror 1*
- M2 = mirror 2*
- FW = filter wheel*
- FC-in = fiber coupler input*
- FC-out = fiber coupler output*
- P1 = polarizer 1*
- SLM = spatial light modulator*
- I1 = iris 1*
- L1 = lens 2*
- P2 = polarizer 2*
- CLB = center light blocker*
- I2 = iris 2*
- L2 = lens 2*
- M3 = mirror 3*
- M4 = mirror 4*

In general:

All lenses and the polarizer should be hit by the beam in the center and the reflected part should overlap with the incoming beam (could be tested with a small piece of paper).

Weak light efficiency of the setup:

If the light after FC-out is much weaker than before, move the fiber a bit (if it changes dramatically, the fiber is damaged) or align the light with M1 and M2.

P1 and P2 have to be rotated while looking at a deflected dot on "Cam.vi". While the deflected light should be maximized, any not deflected light should be minimized. Remove CLB if needed.

Center the not deflected light spot:

The easiest way to center the not deflected light spot on the camera image is to move the camera. But to improve the shape (and volume) of the illuminated spots, the light focusing to the sample has to be centered to the objective back focal plane.

To test the alignment of the microscope, remove the CLB and use the correction image for the SLM. First close I2 and make sure the beam hits the iris in center. Do the same with I1. If the beam does not hit both iris in the center, align the light with the FC-out and SLM.

If a lens is probably misaligned (perpendicular to the beam path), remove the lens, align to the iris without lens and put the lens back. Align the light by moving the lens at right angle to the beam path. This can be done properly for L1, but not as accurately for L2. For a well aligned lens, moving it along the beam path should only change the focus position but not the direction of the beam path.

After this alignment, use M3 and M4 to center the beam inside the microscope. A small paper above the objective revolver (empty position or on top of an objective) can help. The alignment rod has to be put onto the objective revolver and the beam must be centered through both pinholes inside the rod.

Compare centered spot with a fluorescent plate in eyepiece and camera. The camera can be positioned perpendicular to the beam path, but should not be positioned too far from the positions of the fibers. See "camera position".

Focus the light:

To optimize the focus, the beam has to be collimated on the back focal plane of the objective. To test the alignment of the microscope, remove the CLB and use a correction image for the SLM. Move the objective revolver to an empty slot and look with a small piece of paper along the beam path above the microscope.

To align the laser light, first use the backside lamp and focus with your objective of interest, using the camera ("Cam.vi") and the microscope focus knobs.

Remove L1. Move L2 along the beam path until its focus is at the upper border of an empty objective revolver slot.

Put back L1 and use objective of interest. Focus using the camera by moving L1 along the beam path.

As an additional step, the SLM can be positioned. Very likely you would have to proceed with "Center the not deflected light spot" afterwards. Use the transmission light, with objective and a grating. Closing the two iris of the top-light separately and looking at the focus of the grating and the iris, the whole system can be checked and even the SLM positioned.

7.5. Appendix

Alignment of CLB:

Chose a small blocker first, move to bigger if needed. But a big block will produce a "dead area" around the position of the not deflected light, where no light could be set to. Use the camera ("Cam.vi") and a correction image for the SLM. Position the light-blocker in focus between L1 and L2. Align it with the knobs on the CLB until most light is blocked.

Hitting the SLM in center, or "who bit off my donut":

Although normally not very important, it is needed to create donuts. Donuts are created by a phase shift in a circular pattern with a center of pattern. If the light is not aligned correct, the donut will be open to one side. Move the SLM and the FC-out until the donut is closed. Very likely you have to proceed with "Center the not deflected light spot" afterwards.

In some parts of the software, it is possible to change the position of the center of the pattern.

Total loss of beam path:

It is not easy to position the SLM and the FC-out if the beam path is lost completely. Remove L1 and L2 and CLB. Use an alignment laser close to the former position of L2, put it through I2 and I1, try to hit the SLM in the center and position the FC-out accordingly. The angle between incoming and reflected light by the SLM should be very small.

Camera position:

In most cases, it is enough to center the not deflected light spot by moving the camera perpendicular to the beam path. But to be able to see the positions of the spots created to fit the fibers, and to center the not deflected light spot can require multiple steps between aligning the camera and the "Center the not deflected light spot". To find the fibers, mount a 50:50 beamsplitter inside the dual-port C-mount adaptor on the left side of the microscope, use no filter inside the microscope and a fluorescent plate. Connect an alignment laser to the fibers and focus the microscope while the light is sent to the camera port. In most cases, it is enough to look at three fibers: two along a line (for testing the rotation of the fiber array – can be changed by rotating the fiber array) and one across. The other fibers are in between.

In addition there is a lens in the beam path between the dual-port C-mount adaptor and the camera. The position can be changed by rotating the tube. An image on the camera should be in focus at the same time as on the eyepiece. This can be tested with a test-grid or any other sharp object on the microscope, and the toplight.

FCS analysis package

Needed: Enthought Python Distribution with Python 2.7 and additional packages (use “epd-7.0-2-win-x86.msi” in software folder) and the Python FCS analysis package written by Dr. Hernán Grecco.

Commands:

fcs-process (-f -p -s -m -t)

-f, --format, default = auto
 -p, --plot, choices=('none', 'show', 'save', 'both'), default = show
 -s, --save, default = False
 -m, --model, model to be fitted to the autocorrelation curve.
 -t, --table, default = False, save processed data as a table.

fcs-stats

fcs-join

fcs-collect (-r -o)

-r, --recursive, running through folders below the path given here.
 -o, --output, path and name of file for the results.

fcs-refit (-p -m -s --fr --to -r)

-p, --plot, choices=('none', 'show', 'save', 'both'), default = show
 -m, --model, model to be fitted to the autocorrelation curve.
 -s, --save, default = False
 --fr, fit from in seconds (e.g. 0.000001)
 --to, fit to in seconds (e.g. 0.5)
 -r, --recursive, running through folders below the path given here.

Example commands:

Calculating FCS of all *.spc in the sub folders of a specific folder including picture, fit:

```
C:\Python27\python "C:\Python27\Scripts\fcs-process" "F:\measurements\*\*" -p save -s -m
diffusion3d -t
```

Counting total counts per channel, result saved in a file:

```
C:\Python27\python "C:\Python27\Scripts\fcs-stats" "F:\measurements\*\*" >
"F:\measurements\allCounts.txt"
```

Joining the parted *.spc-files (only use on files of the same measurement without gap):

```
C:\Python27\python "C:\Python27\Scripts\fcs-join" "F:\measurements\*.spc"
```

And calculating FCS of this curve:

```
C:\Python27\python "C:\Python27\Scripts\fcs-process" "F:\measurements\*.rawpy" -p save -s -m
diffusion3d -t
```

7.5. Appendix

Listing all *fit.txt-data resulting of the fcs-progress found in one folder and its sub folders into one table:

```
C:\Python27\python "C:\Python27\Scripts\fcs-collect" -r "F:\measurements\" -o "F:\measurements\collectedData.csv"
```

Recalculating the fit:

```
C:\Python27\python "C:\Python27\Scripts\fcs-refit" -p save -m diffusion3d -s --fr 0.000001 --to 0.5 -r "F:\measurements\"
```

Other important commands:

To switch to a different folder: `cd\Folderpath\`

To list all files inside a folder and print the list to a textfile: `dir /b > list.txt`

To create an executable list of comments in Windows, copy them to a *.txt-File and rename the ending to *.bat .

8. Acknowledgements

I want to thank Prof. Dr. Philippe Bastiaens and Prof. Dr. Hernán Grecco for the chance to work in such an international, interdisciplinary and renowned institute. It is probably a curiosity to walk with a smile to a only half paid but laborious work, a curiosity produced by individual responsibility, liberty and backup of brilliant minds.

I want to thank Dr. Sven Archibald Hubertus Müller, one of those rare human too good for himself and whose importance for the department has to be underestimated by anyone not sitting in the same office (and playing his clerk).

Furthermore I want to thank Dina Truxius for guiding me through the mysterious deeps of biological acronyms and preparing the biological samples. I want to extend this gratitude to those in the department, who tried to explain their gain of years of study to a physicist. Interdisciplinary work is only as good as the individual cooperativeness, for any individual should listen to and do each practical step once or twice by himself, but should not try to substitute the expertise of other attendant disciplines.

Another excellence of the institute are the supporting handicraftsmen, whose helpfulness and local expertise enrich any system development. Especially I want to thank Joachim Besler and his crew (tool shop) for fast and skillful crafting of custom mechanical components, Rüdiger Fehrmann (electrician) for assembling the APD array components and other electrical components, e.g. the LCoS cooling unit, and Udo Koester (IT department) for an unforgettable assembling of the most stuffed retro desktop computer I ever needed.

Special thanks to my parents, which not only endured my curiousness, but boost it till they let me loose to the community. Without their support, my laziness could have prevailed. My gratitude expands to my friends accepting my peculiarity and my curtness during the past years. I will better myself.

Last but not least a warm hug to my furry roommate Nicky, which I had to neglect too much the last couple of months but still selflessly eased my mind.

9. Curriculum Vitae

Name: Thimo-Christian Göllnitz
Address: Lessingstraße 61, 44147 Dortmund, Germany
eMail: Thimo@Goellnitz.eu
Date of Birth: 24.08.1981
Nationality: German

Education:

Aug. 2009 - Nov. 2012: Doctoral candidate at the Max-Planck Institute for Molecular Physiology, Dortmund
Department of Systemic Cell Biology
Technical University Dortmund, faculty chemistry
Prof. Dr. Bastiaens
Group of Dr. Grecco

Mar. 2007 - Jun. 2008: Diploma thesis at the Institute of applied physics, University of Hamburg
Department of scanning probe methods
Prof. Dr. Wiesendanger
Prof. Dr. Heck, inorganic and applied chemistry, University of Hamburg
Title: Photolytische OMCVD-Abscheidung von Wolfram auf Glas -
Entwicklung, Realisation und erste Testmessungen.

Feb. 2005 - Feb. 2007: Student research assistant
Institute of applied physics, University of Hamburg
Department of scanning probe methods

Oct. 2001 - Jun. 2008: Studies in physics at the University of Hamburg
Degree: diploma degree (in German 'Diplom')

Aug. 1992 - Jun. 2001: Secondary school Gymnasium Lohbrücke, Hamburg
Degree: university-entrance diploma (in German 'Abitur')

10. Statement of Originality

The work presented in this thesis is, to the best of my knowledge, original and my own work, except as acknowledged in the text.

The material has not been submitted, either in whole or in part, for a degree at this or any other university.

Eidesstattliche Erklärung

Hiermit versichere ich an Eides statt, dass ich die vorliegende Arbeit selbständig und nur mit den angegebenen Hilfsmitteln angefertigt habe.

Dortmund,